Università degli Studi di Palermo

AREA RICERCA E TRASFERIMENTO TECNOLOGICO
SETTORE DOTTORATI E CONTRATTI PER LA RICERCA
U. O. DOTTORATI DI RICERCA

Corso di Dottorato di Ricerca in
Energy - Low-carbon Energetics and Innovative Nuclear Systems
Dipartimento di Ingegneria

Settore Scientifico Disciplinare ING-IND19

THERMAL-HYDRAULICS AND THERMOMECHANICS OF EU-DEMO DIVERTOR

LA DOTTORESSA
FRANCESCA MARIA CASTROVINCI

LA COORDINATRICE
CH.MA PROF.SSA E. RIVA SANSEVERINO

I TUTOR
CH.MO PROF. P. A.DI MAIO
CH.MO PROF. P. CHIOVARO

I CO TUTOR
ING. GIUSEPPE MAZZONE
PROF. JEONG-HA YOU

CICLO XXXVI
ANNO CONSEGUIMENTO TITOLO 2024

Contents

List of Figures

List of Tables

Abstract

Energy production from thermonuclear fusion power plants is one of the most ambitious energy projects in the world today. The European fusion roadmap outlines the main steps towards commercial fusion power plants, including the development of the European DEMOnstration Power Plant (DEMO), which will demonstrate the commercial feasibility of fusion power plants.

In this context, a crucial component is the divertor which is in charge for power handling and particle exhaust, while operating in a harsh loading environment. The current DEMO divertor is composed of a Cassette Body (CB) supporting two Plasma Facing Components (PFCs). The most promising divertor cooling scheme foresees two separate cooling circuits for the CB and PFCs, provided with cooling water at different operating conditions. Moreover, the divertor design has been recently revised so to operate the CB with a high-temperature and high-pressure coolant. These design assumptions pose new challenges in achieving uniform and effective cooling of the structure to ensure reliable operation for the intended divertor lifetime.

The work conducted during the Ph.D. years progressed along parallel paths. In a first phase, the main objective was to numerically assess the steady-state thermo-hydraulic performance of the DEMO divertor cooling circuits. In particular, an integrated fluid-structure Computational Fluid-Dynamic analyses campaign of the entire divertor was carried out introducing new details and a significant increase of complexity with respect to the previous approach adopted for such kind of studies.

The twofold aim was to evaluate the CB thermal performance under the revised coolant conditions and to compare the temperature distribution in the PFC's Target Bodies by selecting different materials actually under assessment to extend the component’s lifetime under irradiation. Despite the many advantages connected to the new high temperature divertor, some critical points were identified in terms of thermal hydraulic performances, which pose the need for a design revision of some parts.

During a second phase, attention was focused on two peculiar aspects of the thermostructural performance of the DEMO divertor. The first one was the behaviour of the CB structure subjected to the high pressure and its compliance with the structural design code. In this regard, the CB structural response under the load combination foreseen for a

hydrostatic test scenario was assessed, showing some interesting outcomes and suggesting a design revision of the internal divertor ribs to improve its structural integrity.

Furthermore, the second complementary aspect was the structural behaviour of the plasma-facing surfaces, which are subjected to high thermal and particle fluxes. In particular, the study was applied to a divertor plasma-facing surface which is supposed to be coated with a thin layer of Tungsten. In this framework, a theoretical-numerical assessment of the residual stresses on a typical Tungsten armour was carried out. The main outcome of the activity was the verification that the influence of temperature-dependent mechanical properties of the materials affects the results in a negligible way.

Introduction

Extreme instability in energy markets during the global energy crisis has underlined the importance of affordable, reliable and robust energy supply. After Russia's invasion of Ukraine, uncertainty in the Middle East could bring to further troubles to energy markets and prices. This emphasizes once again the weaknesses of the fossil fuel era, and the advantages for energy security as well as for emissions of moving to a more sustainable energy system. Moreover, according to the World Energy Outlook 2023 [1], the global economy is assumed to increase at an average of 2.6% per year to 2050 while the global population will expand from 8 billion today to 9.7 billion in 2050, driving an increase in the quantity of energy that has to be produced in order to satisfy human needs.

In this framework, research on alternative and low-carbon energy sources is required and it is a crucial issue to pursue the path to a sustainable future.

Nuclear fusion, the reaction that powers the Sun and the stars, is a potential source of safe, non-carbon emitting and virtually limitless energy, representing a concrete long-term solution for future generations, contributing to the decarbonization and diversification of energy generation. Its exploitation, aimed at achieving safe and sustainable energy production, will be essential to meet the United Nations Sustainable Development Goals [2] including access to affordable and clean energy, global climate and energy security objectives.

Energy production from fusion power plants is one of the most ambitious energy projects in the world today, due to the great technical challenges that have to be overcome to industrially exploit this energy source.

In 2014, fusion research groups from European Union member states and Switzerland signed an agreement to join a European collaboration on fusion research and EUROfusion, *the European Consortium for the Development of Fusion Energy*, was born. Its mission is to pave the way for fusion power reactors funding and supporting the research of its members on the basis of the *European Roadmap to the Realisation of Fusion Energy* as a joint programme within Euratom Horizon Europe [3].

The EUROfusion roadmap outlines the main steps towards commercial fusion power plants. The first step is the realization of the International Thermonuclear Experimental Reactor (ITER) that will demonstrate the scientific and technological feasibility of fusion as a reliable energy source. It will be operative for a period of about 20 years during which researchers will extrapolate and select data for the development of the European DEMOnstration Power Plant (EU-DEMO, simply referred to as DEMO in the following).

DEMO will meet the target of delivering a net electricity output to the grid, demonstrating the commercial feasibility of fusion power plants. The actual conceptual design phase and the definition of the final layout will bring to DEMO construction and operation, planned for the end of this century [4].

The elementary process occurring in a fusion reactor is the thermonuclear fusion reaction that involves two light hydrogen isotopes, deuterium and tritium. To make them collide with an acceptable reaction rate - required to ensure that a large number of reactions takes place per unit time and volume - they have to be heated up to 100 million Celsius degrees. In order to withstand the exceptional temperatures required, ITER and DEMO will rely on the magnetic confinement, and they will be based on the *tokamak* reactor concept. Inside these devices, the plasma, i.e. a state of matter composed of ionized fuel particles, will be confined and controlled using a complex system of superconducting coils.

The products of the fusion deuterium-tritium reaction consist of α particles and neutrons. These latter interact with the components surrounding the plasma, making possible the conversion of their kinetic energy into heat, which can be used as the main power source for a steam cycle. In this context, a crucial component, on which this dissertation is focussed on, is the divertor which is responsible for power handling and particle exhaust.

In this context, the activity conducted during the XXXVI Cycle of the Ph.D. Course in *Energy – Low carbon Energetics and Innovative Nuclear Systems* – held at University of Palermo was born from a cooperation between University of Palermo and the ENEA Research Centre. The present work is part of DEMO design activities supported by the EUROfusion consortium, to which University of Palermo is affiliated as a linked third party of ENEA. The research was particularly focused on the thermal-hydraulic and thermomechanical study of DEMO divertor.

The DEMO divertor design is currently under study within the Work Package Divertor (WPDIV) of the EUROfusion actions within the 2021-2027 Framework Programme for Research and Technological Development (FP9) of Horizon Europe.

The current DEMO divertor is made of toroidal assemblies, each composed of a Cassette Body (CB) supporting two Plasma Facing Components (PFCs). The most promising

configuration involves a dual cooling scheme, with two separate cooling circuits for the CB and PFCs, provided with cooling water at different operating conditions.

The cassette design has been revised after the DEMO project Gate Review 1 to use high-temperature (295-328°C) and high-pressure (155 bar) coolant, similarly to the water-cooled breeding blanket, for the CB cooling circuit. These design assumptions pose new challenges in achieving uniform and effective cooling of the structure to ensure reliable operation for the intended divertor lifetime. Moreover, alternative materials for the PFCs supporting Target Bodies (TBs) are under assessment aiming to extend the component's lifetime under irradiation.

The work carried out during the Ph.D. years progressed along two different paths. In a first phase, the main objective was to numerically assess the steady-state thermo-hydraulic performance of the DEMO divertor cooling circuits. In particular, an integrated fluid-structure Computational Fluid-Dynamic (CFD) analysis campaign of the entire divertor cassette was carried out, with the twofold aim to evaluate the CB thermal performance under the revised coolant conditions and to compare the temperature distribution in the TBs by selecting different materials, namely CuCrZr alloy, Stainless Steel (SS) 316 Ti modified, and Eurofer97.

The study was focused, for each cooling circuit, on the evaluation of the coolant pressure drop, coolant flow velocity distributions, coolant temperature and sub-cooling margin distributions, critical heat flux margin distribution among plasma-facing channels, and structure temperature distribution. The activity was carried out following a theoretical-computational approach based on the Finite Volume Method and adopting the commercial CFD code ANSYS CFX.

During the second phase, attention was focused on the structural behaviour of the DEMO divertor as well. In particular, two main aspects were studied. The first one was the behaviour of the CB structure subjected to the high pressure and then, the compliance with the structural design code. In this regard, the CB structural response under the load combination foreseen for a hydrostatic test scenario was assessed, with particular attention to the equivalent stress and displacement fields. Moreover, the verification of the fulfilment of the RCC-MRx structural design criteria was performed.

The work was carried out following a theoretical-numerical approach based on the Finite Element Method and adopting the ANSYS Mechanical commercial code.

Furthermore, the second complementary aspect that requires investigation is the structural behaviour of the plasma-facing surfaces, which are subjected to high thermal and particle fluxes. In particular, the study was applied to a divertor plasma-facing surface which is

supposed to be coated with a thin layer of Tungsten over a Eurofer97 heat sink, similar to the SL and the RPs surfaces exposed to the plasma. In this framework, a theoretical-numerical assessment of the thermal stresses on a typical Tungsten armour was carried out to check whether the influence of temperature-dependent mechanical properties of the materials may affect the results.

The thesis work has been built as follows: Chapter 1 presents some generalities on nuclear fusion physics, DEMO fusion reactor and a general description of the DEMO Divertor. Chapter 2 illustrates models, loads and boundary conditions of the thermofluid-dynamic study on DEMO Divertor, together with the results and outcomes obtained.

Finally, in Chapter 3, the thermomechanical assessment was described, considering the abovementioned parallel activities i.e. the CB structural analyses and the study of thermal stress on the tungsten coating of plasma-facing surfaces.

Chapter 1

1 The Divertor of the EU-DEMO Fusion Reactor

1.1 Notes on nuclear fusion

Exergonic nuclear fusion reactions provide energy when two light nuclei combine to form one heavier nucleus. The mass difference between the reactant and products determines how much energy is generated during a fusion process. In fact, the mass of fusion reaction products is less than that of reactants because they arise as more tightly bound nuclei than reactant nuclei (Figure 1.1).

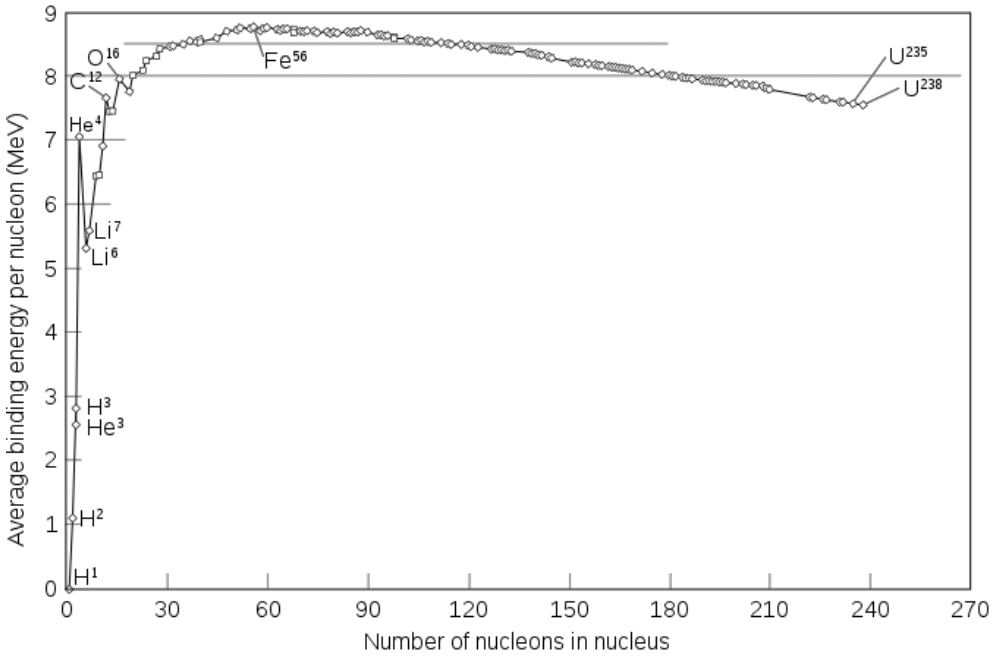

Figure 1.1 Average binding energy per nucleon [5].

The fusion reaction energy output is proportional to the mass defect due to the conservation of energy principle (1.1):

$$Q = (-\Delta m)c^2 \tag{1.1}$$

where the *Q-value* is the energy output of the fusion reaction, $\Delta m = m_{products} - m_{reactants}$ is the mass defect and c is the speed of light in vacuum (i.e. $3 \cdot 10^8$ m/s). It is evident that $Q > 0$ (i.e. energy is released by the reaction) only if $\Delta m < 0$; in this case, the reaction is called exoergic, otherwise it is called endoergic. This means that the additional quantity of mass is converted in kinetic energy of the reactants.

Strong nuclear force and electrostatic force, two of the four fundamental forces of nature, act in opposition to one another to trigger fusion reactions.

The strong nuclear force acts over a small distance and is an attractive force that binds protons and neutrons inside the nucleus. On the other hand, the electrostatic force depends on the relative distance between the particles and is attractive for those with opposite charges and repulsive for those with similar charges.

According to electrostatic principles, reacting nuclei must therefore possess enough kinetic energy to cross the "Coulomb barrier", which is inversely proportional to the square of the distances between the charges and directly proportional to the product of the charges in order to initiate fusion reactions. However, the threshold energy can be lowered because of the quantum phenomenon known as the "tunnel effect".

Particles with energies lower than the Coulomb barrier have a non-vanishing probability of crossing the barrier when quantum mechanical tunnelling is taken into account. A compound nuclear state is created when particles are close enough to one another for the strong nuclear force to overwhelm the electrostatic force.

Since light particles like deuterium and tritium have Coulomb barriers in the range of 0.4 MeV, heating a hydrogen gas to temperatures where a sufficient number of nuclei have energies of relative motions at least in the tens of keV range (roughly 370 keV for Deuterium-Tritium (D-T) fusion) while taking the tunnelling effect into account is required to achieve an acceptable fusion reactions frequency. Considering that hydrogen has an ionization potential of 13.6 eV, at this temperature, in the range of 10^8 K, the gas will be completely ionized in the state of matter defined as plasma. After reaching a sufficiently high temperature, it is necessary to maintain it and confine the plasma for enough time to achieve an adequate number of reactions to get an energy surplus for power production purposes.

Many exergonic nuclear fusion reactions can be promising for both academic and commercial use and they are shown in Table 1.1. Moreover, fusion reactions can be

compared using their cross section, which terms the probability of a fusion reaction as a function of the relative speeds of the impacting particles.

Table 1.1 Principal nuclear reactions [6].

Reaction name	**Reaction**	**Q-value [MeV]**
D-T	$D + T \rightarrow \alpha + n$	17.6
$(D\text{-}D)_P$	$D + D \rightarrow t + p$	4.05
$(D\text{-}D)_n$	$D + D \rightarrow h + n$	3.27
D-h	$D + h \rightarrow \alpha + P$	18.34
D-^{6}Li	$D + {}^6Li \rightarrow 2\alpha$	22.40
p-^{7}Li	$P + {}^7Li \rightarrow 2\alpha$	17.20
p-^{6}Li	$P + {}^6Li \rightarrow \alpha + h$	4.00

While deuterium for D-T reaction is abundant (earth waters have a mean particle density ratio of 1 deuterium particle over 6700 hydrogen atoms), tritium is scarce. It is a radioactive beta emitter with 12.3 years half-life produced on earth by cosmic radiation at a rate of 50 kg per year.

The main supply of tritium in future nuclear fusion power plants is expected to be lithium, through nuclear reactions usually referred to as tritium breeding. It occurs by capture of the fusion neutron in lithium following the two reactions in equation (1.2).

$$ {}^1_0\mathrm{n} + {}^6_3\mathrm{Li} \rightarrow {}^3_1\mathrm{H} + {}^4_2\alpha + 4.7\mathrm{MeV} \quad (1.2)$$

$$ {}^1_0\mathrm{n} + {}^7_3\mathrm{Li} \rightarrow {}^3_1\mathrm{H} + {}^4_2\alpha + {}^1_0\mathrm{n} - 2.5\mathrm{MeV} \quad (1.3)$$

Naturally stable isotopes lithium-6 and lithium-7 are existing with 7.5% and 92.5% abundance, respectively, and in significant quantity on earth making it possible to breed tritium and use it as a fuel [6]. It is anticipated that these events will take place in a blanket, or breeding blanket (BB), enclosing the fusion core in reactors like DEMO.

Every fusion reaction must be followed by at least one tritium breeding reaction. A Tritium Breeding Ratio (TBR) - defined as the ratio of the rate of tritium production in the breeding blanket to the rate of tritium burned in plasma – should be higher than 1 but to ensure the reactor self-sufficiency the minimum value ranges from 1.1 to 1.2.

The most promising approach to exploit D-T fusion reactions for power production is thermonuclear fusion. The process consists in the confinement and heating of a population of D-T atoms in a given space forming a plasma which is expected to achieve thermodynamic equilibrium as a result of stochastic collisions. The resulting energy

spectrum is then represented by a Maxwell-Boltzmann distribution, where most of the desired fusion processes are found in the high energy region of the distribution.

The difficult technical constraint is the preservation of a sufficiently stable high temperature (10^8 °C) plasma in a reasonable volume and for a period of time long enough to make the whole process energetically possible.

Confinement of the fuel ions is thus crucial to preserve these conditions within the required reaction volume. Plasma may be confined by several means (material confinement, gravitational confinement, electrostatic confinement, inertial confinement.). By the way, the most promising methods to exploit fusion reactions are the inertial and magnetic confinements [6].

The oldest magnetic confinement devices were the solenoidal fields, however they proved to be not applicable to fusion power plants due to the high particle leakage occurring at the ends of the solenoid. Leakage could be reduced by using a mirror magnetic field which is a magnetic field whose strength is enhanced at each end of the cylindrical solenoid region. However, the best solution to avoid leakage is to eliminate the ends, which means closing the solenoidal field in order to achieve a Toroidal Field (TF) [6].

In this regard, the most investigated devices are tokamaks and stellarators (see Figure 1.2). Both use a toroidal configuration of the magnetic field to achieve closed particle magnetic confinement. Tokamak is a Russian acronym for “toroidal chamber with an axial magnetic field” and it has become the favoured concept of toroidal fusion reactor. It was invented by Russian physicists Sakharov and Tamm in 1951 and was first experimented at the Kurchatov Institute (Moscow) in the same year.

Tokamak devices use different kinds of magnetic fields, supplied by toroidal, vertical and poloidal field coils, while stellarators use both TF coils and helical windings in alternating directions in order to twist the magnetic field.

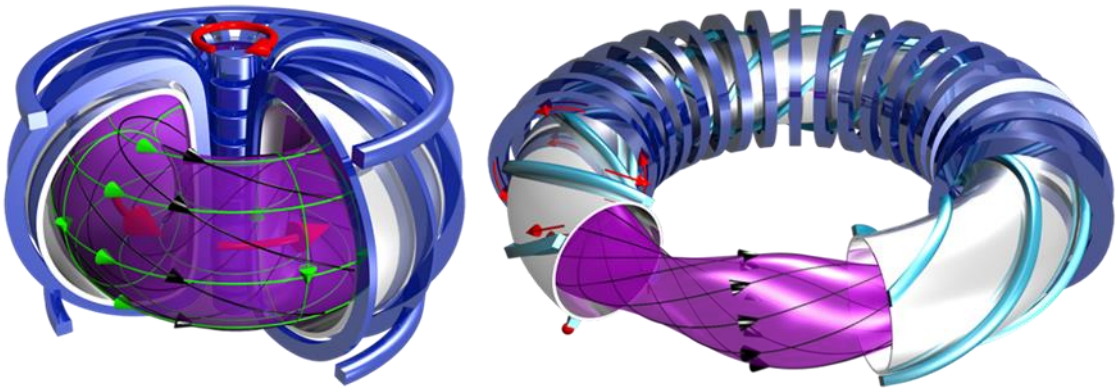

Figure 1.2 Graphics of confined plasmas in tokamaks (left) and stellarator (right) configurations.

By the way, a toroidal device has the main advantage of operating with a closed magnetic field configuration; field lines are therefore confined in the plasma region, and thus offer the advantage of having no ends from which the plasma might escape.

Leakage could occur in TF due to scattering reactions, diffusion across field lines in the radial direction (i.e. particle drifts) or collective particle oscillations (instabilities).

The TF is produced by simply passing a current through a system of coils, each wound around the torus. Because the coils around the torus are arranged closer together on the inboard side than the outboard side, the magnetic field varies radially, giving the particles a drift velocity. Local charge separation is the net effect of the drift, which creates a vertical electric field that causes simultaneous ion and electron drift outward in a direction perpendicular to the principal torus axis.

Thus, the plasma in a simple TF drift outward until the surrounding wall impairing the radial equilibrium and the confinement. To avoid this effect, it is necessary to apply a poloidal magnetic field. Depending upon the relative magnitude of both poloidal and toroidal magnetic fields, a helical path of particle migration occurs. As a result, the particles spend equal time in the two halves of the toroid, therefore cancelling out the charge separation.

The first way to establish the poloidal magnetic field is by placing outside the plasma a set of poloidal coils which generate a current in the toroidal direction; stellarator machines are founded on this principle. Instead, tokamaks use a toroidal current flowing in the plasma, which is a relatively easier solution that currently makes tokamaks of greater interest.

In a tokamak, the plasma torus is considered as a single-winding secondary side of a transformer. The current in the primary transformer induces a current in the plasma torus. The toroidal plasma current ensures Ohmic heating and also generates the poloidal magnetic field. Additionally, stabilizing coils are installed to produce a vertical magnetic field to prevent the plasma from expanding as it naturally would do. The vertical magnetic field produces an inward-directed Lorentz force which prohibits the outward expansion of the plasma. The toroidal plasma current needed to supply the poloidal magnetic induction is generated by a toroidal electric field which is achieved by the time-dependence of the magnetic flux that enters the hole in the torus. It follows, then, that a tokamak is not able to operate in stationary but only in pulsed conditions, unless non-inductive schemes of plasma current drive can be exploited [6].

From a design point of view, all the coils are superconducting in order to minimise dissipation of energy. In a tokamak power plant, plasma is magnetically confined in a torus-shaped vacuum chamber where energetic neutrons and fusion reaction products are produced. Neutrons are then collected in the BB, where they are slowed down, converting

their kinetic energy into heat and are absorbed by lithium atoms to produce tritium. The heat is removed from the blanket by a flow of coolant fluid which feeds steam generators used to produce electricity, exploiting a conventional thermodynamic cycle.

Fusion investigation has been centred on the tokamak confinement idea for the past 60 years, and this development led to the ITER project, the biggest tokamak in the world, and its successor, the DEMO reactor.

In this framework, the ambitious goal of demonstrating electricity production is the main purpose of the European fusion roadmap Figure 1.3. It is based on three elements:

- building and operation of the ITER test fusion reactor as the essential step towards energy production on a fast track;
- building and operation of a DEMOnstration Power Plant (DEMO) as a single step between ITER and a commercial power-producing fusion reactor;
- building and operation of International Fusion Materials Irradiation Facility (IFMIF) for material qualification under intense nuclear irradiation, in parallel with ITER.

The European roadmap reports three separate periods with distinct main objectives [3]:

- Horizon 2020 (2014-2020) with the objective of constructing ITER within scope, schedule and cost. During this period, the foundation of a fusion power plant has to be laid and innovation has to be promoted among industry.
- Second period (2021-2030) with the objective to exploit ITER up to its maximum performance in order to acquire sufficient knowledge for DEMO construction.
- Third period (2031-2050) during which complete ITER exploitation will lead to the construction and operation of DEMO.

The reactor ITER, the largest burning plasma experiment under construction, will produce 500 MW of fusion power with an injected power of 50 MW, so that the fusion gain is expected to be equal to 10. It has been designed with currently available materials and technologies and based on experimental data and theoretical studies of the past decades. With its first plasma originally planned for 2025, it is expected that ITER will progress the knowledge database for tokamak physics and technology further enough to build the first fusion power plant with electric power production capability, DEMO.

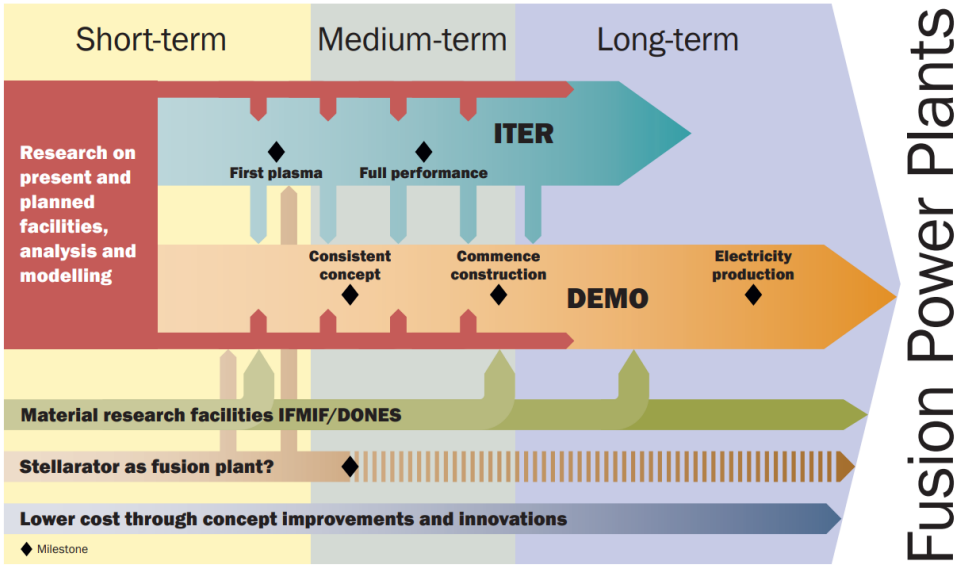

Figure 1.3 EUROfusion Roadmap [3].

The objectives of DEMO are to generate a few hundred megawatts of net electricity for the grid, breed the necessary quantity of tritium to conclude its fuel cycle, and show all the technologies required to build a commercial fusion power plant, including a sufficient degree of availability. To fulfil these goals DEMO will have to rely on simple and robust technical solutions, well-established and reliable regimes of operation and adequate use of materials for the expected level of neutron fluence. These requirements imply extensive ITER exploitation in order to extrapolate technologies as far as possible and pursue innovation both in industries and research laboratories.

1.2 The DEMO fusion reactor

According to the EUROfusion Roadmap [3], DEMO will be a first-of-its-kind facility for the future development of fusion power plants pointed towards commercial application. Many ambitious goals should be obtained through the DEMO project, being [7] [8]:

- the demonstration of net electricity output to the grid (from 300 to 500 MWe) with a 2 GW plasma power;
- the capability to work with a closed fuel cycle with tritium self-sufficiency (TBR>1);
- the compliance with all the safety requirements;
- the qualification of many fusion-relevant technologies;
- several full power years of operation;
- showing the effective environmental sustainability of the process minimizing all the activation waste (no long-term storage).

The construction and the subsequent operation of DEMO will be even divided into three steps well-structured by many other secondary goals. The DEMO Pre-Conceptual Design phase, finalized in 2020, aimed at advancing the technical basis of the DEMO design. In particular, emphasis was placed on the comparison between various plant design options with a reference concept in order to select the configurations with the highest probability of success. These selected concepts will define the basement for the subsequent developments and at the end of that optimization (Conceptual Design phase) only the best configuration will be chosen for the Engineering Design phase, where the final design will be studied [3].

Being the next step after the ITER global experiment, DEMO will largely benefit from the ITER design, construction and operation. Due to its ambitious goals, the DEMO project is going to face significantly stronger technological requirements than ITER. Moreover, most of the design and integration issues should be addressed considering the interdependencies among the critical systems and the uncertainties of the physical and technological assumptions.

In general, a fusion power plant requires a group of components (Figure 1.4 and Figure 1.5) to ensure that plasma will be efficiently and safely controlled and furthermore to obtain a satisfying energy output.

In order to propel all these needs, DEMO architecture will consist of different systems [9]:

- a system of magnets (TF coils, PF coils and central solenoid) to produce the magnetic field which shapes and confines the plasma;
- a Vacuum Vessel (VV), which is a torus-shaped wall performing the primary vacuum and shielding the magnets from neutrons;
- a Cryostat which hosts the magnet system, shielded by a thermal shield from the VV radiations;
- a Breeding Blanket (BB), able to produce tritium, shield VV and coils and remove the thermal power released by the fusion products;
- a divertor, a high heat flux component that is in charge of particles and energy exhausted by the plasma;
- upper, lower and equatorial ports that give access to the in-vessel components (BB, divertor);
- different Primary Heat Transport Systems (PHTSs) which are structures of vessel and in-vessel components cooling pipes transporting the heat from the plasma to the Power Conversion System (PCS). One of the options foreseen in DEMO for the PHTSs, their equipment and the PCS is reported in Figure 1.5;

- the PCS, i.e. the secondary loop to the turbine building (or to intermediate energy storage building). The heat removed from the tokamak by the PHTS systems is transferred through heat exchangers and steam generators to the PCS in order to drive a turbine and to ensure an efficient conversion into electrical power (Figure 1.5).
- heating and current power sources;
- supply and circulation fuel system;
- maintenance and monitoring systems.

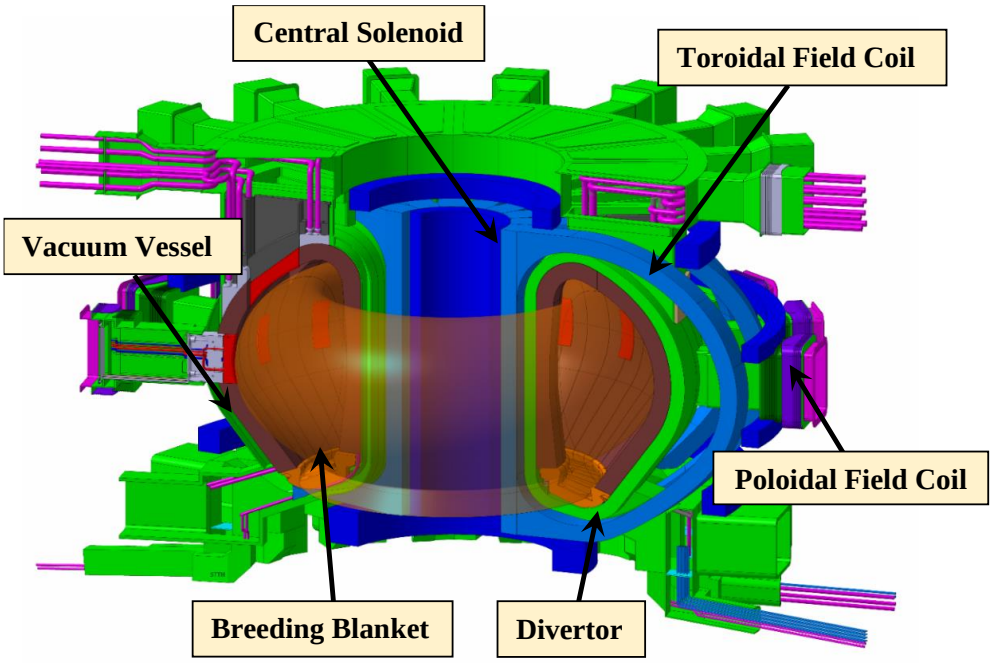

Figure 1.4 DEMO tokamak main systems.

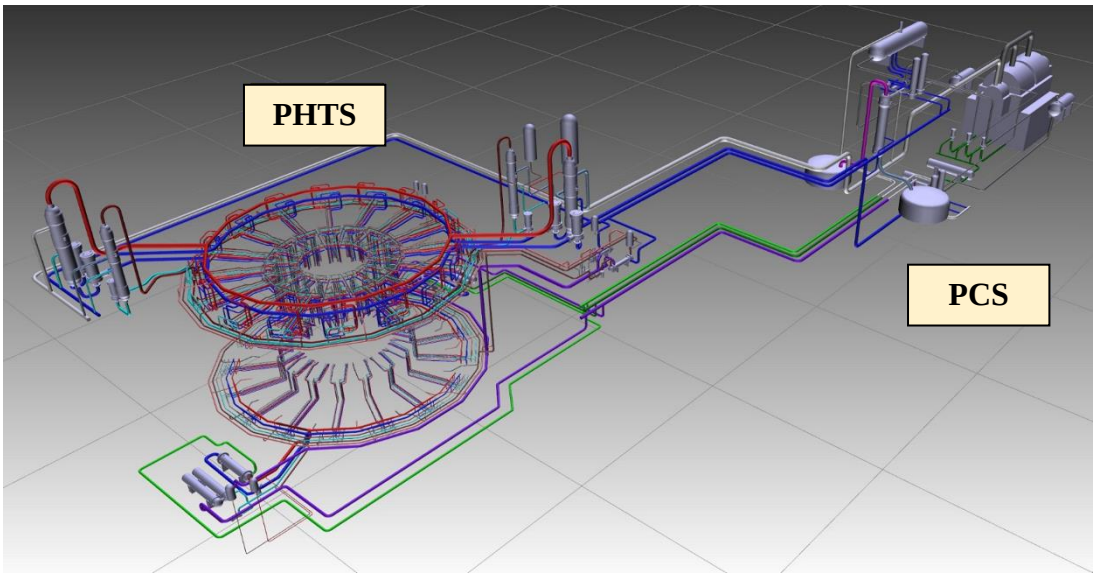

Figure 1.5 DEMO PHTS and PCS 3D model (direct coupling option).

Hence, in DEMO, the divertor and the BB are the key in-vessel components. They have to cope with severe working conditions, posing the need for an adequate cooling capability. Their design is being really challenging and is taking a significant R&D and technological effort from the scientific community. In this dissertation, attention will be focussed on the DEMO divertor cassette, which is going to be described in the following paragraph, and in particular, on the study of its thermal-hydraulic and thermomechanical performances.

1.3 The DEMO divertor

The divertor of the DEMO reactor will carry out many critical functions. Its main role is to remove heat produced by particle bombardment on targets, radiation and volumetric nuclear heating and to form gas flowing channels towards the pumping ports for fusion ashes (helium) and unburnt D-T fuel. Moreover, it shall shield the VV and magnets against nuclear loads and provide plasma-facing surface physically compatible with the plasma (low sputtering, low tritium retention, high melting point) [10].

Plasma particles, with their high kinetic energy, manage to escape the magnetic field lines, heading toward the First Wall (FW) of the blanket where they impact. This leads to physical processes such as localized evaporation and neutron damage. Consequently, the blanket FW is subject to a particle flux and it deteriorates, causing the release of heavy nuclei into the plasma, resulting in a reduction in the rate of the nuclear fusion reaction.

The presence of the divertor is essential for the steady-state or long-pulse operation of the fusion process because the D-T reaction is always accompanied by the production of ^{4}He, which, if it was to remain within the plasma, would affect its performance. In particular, the presence of these helium nuclei inside the plasma shifts the balance of the fusion reaction toward the reactants, reducing the number of effective collisions and increasing the effective atomic number (Z_{eff}) of the ionized mixture, resulting in greater bremsstrahlung radiation emissions and subsequent plasma cooling.

The negative effect of impurities in the dynamics of a fusion reactor can be qualitatively assessed based on the principle of quasi-neutrality of the plasma. According to this principle, plasma, barring high-frequency disturbances, can be essentially regarded as a neutral medium. This principle is analytically expressed in the following equation:

$$n_e = \sum_k n_k < Z >_k \tag{1.4}$$

where n_e is the particle density of electrons per unit volume, n_k is the volumetric density of the *k-ith* ionic species and $<Z>_k$ is the average ionization number of each species. Since H isotopes are fully ionized at the reactor operative temperatures, considering n_i as the ions

volumetric density and defining n_k as the generic density, being a fraction of n_e by means of a parameter f_k, it is possible to obtain:

$$n_k = f_k \cdot n_e \tag{1.5}$$

Combining equations (1.4) and (1.5) becomes:

$$n_e = n_e \sum_k f_k < Z >_k + n_i \tag{1.6}$$

Dividing each member of the (1.6) for n_e:

$$\frac{n_i}{n_e} = 1 - \sum_k f_k < Z >_k \tag{1.7}$$

At high operative temperatures, the energetic losses due to bremsstrahlung radiation are proportional to n_e^2, while the number of fusion reactions is proportional to n_i^2. Thus, to optimize the process, the left-hand side of equation (1.7) shall be maximized. It happens if the concentration of impurities is as low as possible, then if the f_k parameters are minimized.

To this end, the aim is to obtain a field configuration which will produce a Lorentz force able to divert these particles towards a reactor region far enough from the plasma.

This magnetic field configuration inside the VV is feasible due to the introduction of a complex divertor system in the lower part of the machine.

The divertor function is, then, to model the poloidal profile of the magnetic field so that the Last Closed magnetic Flux Surface (LCFS) results in a magnetic bounding surface, namely separatrix, which contains closed magnetic surfaces and is surrounded by open surfaces converging in the divertor itself.

Consequently, the plasma is confined within the separatrix, while the plasma Scrape-Off Layer (SOL), outside of the separatrix, contains particles directed towards the divertor. As a consequence, He particles and any heavy elements inside the SOL, due to the Lorentz force, follow helical paths around the magnetic field lines. These particles then collide on the divertor outer surface at low incident angles and release their energy.

The interaction between the divertor and the particles, and their subsequent neutralization, causes an increasing gas pressure near the divertor area and facilitates their extraction by means of vacuum pumps [11].

The actual layout adopted for DEMO is the ‘single-null’ divertor concept, depicted in Figure 1.6, where the divertor is positioned at the bottom of the VV and the SOL field lines intersect at one point (null) [10].

The divertor is then a component subjected to extremely high thermal flux, with peak values around 20 MW/m^2 under off-normal operating conditions, which could be exceeded

for a short period of time during accidental plasma scenarios (for instance, the maximum heat flux density on the target during reattachment can reach up to 40 MW/m² depending on power exhaust strategy).

Due to the aforementioned reasons, the divertor has a crucial role in maintaining the delicate equilibrium that allows fusion reactions to take place. To this end, the design of this component is a serious challenge from hydraulic, thermal and mechanical points of view.

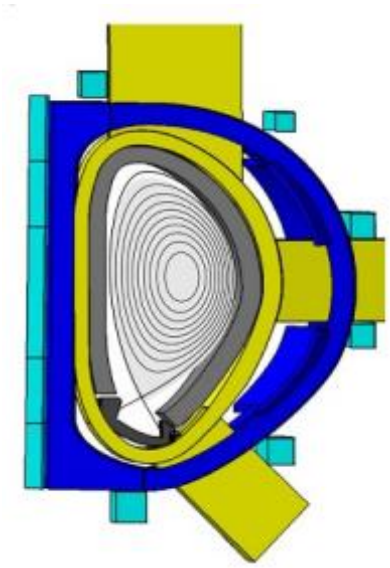

Figure 1.6 Single-null Divertor configuration [12].

Different cooling options have been analysed throughout the last years for the DEMO divertor and they are listed as follows:

- double-circuit cooling option, which foresees two hydraulically separated cooling circuit, one for the Cassette Body (CB) and one for the Plasma-Facing Components (PFCs);
- alternative configuration with an integrated single-circuit cooling option with inlet pressure and temperature of 5 MPa and 130 °C.

According to the DEMO divertor baseline, the circuits were operated with inlet pressure and temperature of 5 MPa and 130 °C, for the PFC cooling circuit and 180 °C and 3.5 MPa for the CB cooling circuit. However, in the last years the possibility to operate the CB cooling circuit at Water-Cooled Lithium Lead (WCLL) BB operating conditions is being explored. The advantages of such operating conditions, being inlet pressure and temperature of 15.5 MPa and 295 °C, respectively, are an increased component lifetime, due to reduced neutron damage, and more simple tokamak cooling system configuration, eventually integrated with the BB cooling system [13].

In this Ph.D. dissertation, attention is focused on the latter cooling option foreseen for the DEMO divertor cassette cooling system, which is described in the following paragraph.

Moreover, for the sake of completeness, the single-circuit cooling option is also briefly described in paragraph §1.3.2.

1.3.1 Double-circuit cooling option

The DEMO divertor baseline design and the main technological options were established following the conclusion of the Pre-Conceptual Design phase of the project, in 2020 [14].

The DEMO divertor design is currently under study within the EUROfusion Work Package Divertor (WPDIV). Its double-cooling circuit configuration was defined in 2017 [15] and then further updated in the following years [16, 17, 18]. The actual configuration, on which this dissertation is focussed, is the 2022 design [18], corresponding to the aforementioned double-circuit cooling option operated with WCLL BB conditions.

The DEMO divertor is made up of 48 separate modules in the toroidal direction arranged in 16 sectors, each one consisting of three modules, i.e. two side cassettes and one central cassette, almost identical and separated by a space of 20 mm. Each sector has a lower port acting as a passage for the feeding pipework and for the cassettes installation and maintenance. The toroidal angular range of a sector is 22.5°, while a cassette module occupies the toroidal angular range of 7.5°.

The number of TF coils and the number of sectors is equal. The best balance between the BB maintenance port spacing and the intensity of magnetic field ripples is predicted to be achieved by 16 TF coils in the DEMO baseline. The fewer number of TF coils in DEMO permits a larger toroidal space accessible for remote maintenance of a BB segment through an upper port. However, a lower number of cassettes has the impact of increasing the thermal power on each cassette, consequently requiring a larger cooling capacity per cassette.

In Figure 1.7 the CAD model of a divertor cassette is reported, where it is possible to identify its PFCs, being the two Vertical Targets (VTs), i.e. Inner Vertical Target (IVT) and Outer Vertical Target (OVT), the Shielding Liner (SL) and the Inner and Outer Reflector Plates (RPs).

Each cassette module includes two target surfaces on which the incident SOL particles are stopped, a Cassette Body (CB) which holds the shielding components and the targets, protecting the VV, the pipes and the pipework of the cooling circuits. Accordingly, the main characteristics of the identified sub-systems listed above are described in the following.

The CB hosts and holds all sub-components of a cassette module (see Figure 1.7). A square-shaped pumping channel is located in the middle region entering through the CB. This duct is the main gas flow channel towards the pumping ports.

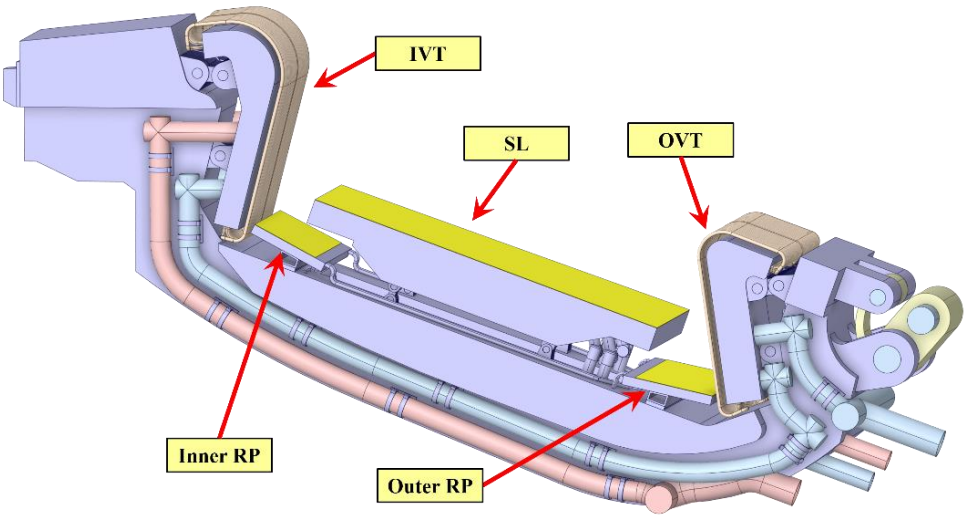

Figure 1.7 DEMO Divertor CAD model 2022.

The CB is made of many internal compartments separated by ribs (see Figure 1.8) and it is entirely made of Eurofer97 steel [1]. At the same time, the ribs act as stiffeners for structural robustness and as partition walls for the coolant that flows through the ribs' holes. The ribs are 20 mm thick and their layout was changed in 2022 considering the higher operating pressure of the coolant (from 3.5 MPa to 15.5 MPa). For the same reason, the external plate thickness was increased from 30 mm to 40 mm, according to "EN 13445-3 2015 Pressure vessel of rectangular section" [18]. Moreover, due to the higher pressure, the thickness of the inlet and outlet CB pipes was increased as well, from 2.5 mm to 5 mm, with respect to the previous divertor design [18].

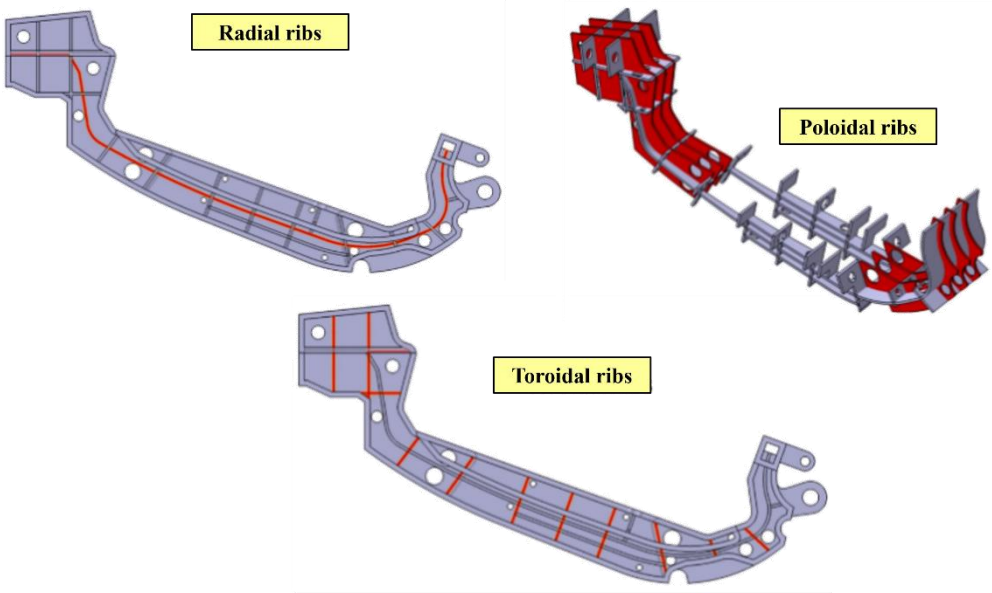

Figure 1.8 Divertor CB internal ribs.

The CB serves as a supporting structure for its shielding structures, i.e. SL and RPs. The SL replaced the so-called dome of the ITER divertor for shielding and gas compression, in order to simplify the design and manufacturing, reducing production costs.

The SL structure, reported in Figure 1.9, hosts four levels of radial cooling channels, for effective cooling and moderation. The cooling path inside of the SL is connected in series with a forward and return flow. The SL First Wall (FW) side is made of a parallel arrangement of 53 cooling channels having a diameter of 12 mm. The other three layers are cooled by large quasi-rectangular cooling channels.

The uppermost front face channels, which are exposed to the highest nuclear heating power density, receive the coolant intake from the inlet pipes first. The coolant is then directed towards the bottom and via the underlying cooling channels before returning via the output pipes to the CB.

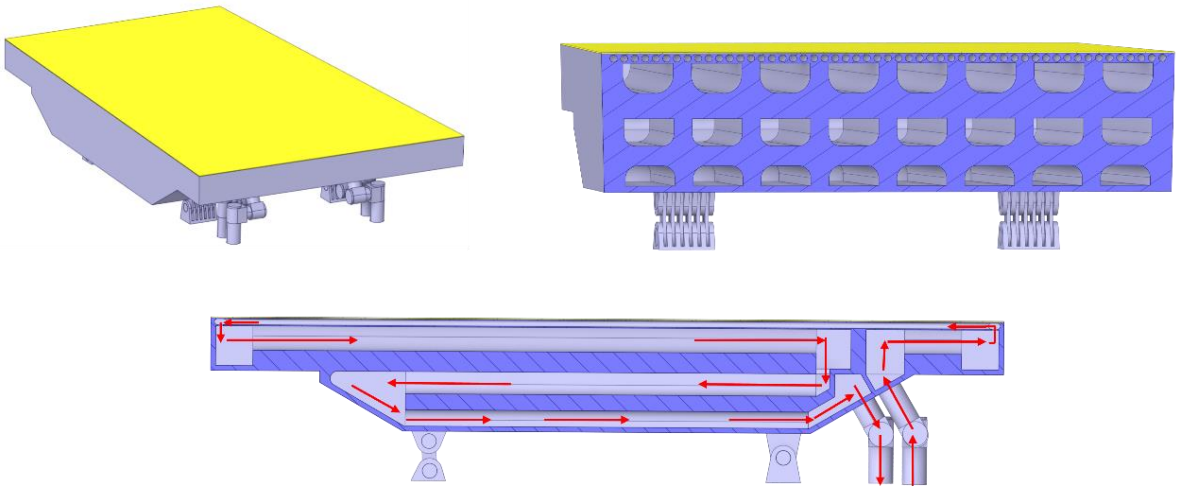

Figure 1.9 Divertor SL and sections.

Due to the higher operating CB pressure, only the top layer thickness was recently changed from 7 mm to 8 mm [18]. The SL structural material is Eurofer97. To ensure low sputtering yield and physical compatibility with the plasma, the front face of the steel plate is coated with a 2 mm-thick tungsten layer (in yellow in Figure 1.9). This coating also serves to shield the structure from radiation, gas particles, and neutron flux. The SL's differential thermal expansion in relation to the CB is made possible by the four multi-link supporting legs. Every leg has two outboard single hinges as well as two double hinges on the inboard (Figure 1.9). Moreover, the dimension of these legs was minimized to prevent overheating by nuclear heating since they are not actively cooled.

The RPs were introduced in 2019 [14] to protect the feeding pipes of the VTs and their manifolds from neutron irradiation. Since the PFC structure was deeply revised in the last years, and the PFC distributors are no longer present [19], the RPs are currently intended

only to protect the cassette from off-normal plasma transients. More in detail, RPs, whose 3D model is reported in Figure 1.10, are structural components made of Eurofer97 with armoured plasma-facing surfaces of 2 mm thick tungsten. In the last configuration, the RPs were moved closer to the CB, changing the dimensions of the supports and, at the same time, improving the pumping performances through the gap between the SL and the RPs.

The cooling circuits of the inboard and outboard RPs are connected in series and they have an analogous internal configuration to the SL. In particular, each RP is made of two layers of cooling channels cooled in series. Inboard and outboard RPs layers are made of parallel arrangements of 39 and 35 circular cooling channels, respectively, whose diameter is 12 mm. The two RPs are connected to each other and to the CB cooling circuit by a set of four manifolds arranged in parallel whose internal diameter is 12 mm. Moreover, in 2021 some advancements were made to the cooling circuit [20] by increasing the volume of the internal manifolds in order to improve the distribution of coolant among the RPs FW channels of the 2019 configuration [21].

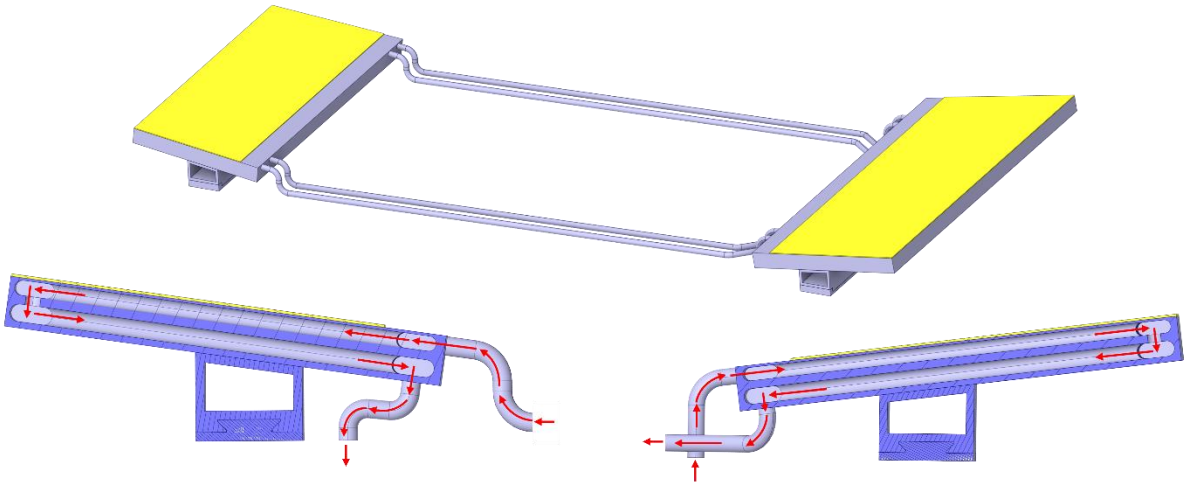

Figure 1.10 Divertor RPs, flow path and RPs section.

The RPs supporting structures were revised during 2022 and a dovetail support, shown in Figure 1.11, was adopted as a current reference solution. The previous configuration was equipped with a system of hinges and double hinges, similarly to the SL, However, this support system was changed because of the high temperatures reached due to nuclear heating [20]. The dovetail solution presents an empty support box to reduce the nuclear heating. It is fixed to the CB by means of a dovetail mechanism, where the rail is welded to the CB.

Alternative design solutions for the RPs supports, like an active cooled supporting system, are currently under investigation within the WPDIV.

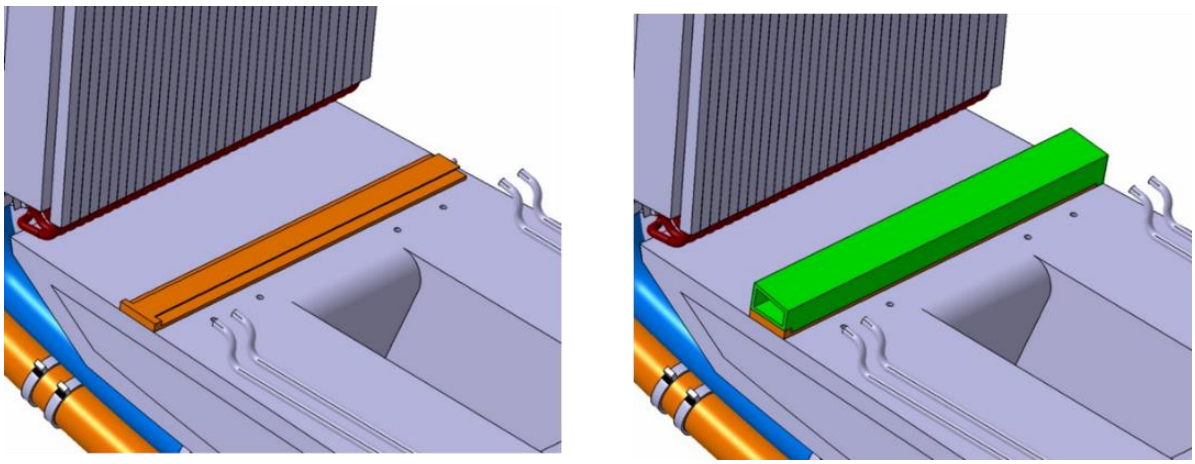

Figure 1.11 RPs dovetail support.

Another crucial subsystem located in the vacuum pumping hole is the Neutron Shield (NS). It was introduced in 2020 to achieve the objective of 2.75 displacements per atom (dpa) on the VV over 30 full power years, highlighted during the WPDIV final review panel report [22]. It consists of two Eurofer97 plates located in the vacuum pumping hole and connected to the cassette body cooling water. Several designs of NS plates were investigated and analysed from the neutronic point of view [23] and an optimal configuration was designed in 2021. It consists of a system of two plates (Upper NS and Lower NS) of 60 mm, cooled by four independent cooling circuits (see Figure 1.12).

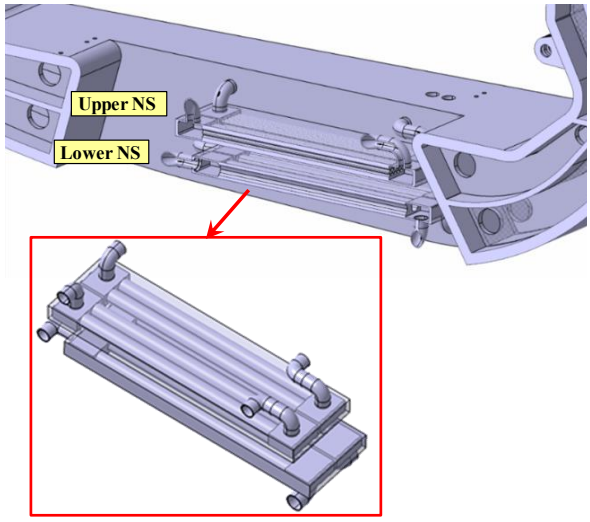

Figure 1.12 Divertor NS.

Each NS is cooled by two parallel and separate sub-circuits, where the coolant is first routed to 4 circular channels, whose internal diameter is 40 mm, fed in parallel by two headers and then collected in the other two parallel headers. Each cooling section is made of two circular channels in the radial direction.

The fluid domain of the CB cooling circuit and its nomenclature are then reported in Figure 1.13 and Figure 1.14, while the whole cooling path is reported in Figure 1.15.

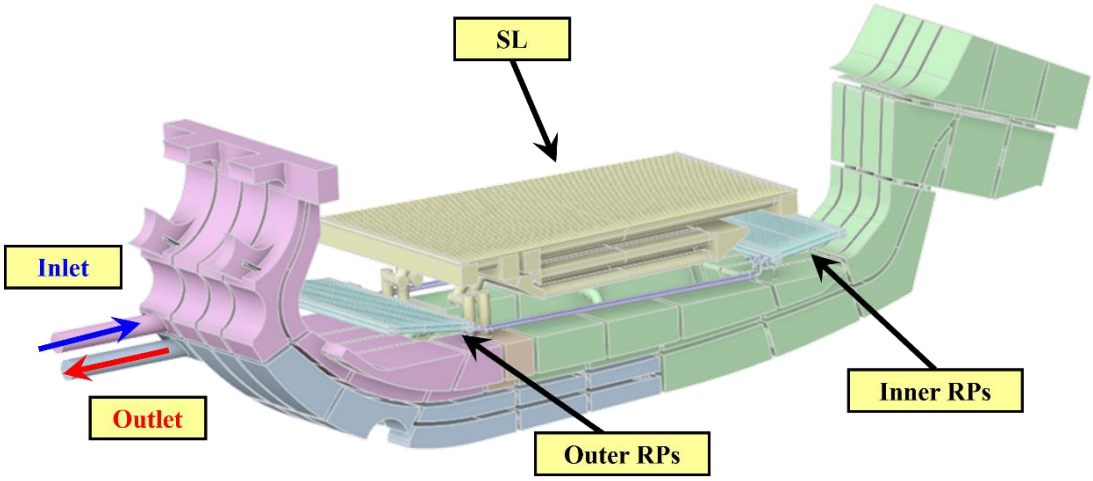

Figure 1.13 Divertor CB fluid domain.

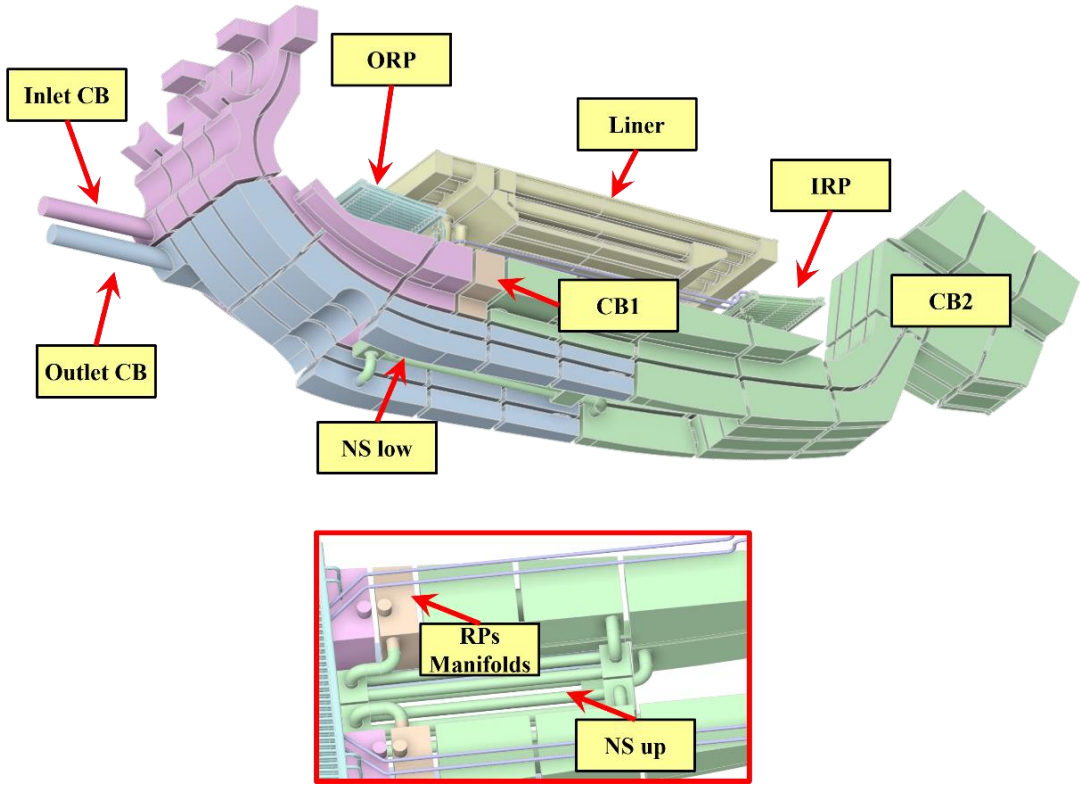

Figure 1.14 Divertor CB cooling circuit main components.

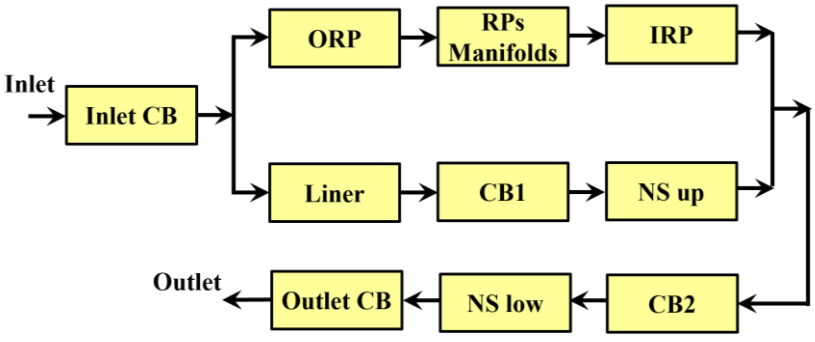

Figure 1.15 Divertor CB cooling circuit cooling path.

The flow is routed from the inlet pipes to the "Inlet CB" box, feeding two parallel branches one parallel path connects Outer RP (ORP), the RP manifolds and the Inner RP (IRP). The other one feeds the SL and the Upper NS. Water is then collected to the inboard box of the CB (referred to as "CB2") and routed to the Lower NS in series with the "Outlet CB" box.

Inboard and outboard RPs cooling circuits are fed in series with the SL and the upper NS cooling circuits and in series with each other. The upper NS cooling circuits are fed in series with the CB, while the lower ones are fed in parallel with the RPs and in series with the SL.

The divertor cassette is connected at its inboard and outboard sides to the VV via different kinds of fixation systems, shown in Figure 1.16.

The "two nose" concept has been designed for the inboard attachment system to decrease the gap to the BB during the installation movement and to be engaged in the VV to react to radial moments. Inboard divertor supports are in radial contact with the VV in the installed configuration, controlling the position of the targets. Both VV support and divertor "nose" are custom machined for tight tolerances.

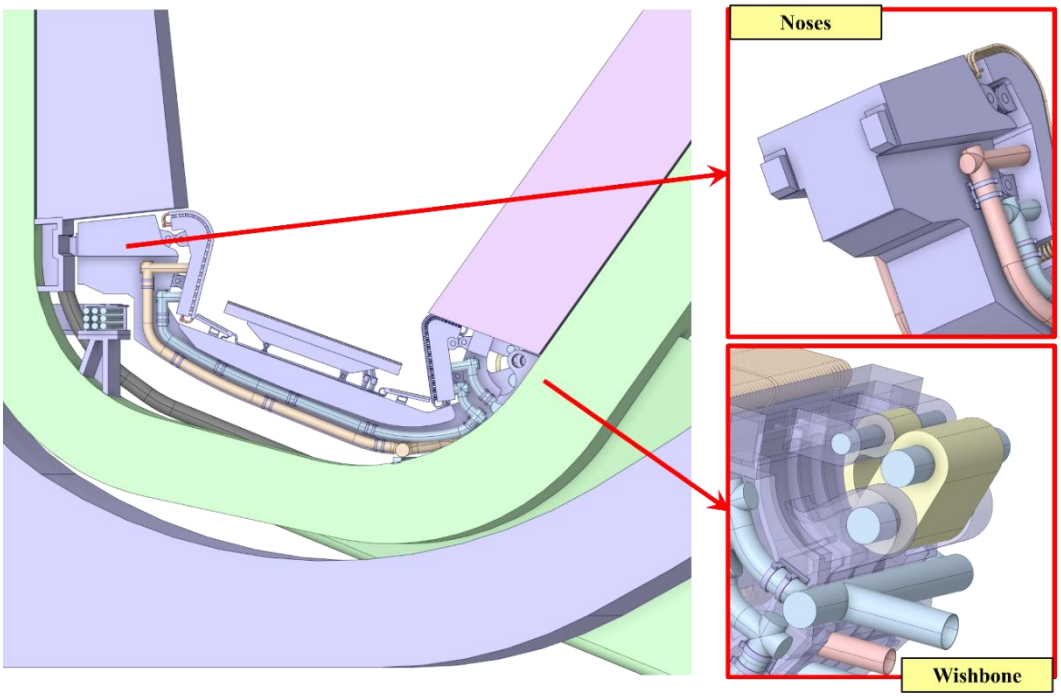

Figure 1.16 Inboard and outboard divertor fixation systems.

The outboard fixation is made with a component called wishbone. Its objective is to improve the flexibility of the outboard attachment avoiding complex spring mechanisms. It has also to withstand load in any direction ensuring electrical continuity. The aim of this layout is to obtain a proper elastic system allowing radial expansion and to transfer vertical and toroidal loads at the same time. From a first assessment, the alloy Ti6Al4V has been selected for its elasticity properties [24].

Each cassette module is equipped with targets, namely Inner Vertical Target (IVT) and Outer Vertical Target (OVT), which are the most significant and technologically critical components of the divertor. They were deeply revised after 2019 and the updated model and cooling scheme are shown in the following Figure 1.17.

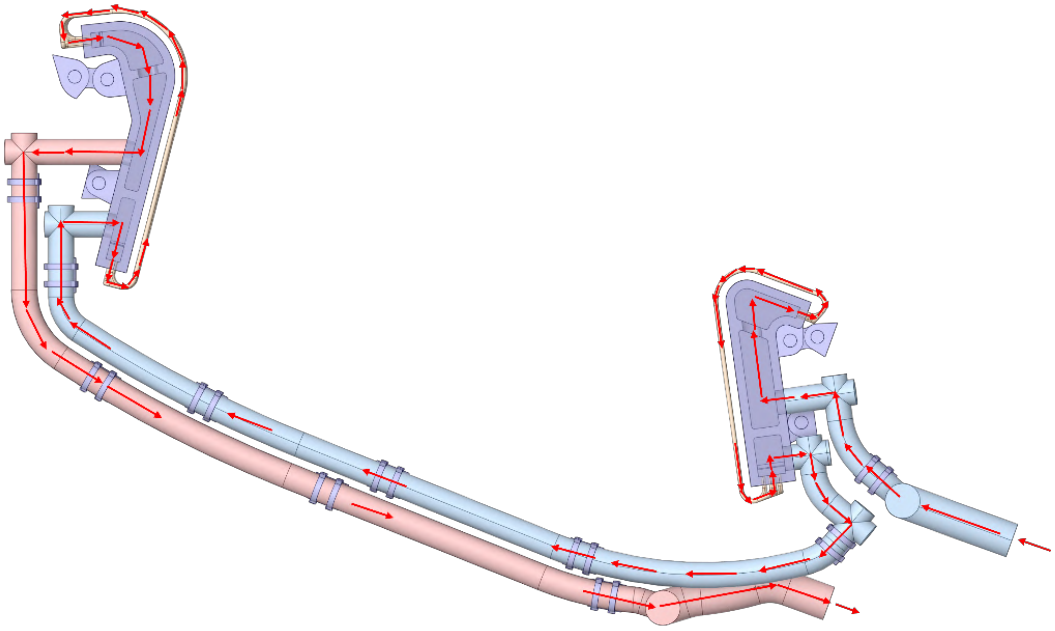

Figure 1.17 Divertor PFC circuit and cooling scheme.

The actual VTs configuration foreseen for the double-cooling option has the same structure as the single-cooling solution presented in 2021 [17]. In particular, they have their own body, called Target Bodies (TBs), connected to the CB by an ITER-like multi-link system (Figure 1.18). The two VTs are fed in series with each other and each VT is connected to the PHTS feeding pipes by a couple of inlet and outlet pipes whose diameter is 120 mm.

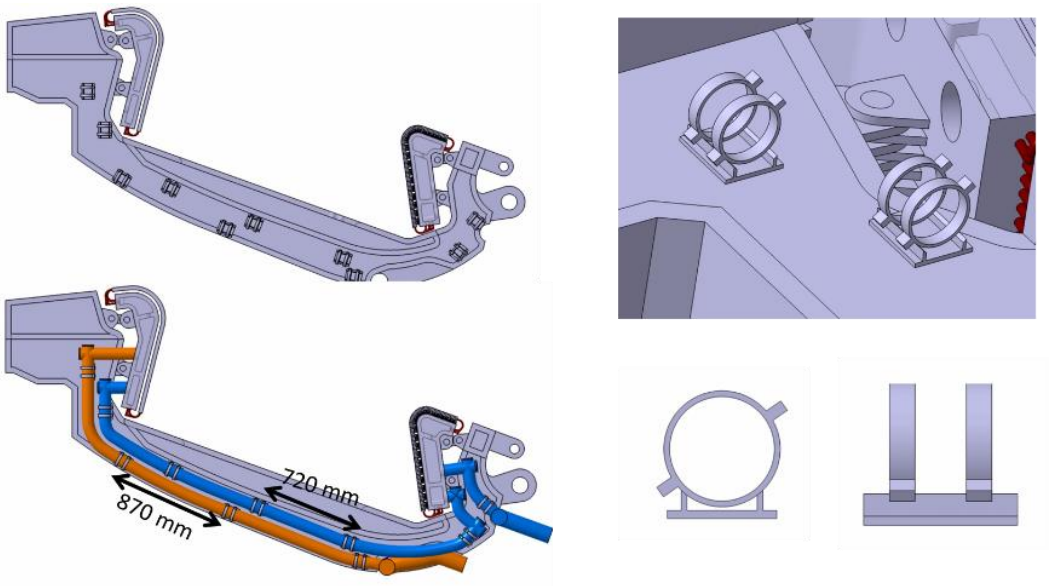

Figure 1.18 Cooling pipes supports.

The VTs cooling circuits are comprised of a parallel arrangement of 34 and 46 actively cooled Plasma Facing Units (PFUs) for the IVT and the OVT, respectively, each one provided with Swirl Tapes (ST) heat transfer performance enhancers (Figure 1.19). Moreover, each VT is made of two independent toroidal assemblies, comprising the TB, which can be removed from the cassette during maintenance.

Every PFU element is composed of a longitudinal array of rectangular tungsten armour blocks connected by a long cooling pipe (CuCrZr alloy [25]) passing through the centre bore of the blocks. To account for the blocks' differing thermal expansion, a 1 mm thick copper interlayer connects the pipe to the blocks.

A representation of the two VTs with the detail of a PFU assembly is shown in Figure 1.19.

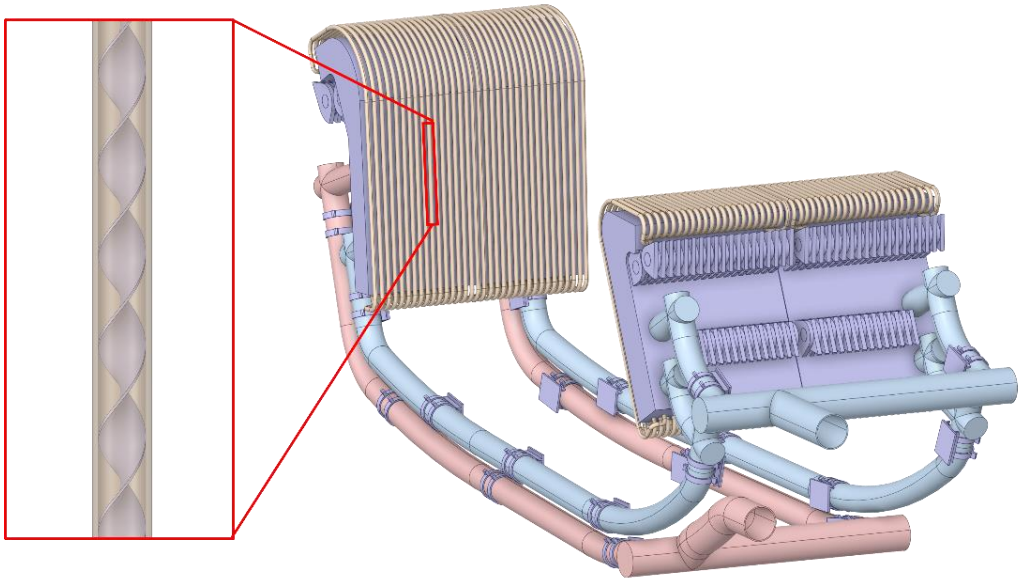

Figure 1.19 Divertor PFC ST detail.

To improve heat transfer efficiency, each channel has a thin (0.8 mm) copper ST turbulence promoter. For the IVT, the ST extends 575 mm, and for the OVT, 493 mm, along the straight portion of the canal. It should be noted that the cross section of every PFU channel is the same. Every monoblock has the dimensions of a parallelepiped, measuring 23 mm in width, 28 mm in height, and 12 mm in depth.

The thermal power density is converged on a thin band of the targets, around the so-called strike point, where high heat flux values occur. The strike point is expected to be placed at the central area of the targets with a Gaussian distribution of power density. The strike point will be swept over a poloidal range of ±200 mm in case of off-normal plasma reattachment events to moderate the time-averaged heat flux. The strike point on the target is in the poloidal centre of the straight part of the VTs which has a total length of 700 mm [10].

Figure 1.20 depicts a typical target element segment. The clear gap between tungsten monoblocks is 0.5 mm in both toroidal and poloidal directions and it is uniform over the entire target areas including the curved baffle region.

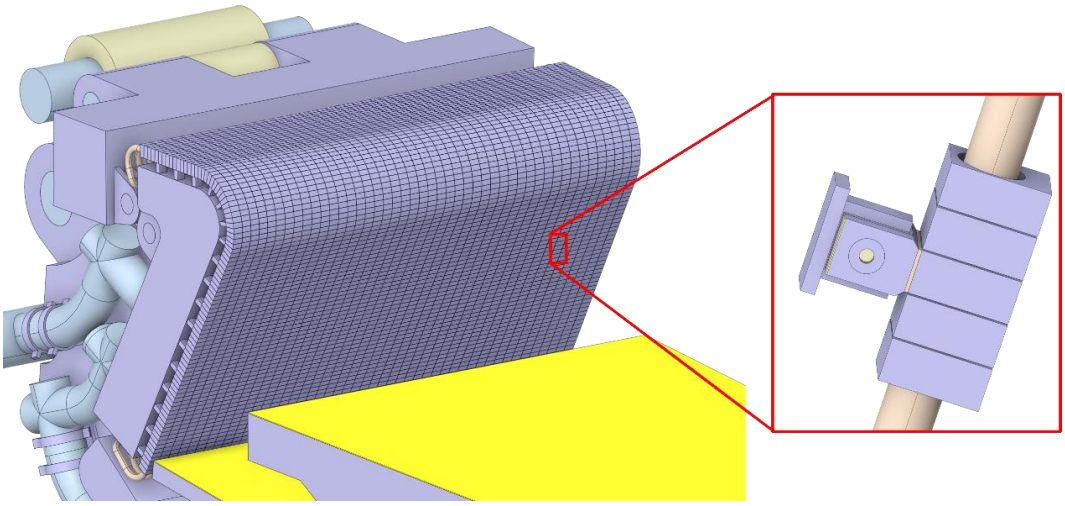

Figure 1.20 PFU supports and tiles.

Considering that the current design was produced in the framework of the DEMO PCD phase, where the details are still beyond the scope, these were not dealt with but shall be defined in the later engineering design phase [10].

The monoblocks placed along the PFU are fixed to the TBs by means of supports located every 5 monoblocks [24]. The support consists of four components that mechanically connects PFU and TBs: a support plug, a support leg, a pin and the pin locks (see Figure 1.21). The unit is made of Eurofer97 steel. The attachment legs are brazed to the tungsten blocks while the legs are fixed to the plug by a pin and two pin locks at both extremities.

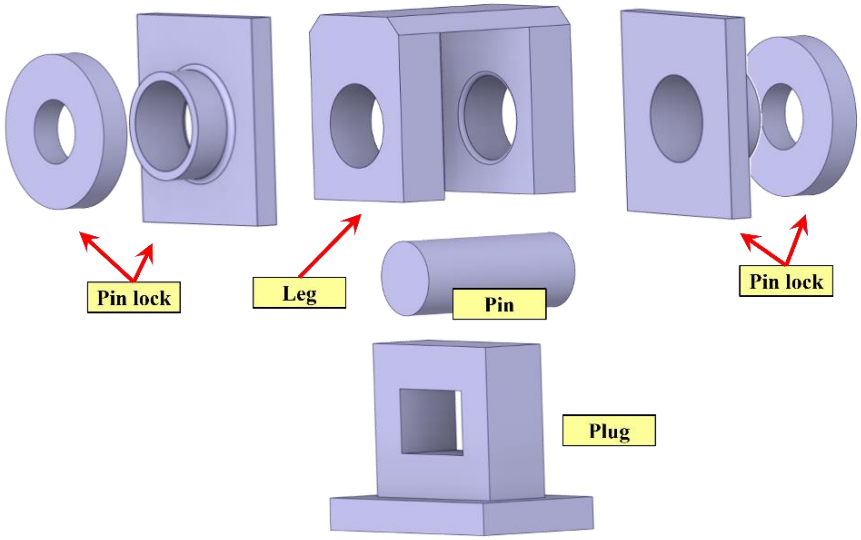

Figure 1.21 Support exploded view.

In the lower zone of the support plug, there is a rectangular support of 4 mm high that will be first inserted in a dedicated hollow designed inside the VTs surface and then welded. In the upper part, there is an elongated hole that enables the pin to slide inside, allowing thermal expansion and avoiding stresses inside the monoblock.

The pin represents the anchoring element between the support plug and the support leg. Some insulating ceramic layers are interposed in some areas to electrically insulate the VTs from the PFU. They are located between the leg and the plug and between the upper part of the leg and its basis and, respectively, the monoblock and the VT TBs.

The fluid domain of the PFC cooling circuit and its nomenclature are reported in Figure 1.22, while the whole cooling path is reported in Figure 1.23.

The flow inside the PFC cooling circuit is routed from the inlet pipes to the two TBs, acting as feeders for the PFUs, then it is collected to two separate outlet manifolds and finally routed back to the PHTS.

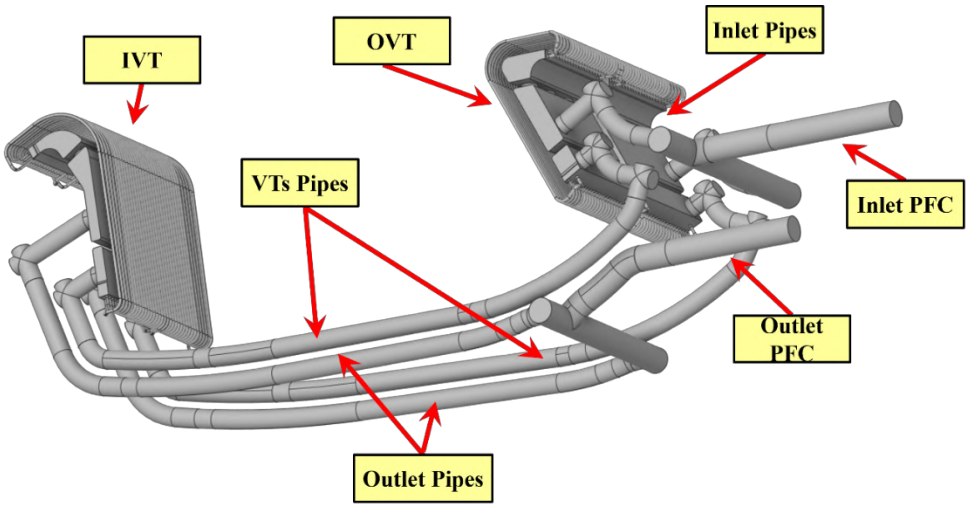

Figure 1.22. Divertor PFC cooling circuit main components.

Figure 1.23. Divertor PFC coolant flow path scheme.

1.3.2 Single circuit cooling option

An alternative option to the baseline double cooling circuit divertor configuration is represented by the single-circuit cooling option, thoroughly illustrated in [17]. This alternative concept was first developed in 2020 [16] and then improved in 2021 [17], exploring the possibility of adopting a single cooling circuit for both PFCs and CB. This solution was proposed with the aim both to ease the remote maintenance and to permit for a cleaner balance of plant design and integration [22], requiring a single PHTS.

From the architectural point of view, this cassette design (Figure 1.24 and Figure 1.25) is made of two VTs, an SL, two RPs, and two NSs hydraulically and mechanically connected to a supporting structure, commonly referred to simply as CB.

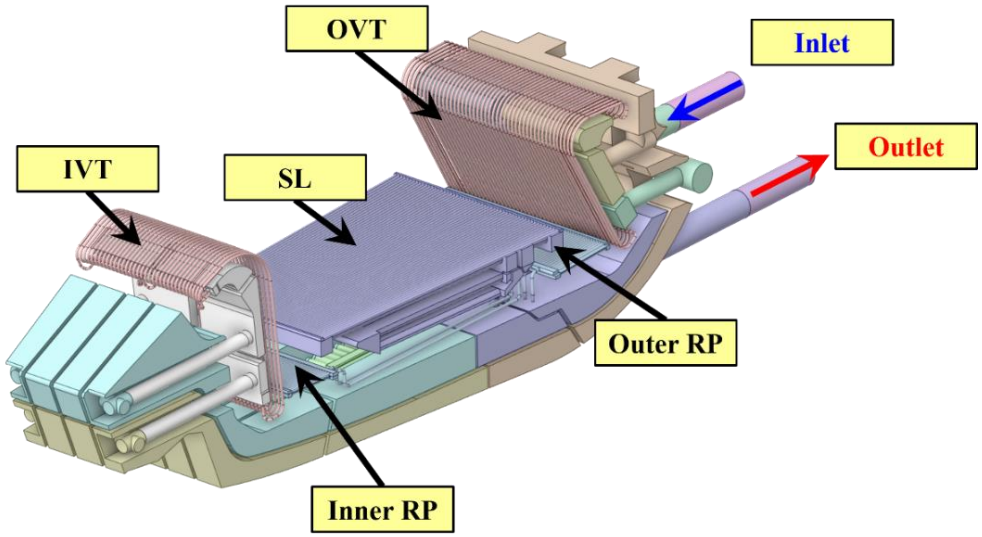

Figure 1.24. Divertor fluid domain.

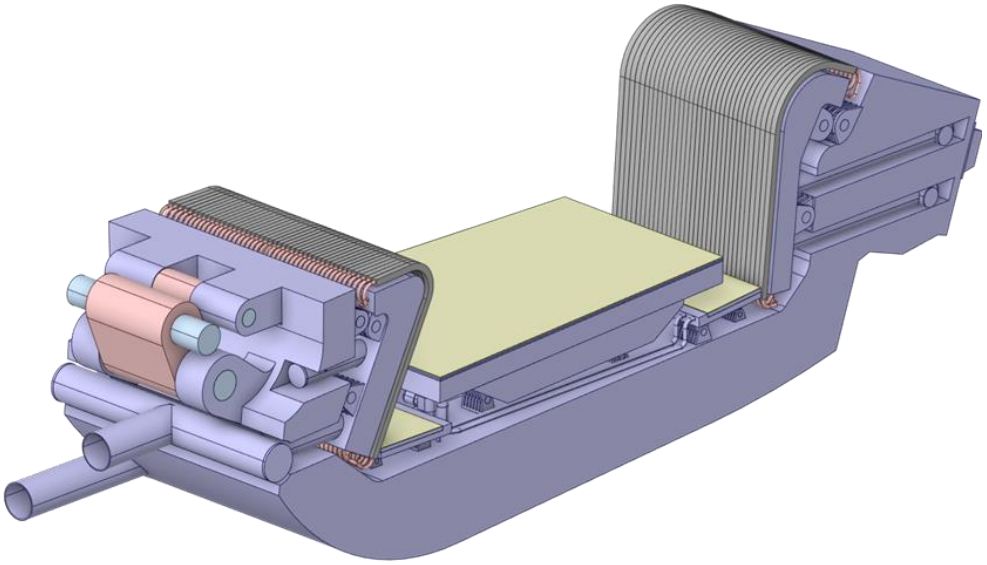

Figure 1.25. Divertor structure domain.

To ease the comprehension of the complex fluid routing inside the divertor cassette, the location of the above-mentioned components is depicted in Figure 1.26, whilst their connections sketched in Figure 1.27.

The two VTs are fed in series with each other and with the CB. Each VT is connected to the CB by a couple of inlet and outlet pipes whose diameter is 70 and 87 mm, respectively for IVT and OVT. The flow is routed from the inlet pipes to two separated TBs, acting as feeders for the PFUs, then it is collected to two separate outlet manifolds and finally routed back to the next box of the CB.

The VTs and the SL cooling circuits have the same configuration foreseen for the double cooling option (§1.3.1).

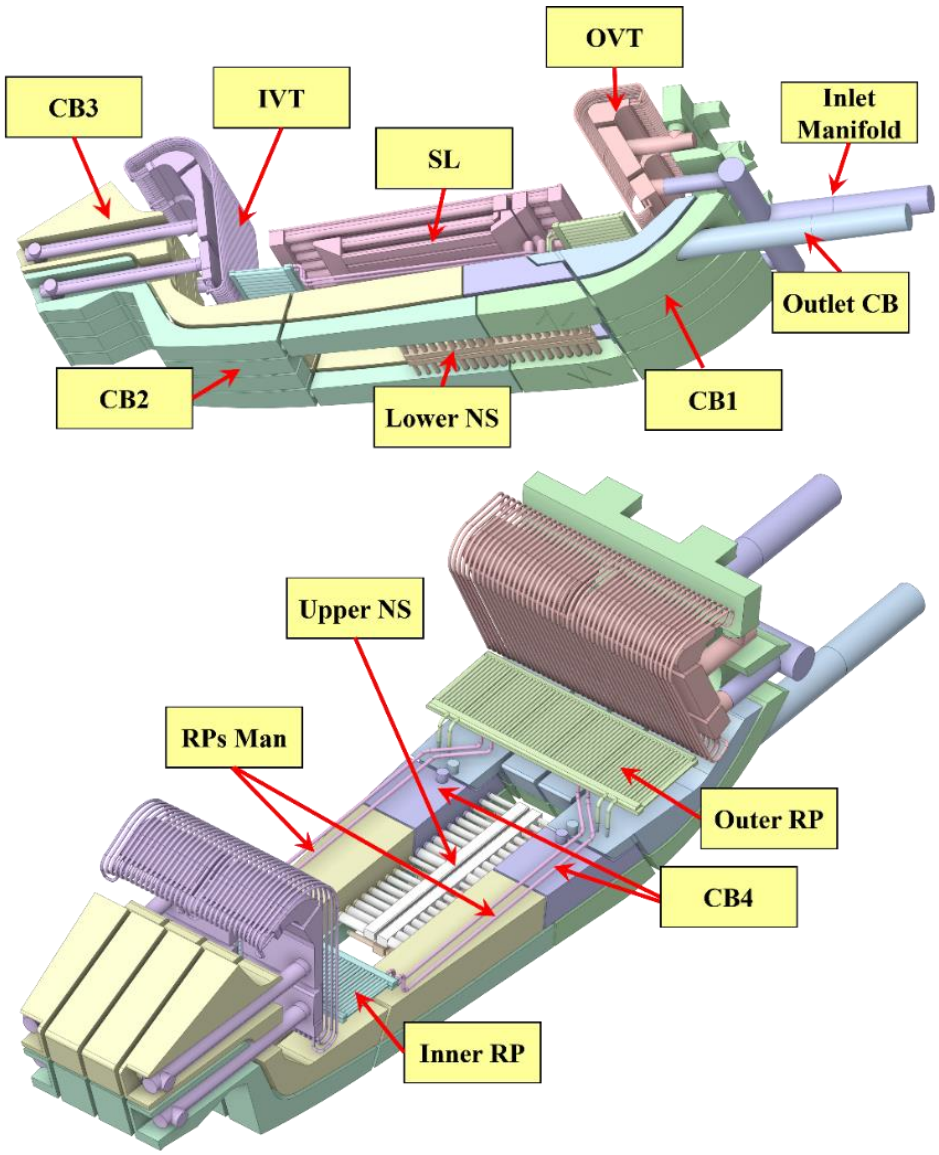

Figure 1.26. Divertor cassette main components.

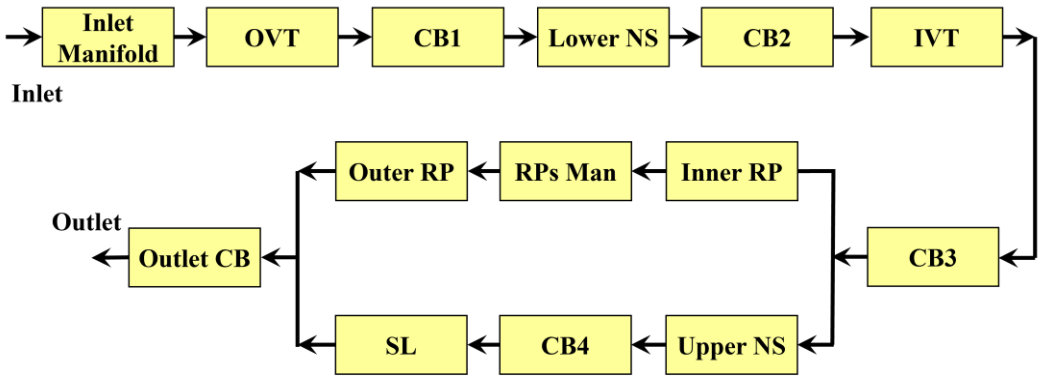

Figure 1.27. Divertor cassette coolant flow path scheme.

IRP and ORP cooling circuits are fed in parallel with the SL cooling circuit and in series with each other. Analogously to the SL design, RPs cooling circuit is made of two layers of

cooling channels in series. IRP and ORP FW layers are made of parallel arrays of 61 and 49 circular cooling channels, respectively, 12 mm in diameter. The other layer is cooled by semi-circular large cooling channels both for inboard and outboard RPs. The two RPs are connected to each other and to the divertor cooling circuit by a set of four manifolds arranged in parallel whose diameter is 15 mm.

One of the two NS cooling circuits is fed in series with the CB, while the other one is fed in parallel with the RPs and in series with the SL. Each NS is cooled by two parallel and separate toroidal sub-circuits, where the coolant is first routed to a radial header fed in parallel by 20 circular channels and then fed back to the CB through 20 more channels, whose internal diameters are variable along the radial direction, as a result of the preliminary fluid-dynamic optimisation campaign performed as part of thermal-hydraulic research activities carried out in 2021 by the University of Palermo [20].

The underlying CB is cooled employing a complex arrangement of box-shaped volumes and acts both as a supporting structure, as previously mentioned, and as a coolant header for the supported components' cooling circuits. In fact, VTs, SL, RPs, and NSs are mechanically connected to the CB structure. In particular, VTs, SL, and RPs are connected to the cassette through two couples of hinges designed to accommodate their thermal expansion, while the NSs are directly welded to the CB.

However, this option is actually not considered since several design reviews are necessary, considering the main outcomes of [26]. The research study showed that the adoption of a single-circuit cooling option divertor for the EU DEMO may pose some severe criticalities. It is not possible to fulfil requirements, especially considering acceptable pressure drops and sufficiently high CHF margin while guaranteeing a suitable divertor lifetime.

Chapter 2

2 Thermofluid-dynamics of DEMO Divertor Double Cooling Circuit Option

2.1 Introduction

A reliable solution for heat exhaust and helium removal is one of the main topics of the EUROfusion European Roadmap [3]. The DEMO divertor will fulfil this function but, due to the harsh environment to which it is subjected, its design is one of the greatest challenges for the DEMO project. As part of the activities planned for this Ph.D. dissertation, the investigation of the thermal-hydraulic performances of the divertor assembly cooling system was carried out.

Due to the very high heat and particle fluxes arising from the plasma and the intense nuclear power deposited, attention must be paid to the thermal-hydraulic design of its cooling system to guarantee a uniform and proper cooling for the PFUs and the CB structural material, giving a safe margin against Critical Heat Flux (CHF) without an excessively high pressure drop.

The work was focussed on the DEMO divertor 2022 design, which foresees different cooling circuits for the PFCs and the CB [27]. The CB cooling circuit is operated with cooling water at high pressure and temperature at the same operating conditions adopted for the Water-Cooled Lithium Lead BB.

An integrated fluid-structure CFD analysis campaign of the entire divertor cassette was carried out, with the twofold aim to evaluate the CB thermal performance under the revised coolant conditions and to compare the temperature distribution in the TBs by selecting different materials for their structures, namely CuCrZr alloy, SS 316 Ti, and Eurofer97.

New features were implemented in the model with respect to the previous approach adopted for such kind of studies. The whole divertor, considering both PFC and CB cooling circuits was simulated with a detailed model.

In order to obtain a realistic temperature distribution in coolant and structure domains, particular attention was given to the divertor supporting structures, which were simulated considering a dedicated material library. Additionally, as for the outboard fixation system, including the wishbone, its pins and a section of the outboard rail, a proper radiative heat transfer condition towards the VV was implemented.

The thermal-hydraulic performances of the DEMO divertor cooling circuits were assessed following a numerical approach, described in §2.2, based on the Finite Volume Method (FVM) and adopting the ANSYS-CFX 2021 R2 commercial CFD code. Moreover, all the simulations have been performed with the ENEA CRESCO HPC infrastructure.

2.2 Description of the methodology

Navier-Stokes equations are used in fluid dynamics to characterise a fluid's macroscopic behaviour. These are a set of Partial Differential Equations (PDE) that are nonlinear and are founded on the assumption that the fluid may be represented as a deformable continuum.

Five PDEs and twenty variables are considered in the system of equations: one for density, three for velocity vector, one for pressure, nine for viscous stress tensor, three for convective acceleration vector, one for internal energy, and two for temperature and thermal conductivity.

The fluids satisfy three physical laws, which are mathematically expressed in the Navier-Stokes equations:

- principle of mass conservation (continuity equation),
- second principle of dynamics (balance of momentum),
- first principle of thermodynamics (energy conservation).

The balance between the number of equations and the number of unknowns is reached with the definition of the fluid properties. A single solution of the equation can be obtained if Boundary Conditions (BCs) and initial conditions (together with the state equation in the case of a gas mixture) are given.

The Navier-Stokes equations cannot be analytically solved with the exception of some particular cases, so they must be solved using a numerical approach.

Numerical solutions can be obtained adopting a discretisation method to approximate the differential equations with algebraic ones. The field of science that studies fluid-dynamic problems with numerical analysis is called CFD.

In order to find the Navier stokes numerical solutions, an approximation method has to be chosen for the differential equation employing a system of algebraic equations for the variables at some set of discrete locations in space and time. Several methods are used for the discretisation: Finite Difference Method, FVM and Finite Element Method (FEM). In particular, the FVM adopts the integral form of conservation laws which are resolved in a finite number of Finite Volumes (FVs).

In case of DEMO divertor cassette cooling system, there is no way to use theoretical or analytical methods due to the extremely complicated flow domain. In fact, a theoretical-computational strategy based on the FVM and an appropriate CFD code were used to conduct the research study.

The thermal-hydraulic evaluation of the DEMO divertor was performed using the qualified ANSYS CFX CFD code. This CFD programme simulates the thermofluid-dynamic behaviour of fluids in a completely three-dimensional way while accounting for convective and diffusive transport processes as well as other relevant physical phenomena. Specifically, it uses an element-based FVM to numerically solve the thermofluid-dynamic equations governing the fluid flow of interest with the pertinent BCs. The thermofluid-dynamic behaviour of single-phase, single-component flows in both laminar and completely turbulent regimes may then be precisely predicted by the algorithm.

To numerically study the nominal steady-state thermal-hydraulic behaviour of the DEMO divertor cassette cooling circuits, 3D steady-state CFD analyses have been run.

To this end, a specific 3D FV model has been set up, realistically reproducing the layout of the DEMO Divertor cassette cooling circuit.

In particular, the development of the presented FV model is articulated in the following steps:

- flow domain discretization: it was carried out by importing, employing the ANSYS SpaceClaim software, the 3D geometry of the flow domain to be studied. Considering that calculation time depends on the dimensions of the calculation grid and, thus, a coarse mesh may result in unrealistic predictions, sensitivity analyses were conducted in the past to choose a mesh fine enough to give stable predictions;
- constitutive model definition: water coolant thermofluid-dynamic properties defined in the IAPWS IF97 library, which are already in the CFX database, have been used;

- loads and BCs definition: generally, the total pressure value is set at the circuit inlet portion. Moreover, an output BC is typically the mass flow rate. A suitable "wall function" algorithm and a no-slip condition were applied at the contact between the coolant and the circuit steel walls. The wall function makes it possible to simulate the effects of the fluid-wall interaction on the total pressure drop, reducing the computational burden and simplifies the simulation of intricate transport processes occurring in the thermofluid-dynamic boundary layer. Lastly, a set of nuclear loads were included to the model to replicate thermal fluxes at the exposed surfaces as well as nuclear deposited power inside fluid and solid domains;
- turbulence model definition: the k-ε model is usually adopted for general-purpose simulations, posing a good compromise for accuracy and robustness. This model uses the scalable wall-function approach that overcomes one of the most important weaknesses of the standard wall function use in that they can be applied on arbitrarily fine meshes. On the other hand, the k-ω based Shear Stress Transport (SST) model gives a more accurate description of the near-wall region, especially in the case of flow separation. It is a hybrid model that consists of a conversion of the k–ε model into a k–ω model in the near-wall region while the standard k–ε model is adopted in the fully turbulent region far from the wall. This model uses the automatic wall treatment that automatically switches from wall functions to a low-Re near-wall formulation as the mesh is refined. In a CFD simulation, choosing the turbulence model is a relevant issue that depends on the flow regime in the flow domain and the stability of its parameters, then it should be selected on a case study;
- solution method definition: this is largely influenced by the specific problem, the chosen discretization model, and the computational grid. Typically, these methods involve consecutive linearization schemes of the equations, followed by solving the subsequent linear system using iterative procedures. Once the finite volume model is established and analysis settings are properly outlined, simulations can proceed. In particular, a typical steady-state analysis under nominal conditions was performed using the ANSYS CFX code, which employs the “false transient” algorithm to expedite convergence in steady-state numerical simulations.

Lastly, once defined all the analysis settings and convergence criteria, each analysis has been launched and the pertinent thermofluid-dynamic results have been post-processed adopting the ANSYS CFD-Post.

2.3 Thermal-hydraulic analysis of DEMO divertor

The thermal-hydraulic performances of the divertor cooling circuit were assessed considering the coolant operating conditions reported in Table 2.1.

The complete simulations were carried out considering the CB coolant at an inlet pressure of 155 bar and an inlet temperature of 295°C. Three slightly different mass flow rates (around 17.0 kg/s) were adopted for the three simulations (targets in CuCrZr, SS 316 Ti and Eurofer97). These were properly tuned to obtain the required 328°C outlet temperature of the CB cooling circuit. In this regard, the temperature difference between the inlet and outlet sections of the cassette was evaluated depending on the total deposited power. In particular, both surface and volumetric loads were considered, obtaining a total deposited power of ≈3.4 MW per cassette. Slightly different values of total deposited power on the CB are obtained due to the different TB materials, whose details will be discussed thoroughly in §2.4.1.

Table 2.1. Summary of divertor cooling circuit operative conditions.

CB Inlet Pressure [MPa]	15.5
CB Inlet Temperature [°C]	295.0
CB mass flow rate [kg/s]	≈17.0
PFC Inlet Pressure [MPa]	7.5
PFC Inlet Temperature [°C]	130.0
PFC mass flow rate [kg/s]	45.0
Thermal Power per CB cassette [MW]	≈3.4
Thermal Power per PFC cassette [MW]	≈3.7-4.0
CB Coolant ΔT [°C]	≈33
PFC Coolant ΔT [°C]	≈22

Considering the PFC cooling circuit operating conditions, the ADRANOS tool, widely described in [28], was adopted. The tool was developed to assess the thermofluid-dynamic behaviour of the divertor cooling circuit lowering the computational cost. In particular, this was done by predicting the divertor performance map changing the coolant inlet conditions and mass flow rates and allowing for a low-effort study of several circuit configurations. So, it was used to preliminarily select suitable operating conditions for the 2022 PFC cooling circuit while respecting the main thermal-hydraulic and maximum temperature constraints.

The results, already presented in [29], showed that the cooling circuit cannot be operated at inlet pressure and temperatures of 50 bar and 130°C (conditions originally considered in

[14]) due to insufficient CHF margins. To keep the inlet temperature unchanged so to avoid the CuCrZr to work at unduly low temperatures, the inlet pressure requires to be increased to ≈75 bar. Under these conditions, it was possible to select a mass flow rate between 42 and 50 kg/s, choosing an intermediate value of 45 kg/s. Moreover, it is also noted that the possibility of operating the PFCs cooling circuit under the selected operating conditions was already confirmed by the preliminary 3D-CFD analysis carried out in 2022 and presented in [29].

A fully coupled 3D-CFD analysis campaign was carried out aiming at evaluating:

- the coolant total pressure distributions and overall total pressure drops for both cooling circuits;
- the pumping power required and the breakdown of power loss contributions;
- the coolant flow velocity distribution within PFUs, SL, RPs and NSs cooling channels;
- the coolant temperature distribution in the main cassette components;
- the coolant saturation margin distribution;
- the CHF margin distribution among VTs PFU cooling channels, the SL and the RPs plasma-facing cooling channels;
- the structure temperature distribution.

The assumptions, the models and the results pertaining to these thermal-hydraulic analyses are presented and critically discussed in the following.

2.4 CFD model setup

The divertor cooling circuits' thermal-hydraulic performances were assessed by performing steady-state, fully-coupled (fluid-structure) 3D-CFD analyses, according to the procedure described in §2.2 and adopting the coolant operative conditions of Table 2.1.

For all components (with the exception of the PFUs), the optimal mesh size to be adopted to obtain fairly grid-independent results was based on the results of dedicated mesh-independence studies performed in the past and reported in [29, 30]. The resultant calculation grid was of approximately 350 million FVs and more than 200 million nodes. More detail of the assembled mesh set-up for the CFD analysis are reported in Figure 2.1, while its main parameters are in Table 2.2.

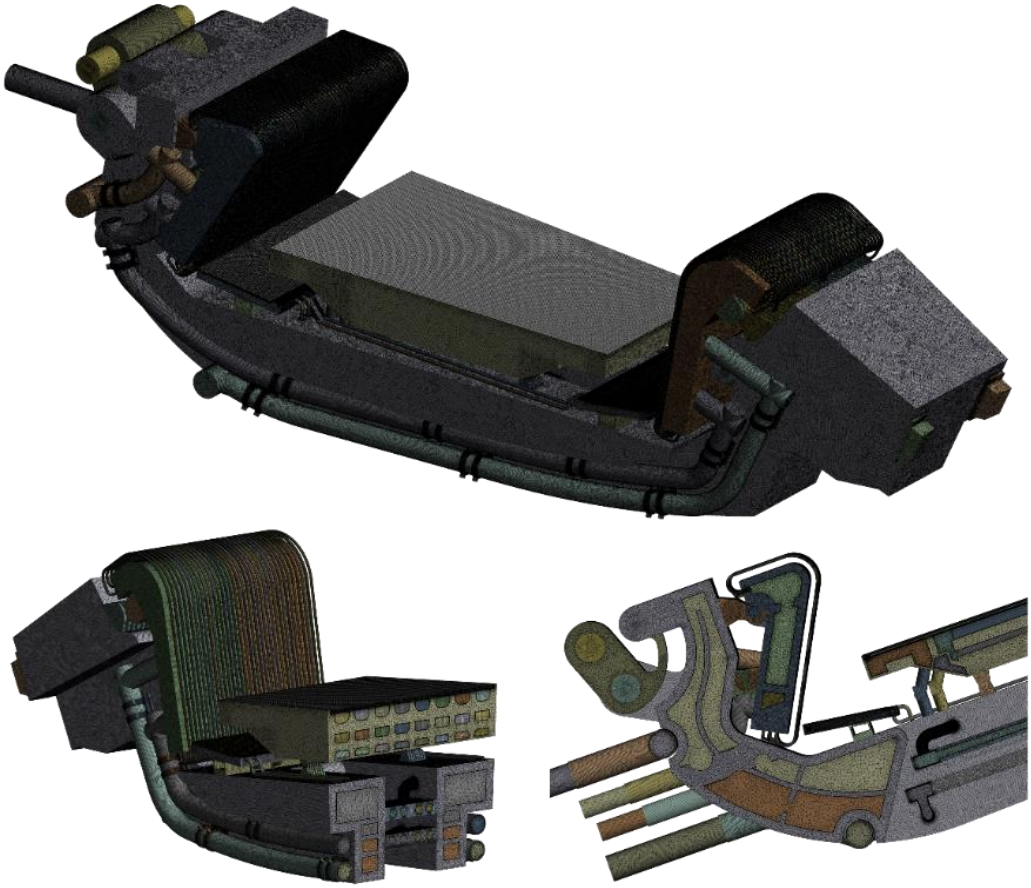

Figure 2.1 Discretization adopted for the model.

Table 2.2 Mesh parameters for coolant and structure domains.

	Coolant	**Structure**
Mesh type	Hybrid Structured/Unstructured	
Nodes	$9.06 \cdot 10^{7}$	$1.10 \cdot 10^{8}$
FVs	$1.31 \cdot 10^{8}$	$2.21 \cdot 10^{8}$
Inflation Layers Number	12	-
First Layer Thickness [μm]	20 – 50	-
Layers Growth Rate	1.2 – 1.35	-
Target Element Size [mm]	1.3 – 10	2.5 – 10

The model setup and the relevant operative conditions are summarized in Table 2.3.

Considering the applied loads, the nuclear heating maps developed in 2022 [31] by the ENEA neutronic team were adopted, which are discussed in §2.4.1. Moreover, constant values for SL and RPs First Wall (FW) heat fluxes were considered respectively amounting to 0.5 and 0.1 MW/m^2, as introduced in [29].

Table 2.3 Model setup and operative conditions.

Analysis Type	Steady-State Coupled
Nuclear Heating	Non-uniform (2022)
Wall Heat Flux – Liner	0.5 MW/m^2
Wall Heat Flux – RPs	0.1 MW/m^2
Radiative Heat Transfer	Towards VV at 40°C
Turbulence Model	k-ω SST
Boundary Layer Modelling	Automatic Wall Functions
Wall Absolute Roughness	2-15 mm
PFU treatment	OVST
Inlet BC (Temperature/Pressure) – CB	295°C/15.5 MPa
Outlet BC (Mass Flow Rate) – CB	~ 17 kg/s
Inlet BC (Temperature/Pressure) – PFC	130°C/7.5 MPa
Outlet BC (Mass Flow Rate) – PFC	45 kg/s

Due to the presence of STs, the PFU cooling channels are the most tough components from the point of view of the computational burden. Then, a simplified approach was chosen by analysing only their fluid-dynamic aspect adopting properly calibrated porous media, employing the Orthotropic Virtual Swirl Tape (OVST) approach described in [32].

Using this methodology, the prediction of the thermal behaviour of the PFUs and their supports is not addressed. By the way, by detecting the most critical region of VTs, further thermofluid-dynamic analyses can be carried out. In particular, a sub-modelling approach can be used, adopting the results of the whole cassette as BCs for a single PFU assembly simulation.

To define appropriate equivalent OVST for both IVT and OVT PFUs, the following workflow was adopted:

- at first, a detailed fluid-dynamic simulation of the coolant inside a single PFU channel was carried out for each of the two targets considering a 0.6 mm bulk size mesh so to have fairly grid-independent results. Additionally, the average nominal value of the mass flow rate, determined as the ratio between the total mass flow rate and the number of PFU assemblies, was taken into consideration within a ±20% range;

- an equivalent fluid volume without ST was defined for each PFU, using a coarser mesh with a bulk size of 1.3 mm, and adopting a porous medium in the whole channel section, originally hosting the ST;
- the OVSTs were then properly regulated to guarantee that the pressure drop at different mass flow rates Δp(G) curve was replicated with a very low relative error (lower than 3% at the lower mass flow rates), optimising their parameters using the ANSYS DesignXplorer optimization tool;
- finally, to correctly reproduce the PFUs' energy balance into account, a uniform volumetric heat source was considered for the porous media, amounting to the sum of surface and volumetric contributions.

By adopting this modelling strategy, the number of finite volumes for each PFUs channel is significantly reduced, from about $5 \cdot 10^6$ to approximately $7 \cdot 10^5$.

Moreover, the capability to reproduce the pressure drop curve as a function of the mass flow rate over an extensive array of values around the nominal one allows to have some confidence in the distribution of flow rates between the various PFUs channels when the complete simulation is performed, being the equivalent model capable of dealing with deviations from nominal values.

However, considering the high computational burden for the simulations, all the analyses have been performed with the ENEA CRESCO HPC infrastructure [33]. By adopting this resource, it was possible to reduce the calculation time for each simulation to a reasonable one (~24 hours) by running the analysis in parallel on 672 processors Intel Xeon Platinum 8160 processors @2.10 GHz, equipped with a total of 2688 GB of RAM.

The set of materials adopted for the model is reported in Table 2.4. In order to obtain more comprehensive temperature distributions, an additional level of detail was introduced in the model, compared to the previous DEMO divertor thermal-hydraulic calculations. In particular, the supports connecting VTs to the CB were simulated in Inconel 718 (Figure 2.2), as well as the wishbone pins (Figure 2.3).

Furthermore, the outboard rail section was simulated with a simplified geometry, as it was considered made of SS 316L (N) [34].

Finally, regarding the PFC circuit, CuCrZr, Eurofer97and SS 316 Ti are considered, while the materials composing the PFU monoblocks are not modelled explicitly. Due to the lack of information on SS 316 Ti thermal properties, data relevant to the SS 316L (N)-IG were selected in agreement with the WPDIV [31].

Table 2.4 Materials adopted for the model.

Fluid CB/PFC	Water IAPWS IF97 [35]
CB (with NS), Liner, RPs	Eurofer97 [36]
TBs and Pipes	CuCrZr [37] /SS 316 Ti [38]/ Eurofer97
Wishbone	Ti6Al4V [39]
Liner, RPs PF layers	Tungsten [39]
VTs supports, Wishbone pins	Inconel 718 [38]
Outboard Rail	SS 316L (N) [40]

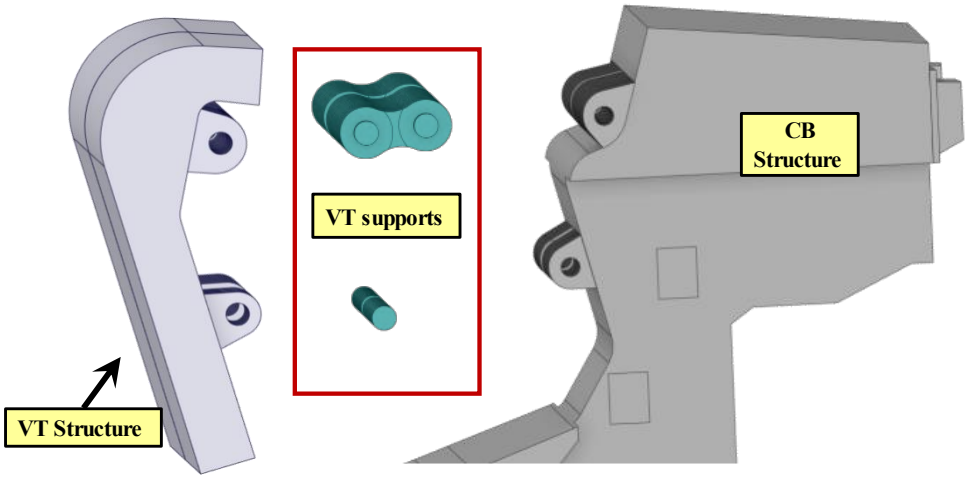

Figure 2.2 VT and VT supports modeling.

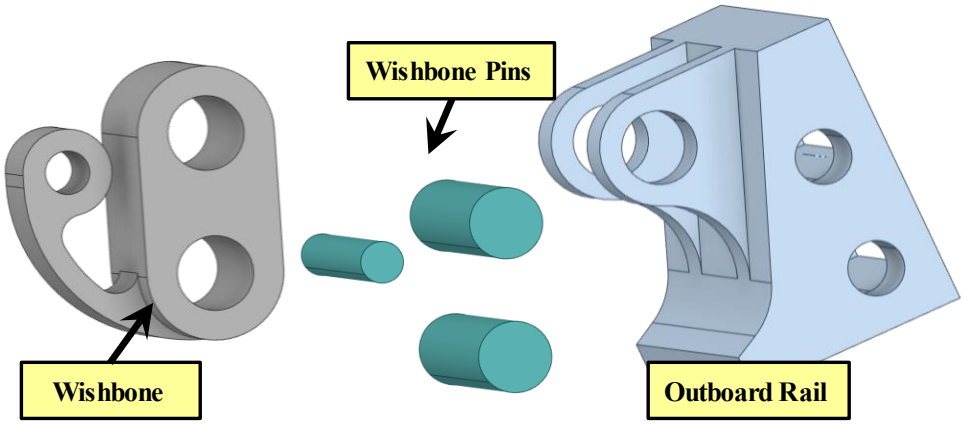

Figure 2.3 Wishbone system exploded view.

Furthermore, to correctly consider the presence of the VV that, looking at [41], is supposed to operate at 40°C, a simplified radiative heat transfer condition has been considered in the CFD model, involving particularly the surfaces of the bottom part of the CB and of the fixation system, as illustrated in Figure 2.4. More in detail, a radiative heat

flux was implemented on the relevant surfaces, given by the Stefan-Boltzmann law, expressed in case of two grey surfaces, which is reported below.

$$Q_{rad} = \sigma \varepsilon F_v (T^4 - T_{VV}^4) \quad (2.1)$$

In equation (2.1), the coefficient σ is the Stefan-Boltzmann constant equal to $5.67 \cdot 10^{-8}$ $W/(m^2K^4)$, the F_v is the view factor which was considered arbitrarily equal to 1. Moreover, the coefficient ε is the Eurofer97 emissivity, equal to 0.3, the T_{VV} is the VV temperature (40°C), whereas T is the temperature variable of the model.

Furthermore, in order to have temperature results not strongly affected by the BCs for what concerns the wishbone system, a toroidal section of the outboard rail to which the divertor is attached was considered in the model. To this additional component, the condition of radiation to VV was applied to its lower and back surfaces. The divertor and rail radiative surfaces are depicted in Figure 2.4.

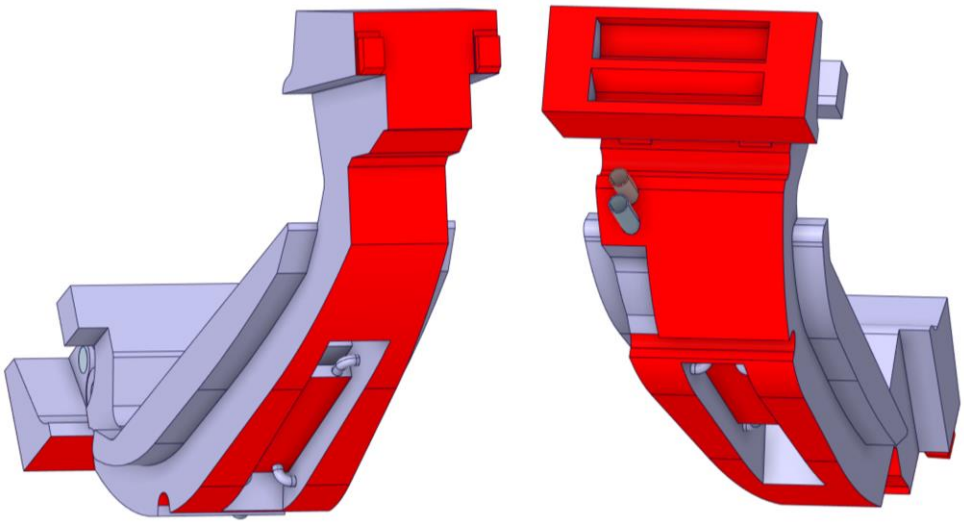

Figure 2.4 Divertor and rail radiative surfaces.

2.4.1 Nuclear heating

The non-uniform volumetric nuclear-deposited power distribution relevant to the last double-circuit divertor concept configuration [24], released by the ENEA Frascati neutronics team ([42], [43]) was adopted. The nuclear heat loads were evaluated using the Monte Carlo N-Particle (MCNP5) neutronic transport code.

The nuclear-deposited power distribution was imported onto the ANSYS CFX environment which interpolates these data over the pertaining domains.

In Figure 2.5 power density distribution for the case with TBs and PFC manifolds made of CuCrZr is shown.

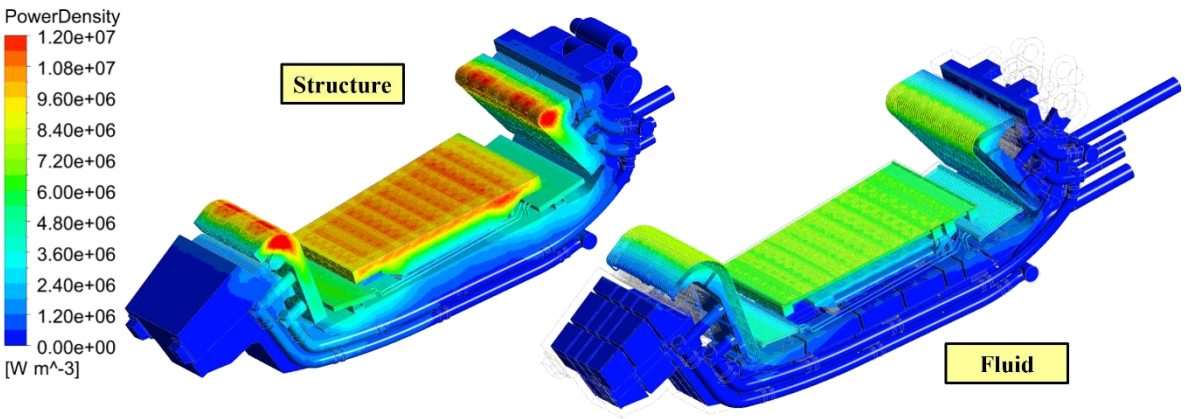

Figure 2.5 Power density distribution in fluid and structure domains.

The full breakdown of the total deposited power is reported for PFC and CB, respectively, in Table 2.5 and Table 2.6 for the case with TBs in CuCrZr, in Table 2.7 and Table 2.8 for the targets in Eurofer97, and in Table 2.9 and Table 2.10 for the targets in SS 316 Ti. Both volumetric (structures and coolant) and surface heat loads for all the pertinent CB and PFC sub-components are included.

As for the total integral values, they were reported in tables from Table 2.11 to Table 2.13 for the three cases considering different materials, for each of the two circuits and are compared to the results obtained with neutronic calculations.

Table 2.5. PFC heat loads (case with TBs in CuCrZr).

Origin	Power [MW]
OVT Surface	1.385
OVT Armour	0.279
OVT Structure	0.391
OVT Coolant	0.100
IVT Surface	1.045
IVT Armour	0.271
IVT Structure	0.422
IVT Coolant	0.090
Pipes Structure	0.015
Pipes Coolant	0.019
TOTAL	4.017

Table 2.6. CB heat loads (case with TBs in CuCrZr).

Origin	Power [MW]
SL Surface	0.771
SL Armour	0.095
SL Structure	1.099
SL Coolant	0.445
RPs Surface	0.062
RPs Armour	0.022
RPs Structure	0.115
RPs Coolant	0.026
CB Structure	0.656
CB Coolant	0.150
TOTAL	3.442

Table 2.7. PFC heat loads (case with TBs in Eurofer97).

Origin	Power [MW]
OVT Surface	1.385
OVT Armour	0.267
OVT Structure	0.255
OVT Coolant	0.091
IVT Surface	1.045
IVT Armour	0.254
IVT Structure	0.282
IVT Coolant	0.082
Pipes Structure	0.013
Pipes Coolant	0.018
TOTAL	3.702

Table 2.8. CB heat loads (case with TBs in Eurofer97).

Origin	Power [MW]
SL Surface	0.771
SL Armour	0.094
SL Structure	1.106
SL Coolant	0.450
RPs Surface	0.062
RPs Armour	0.022
RPs Structure	0.113
RPs Coolant	0.026
CB Structure	0.630
CB Coolant	0.153
TOTAL	3.429

Table 2.9. PFC heat loads (case with TBs in SS 316 Ti).

Origin	Power [MW]
OVT Surface	1.385
OVT Armour	0.267
OVT Structure	0.255
OVT Coolant	0.089
IVT Surface	1.045
IVT Armour	0.258
IVT Structure	0.270
IVT Coolant	0.080
Pipes Structure	0.011
Pipes Coolant	0.017
TOTAL	3.677

Table 2.10. CB heat loads (case with TBs in SS 316 Ti).

Origin	Power [MW]
SL Surface	0.771
SL Armour	0.094
SL Structure	1.096
SL Coolant	0.444
RPs Surface	0.062
RPs Armour	0.022
RPs Structure	0.115
RPs Coolant	0.026
CB Structure	0.634
CB Coolant	0.149
TOTAL	3.416

It can be noticed that there are some differences between the CFX and MCNP total heat load. They are probably due to the interpolation procedure required to map the loads obtained with MCPN into the CFD code. Anyway, the interpolation errors are very small, being globally lower than 5%. However, higher values may be encountered for the single components.

As it may be observed from the tables, the total power deposited onto the CB is practically unchanged for the three cases with differences below 30 kW per cassette. The differences on the heat loads of the PFC cooling circuit are more marked, with differences of ≈400 kW per cassette. This is due to the different material adopted for the VTs.

Table 2.11. Total heat loads comparison (case with TBs in CuCrZr).

Circuit	CFX [MW]	MCNP [MW]	ε [%]
PFC	4.017	4.069	1.27
CB	3.442	3.286	4.72

Table 2.12. Total heat loads comparison (case with TBs in Eurofer97).

Circuit	CFX [MW]	MCNP [MW]	ε [%]
PFC	3.702	3.696	0.16
CB	3.429	3.274	4.72

Table 2.13. Total heat loads comparison (case with TBs in SS 316 Ti).

Circuit	CFX [MW]	MCNP [MW]	ε [%]
PFC	3.677	3.719	1.12
CB	3.416	3.269	4.50

2.5 Results

The main outcomes obtained for the divertor cooling circuits thermofluid-dynamic analysis under the operative conditions of Table 2.1 are herewith discussed. In particular the most relevant results are reported in terms of:

- coolant total pressure and total pressure drop distributions;
- pumping power required and the breakdown of power losses contributions;
- mass flow rate branching between SL and RPs, coolant flow velocity distribution among SL, PFUs, NSs, and RPs cooling channels;
- coolant temperature and sub-cooling margin distributions;
- coolant bulk temperature distribution among main subcomponents' cooling channels;
- CHF margin distribution among PFUs, SL and RPs FW cooling channels,
- structure temperature distribution.

Considering that the results obtained are referred to two hydraulically separated cooling circuits, they have been reported in two sub-sections in the following, one for the PFC cooling circuit (§2.5.1) and the other one for the CB cooling circuit (§2.5.2). In each subsection, the results for the pertaining circuit are reported for all the three cases with different material. Moreover, a third section was introduced §2.5.3 where some considerations about the whole divertor thermal field are reported.

Regarding the CHF margin, it is worth giving first a definition of this parameter since it has a fundamental importance in design of a cooling circuit and in the definition of the coolant conditions. The CHF margin is given by the ratio between the incident CHF, whose definition is given in [44], and the actual wall heat flux on the plasma-facing walls. Naturally, the higher is such a ratio the lower is the risk to reach the instability. Its value in plasma-facing channels for DEMO divertor is prescribed to be higher than 1.4, in compliance with the requirements foreseen for the ITER divertor [44].

2.5.1 PFC cooling circuit results

The coolant total pressure distribution and the total pressure drops between the main sections of the divertor PFC cooling circuit (Figure 1.22) are shown in Figure 2.6 and summarized in Table 2.14 for the CuCrZr case, respectively.

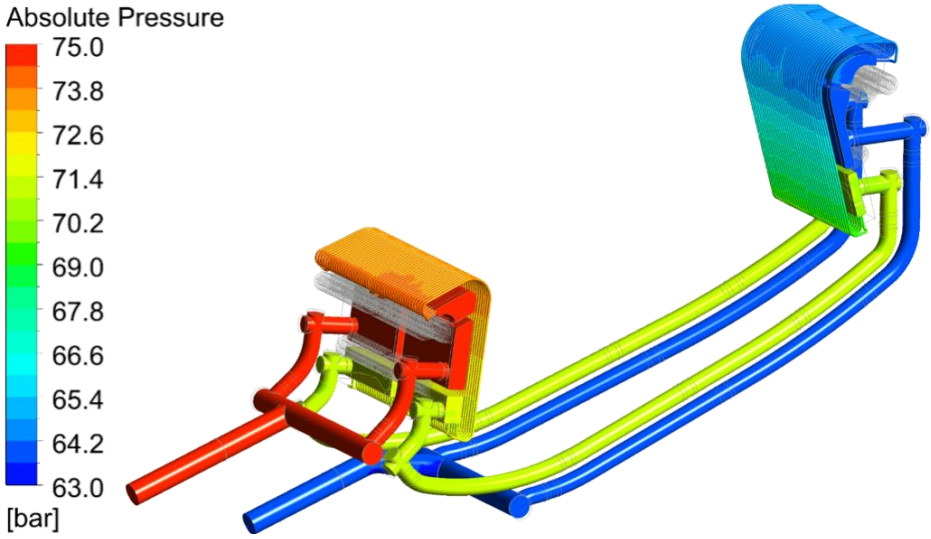

Figure 2.6 Pressure field distribution in PFC cooling circuit.

Table 2.14. Total pressure drop distribution.

Pressure point	**Component**	**Δp_{tot} [MPa]**
Inlet → OVT Inlet	**Inlet Pipes**	0.0308
OVT Inlet → OVT Outlet	**OVT**	0.3362
OVT Outlet → IVT Inlet	**VT Pipes**	0.0481
IVT Inlet → IVT Outlet	**IVT**	0.6703
IVT Outlet → Outlet	**Outlet Pipes**	0.0424
Inlet → Outlet	**TOTAL**	**1.1278**

From the results, it can be argued that the divertor PFC cooling circuit's overall total pressure drop is equal to 1.13 MPa, being lower than the recommended limit of 1.4 MPa [14]. The components with the highest pressure loss are the IVT and OVT, due to the presence of STs. Furthermore, pumping power has been estimated for each component, depending on the product between the mass flow rate and the pressure drop of each section. The results are reported in Table 2.15, while their percentage contribution is shown in Figure 2.7.

Table 2.15 Divertor PFC cooling circuit pumping power breakdown.

Component	P [kW]
Inlet PFC	1.477
OVT	16.208
VTs Pipes	2.332
IVT	32.653
Outlet PFC	2.076
TOTAL	**54.64**

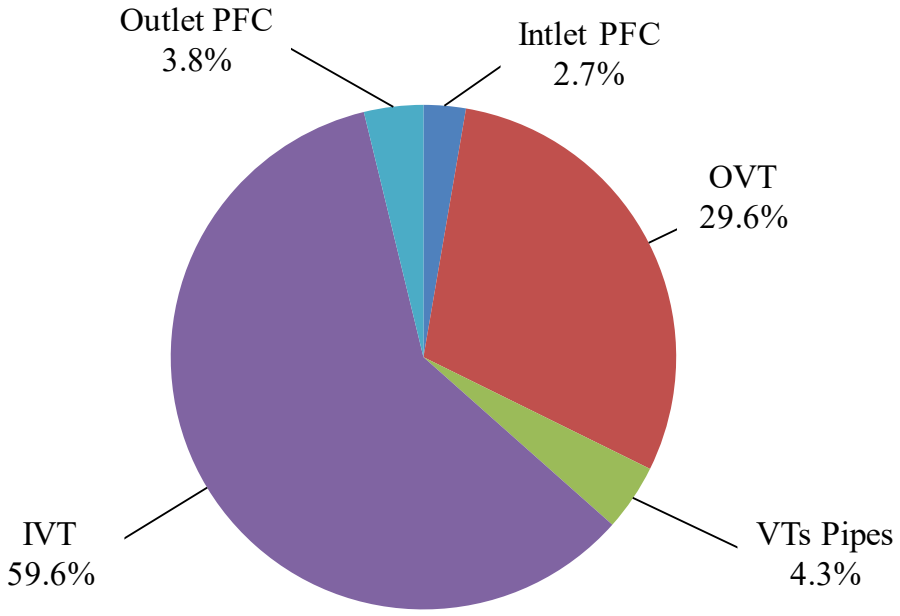

Figure 2.7 PFC cooling channels nomenclature.

For the sake of simplicity, the results reported here in terms of pressures and velocity distributions are only relevant to the option with TBs in CuCrZr, which was considered as the reference case. Negligible deviations are encountered with respect to the other two cases with TBs in Eurofer97 and SS 316 Ti.

The results obtained for the PFC cooling circuit analysis in terms of coolant axial flow velocity distribution among VTs channels (whose nomenclature is in Figure 2.8) are reported in Figure 2.9, while the distribution key parameters are reported in Table 2.16.

From the analysis of the results, it is possible to argue that within the cooling channels of each VTs the distribution of coolant axial flow velocity is acceptably uniform.

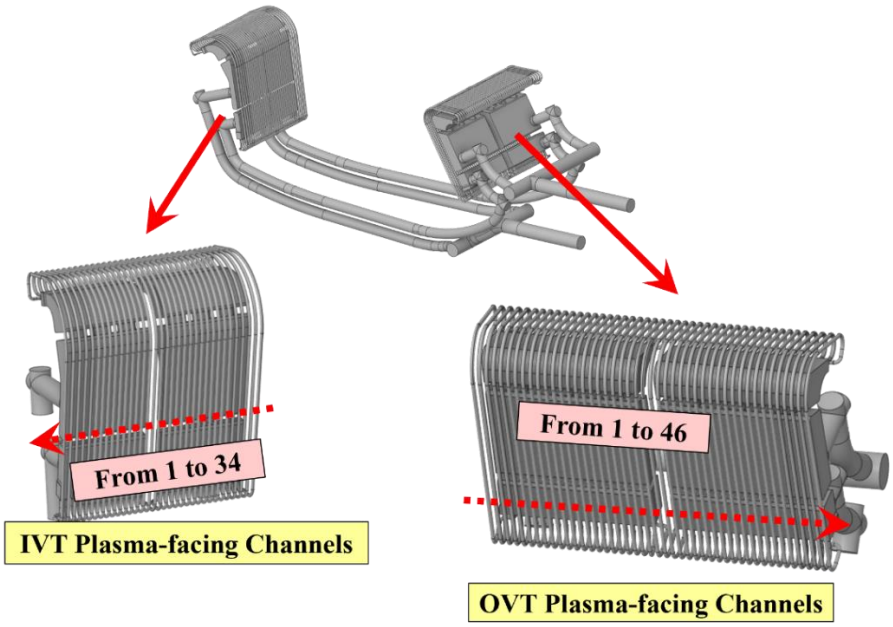

Figure 2.8 PFC cooling channels nomenclature.

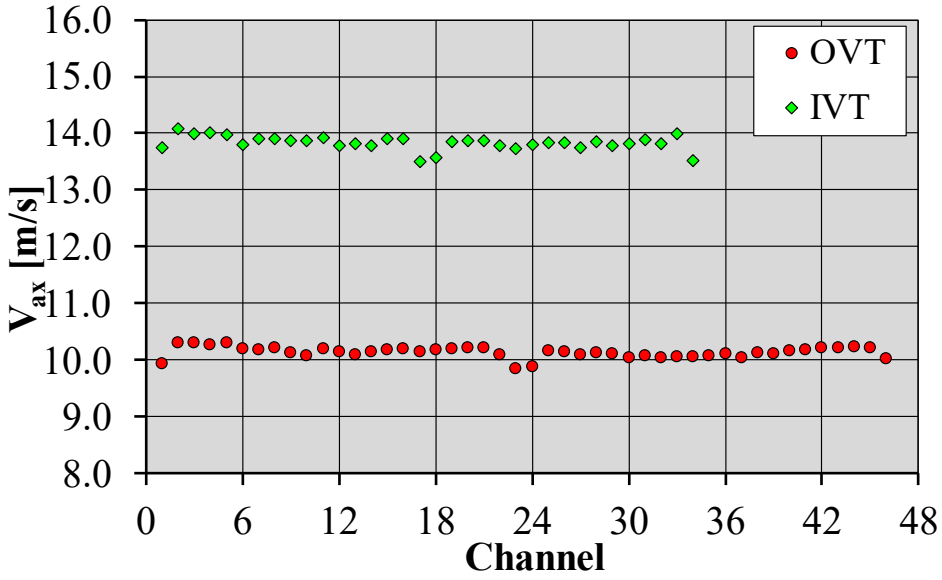

Figure 2.9 Coolant axial velocity distributions among PFC cooling channels.

Some statistical parameters are reported in Table 2.16 to better decipher the results. In particular, σ is the standard deviation, and ε is the relative span, which is defined, for a generic quantity F, as follows:

$$\varepsilon_F = \frac{F_{Max} - F_{min}}{< F >} \tag{2.2}$$

Moreover another statistical parameter was considered, i.e. the Coefficient of Variation (CV), which is given by the ratio between the standard deviation and the average value of the considered data set F and it is reported in the equation (2.3).

$$CV_F = \frac{\sigma_F}{< F >} \tag{2.3}$$

The CV gives an indication of the data dispersion compared to their mean value.

Looking at Table 2.16 maximum deviations around 4% were estimated between the maximum (V_{Max}) and minimum (V_{min}) values calculated for both the two VTs. The CV was calculated for the two axial flow velocity distributions and it is lower than 1% for both VTs, resulting to be quite low.

Moreover, it is worth noticing that the average velocity within IVT PFU channels is remarkably higher (≈13.8 m/s) than for the OVT ones (≈10.1 m/s). This difference is clarified since the same mass flow rate (45 kg/s) is directed inside 34 PFU channels for IVT and 46 channels for OVT as the two VTs are in series, with a consequent higher average velocity in the IVT.

Table 2.16 Coolant axial velocity distribution among the PFU channels main parameters.

	OVT	**IVT**
V_{Max} [m/s]	10.311	14.085
V_{min} [m/s]	9.846	13.505
ε_V	4.51%	4.12%
<V> [m/s]	10.137	13.831
σ [m/s]	0.099	0.125
CV	0.98%	0.91%

In order to check whether these balanced coolant flow distributions might have beneficial effects on the PFC circuit cooling capabilities, coolant temperature distribution and coolant margin against saturation were considered. The coolant temperature field is reported for the three examined cases in figures from Figure 2.10 to Figure 2.12. The maximum values for each sub-circuit are summarized in Table 2.17.

The coolant margin against saturation, given by the difference between the saturation temperature $T_{sat}(p)$ and the local coolant temperature, with $T_{sat}(p)$ derived from [45], is presented instead in Figure 2.13 to Figure 2.15, respectively for the three examined cases. The minimum values for each sub-circuit are summarized in Table 2.18.

Considering the temperature distributions, the highest value is located in the corners of the TB structures, where fluid stagnation is expected. However, it is possible to observe how local temperatures are everywhere lower than the saturation temperature. Indeed, no areas with a negative margin against saturation are predicted, being the lowest value equal to ≈45°C, due to the high coolant operating pressure and the low coolant inlet temperature.

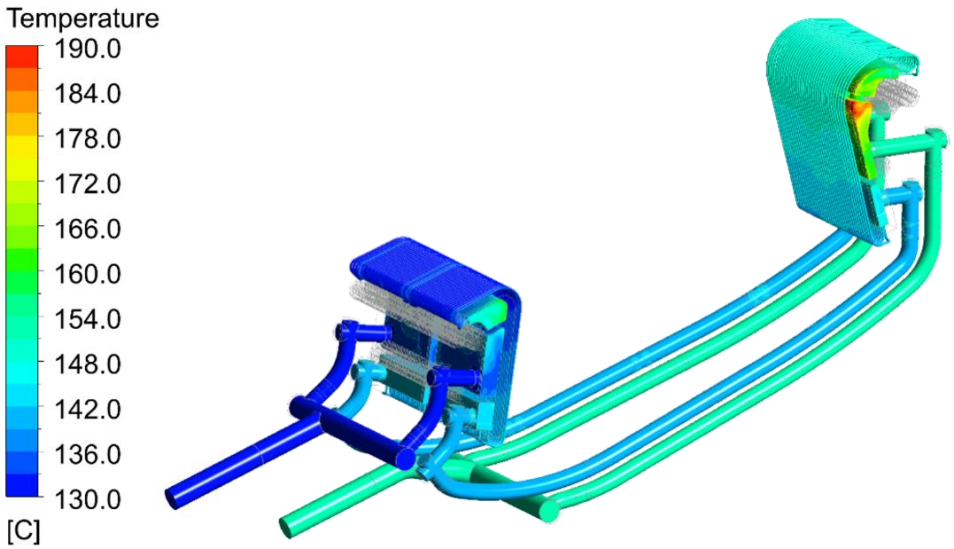

Figure 2.10. Divertor PFC coolant temperature field for case with TBs in CuCrZr.

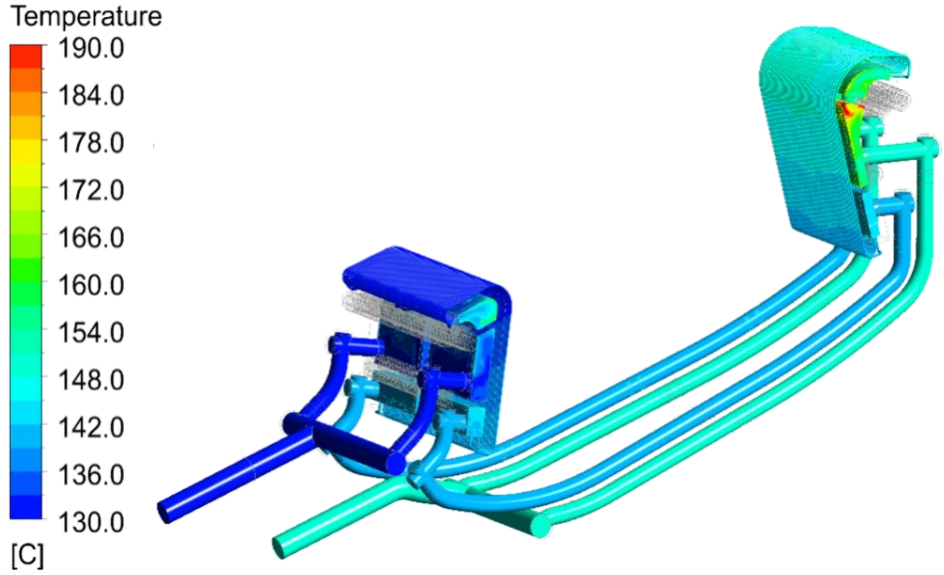

Figure 2.11. Divertor PFC coolant temperature field for the case with TBs in SS 316 Ti.

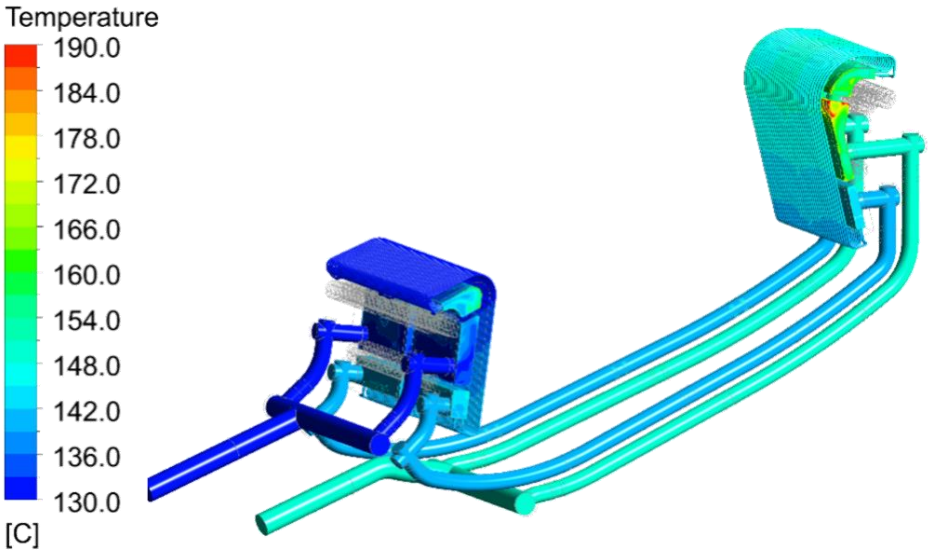

Figure 2.12. Divertor PFC coolant temperature field for the case with TBs in Eurofer97.

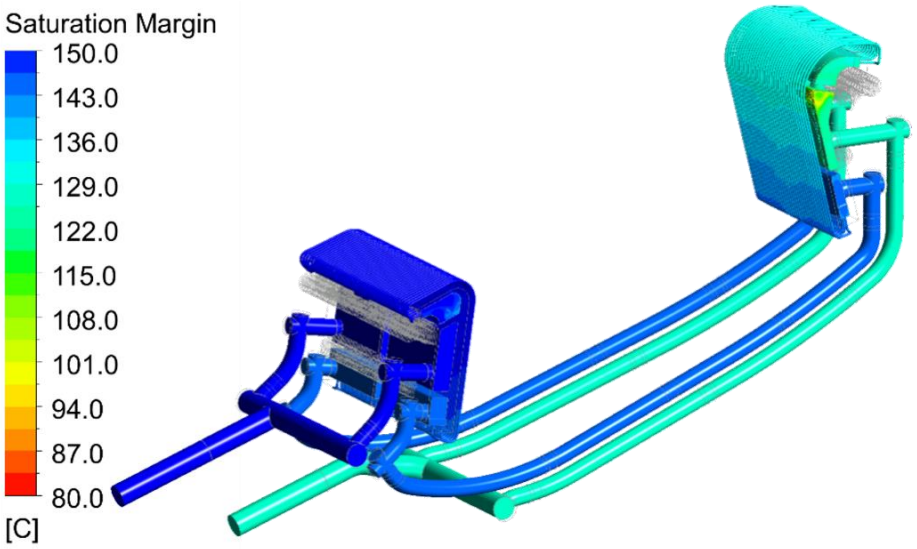

Figure 2.13. PFC coolant margin against saturation field for the case with TBs in CuCrZr.

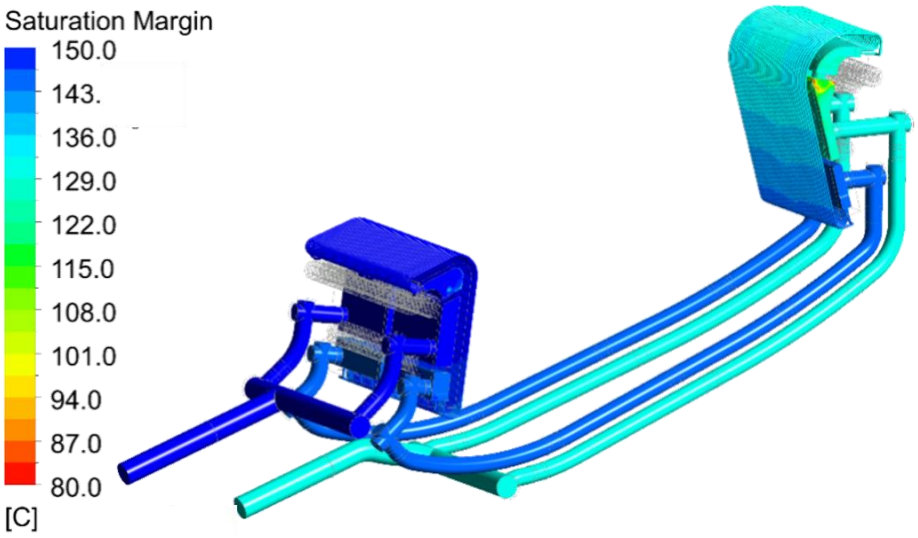

Figure 2.14. PFC coolant margin against saturation field for the case with TBs in SS 316 Ti.

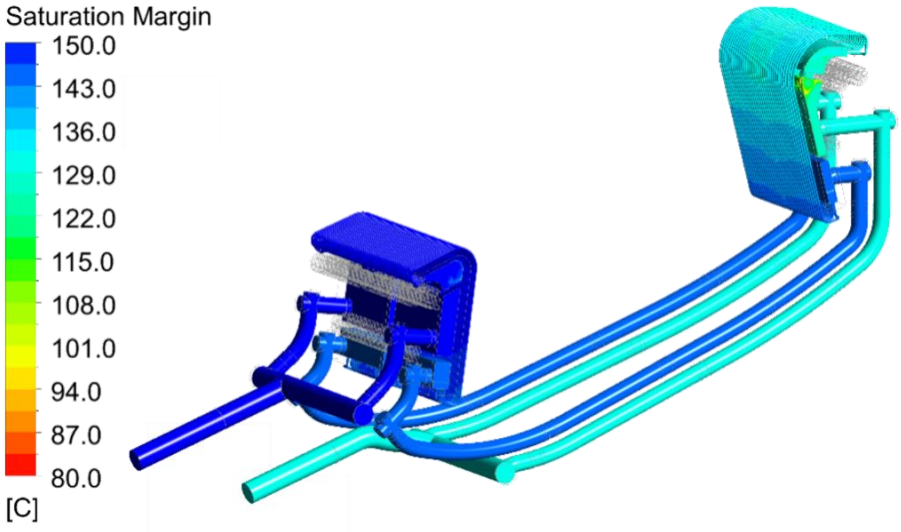

Figure 2.15. PFC coolant margin against saturation field for the case with TBs in Eurofer97.

Table 2.17. Divertor PFC cooling circuit maximum bulk temperatures [°C].

	CuCrZr	**SS 316 Ti**	**Eurofer97**
OVT	166.12	209.73	168.63
IVT	189.87	234.37	192.03
Pipes (VTs)	153.34	150.96	150.69

Table 2.18. Divertor PFC cooling circuit minimum saturation margins [°C].

	CuCrZr	**SS 316 Ti**	**Eurofer97**
OVT	124.08	80.47	121.56
IVT	90.21	45.61	88.03
Pipes (VTs)	126.53	128.91	129.10

The distributions of the margin against CHF onset within PFUs channels were assessed to check whether its prescribed minimum value of 1.4 [44] is ensured by the current cooling circuit configuration. The modified Tong-75 correlation [44, 46] already employed in the the analyses of divertor components is adopted, considering a nominal maximum heat flux of 20 MW/m^2.

The CHF margins within the PFC channels are shown in Figure 2.16 and their relevant statistical parameters are summarized in Table 2.19.

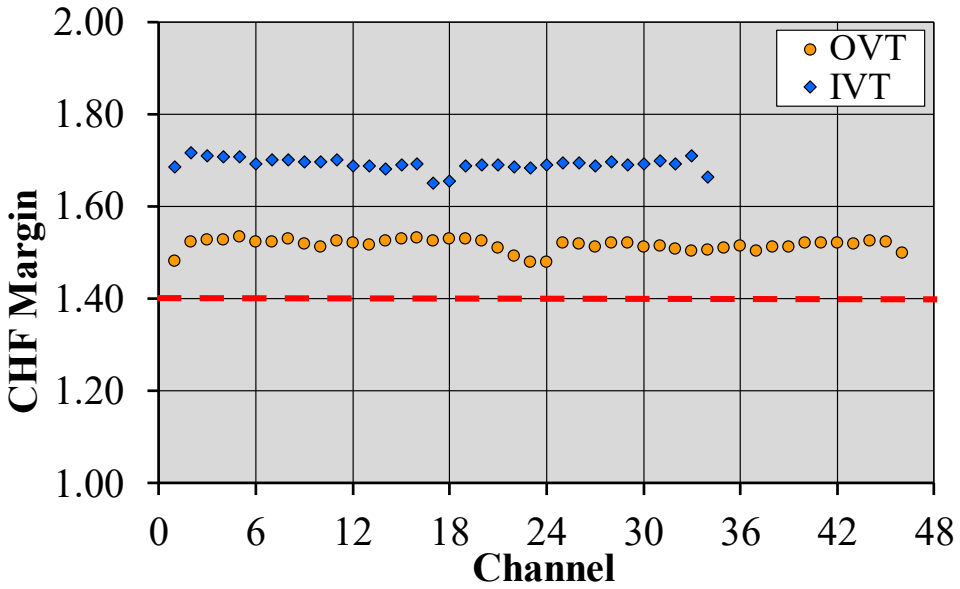

Figure 2.16 CHF margin distributions among PFC cooling channels.

Results clearly show CHF margins above the threshold value of 1.4 [44], indicated by the red dotted line. In particular, the minimum CHF margins are equal to 1.48 and 1.69, respectively for the OVT and the IVT.

Moreover, from the analysis of the results obtained, it can be noticed that the distributions of CHF margin are reasonably uniform for both the VTs. The deviations between their maximum and minimum values amount to less than 4%. Analogous results in terms of CHF margins were achieved for the cases with TBs in Eurofer97 and SS 316 Ti.

Table 2.19 CHF margin distribution main parameters.

	OVT	**IVT**
$(\text{CHF Margin})_{Max}$	1.533	1.717
$(\text{CHF Margin})_{min}$	1.478	1.651
ε_{CHF}	3.57%	3.84%
<CHF Margin>	1.516	1.691
σ	0.013	0.014
CV	0.87%	0.81%

Finally, the structure temperature field is reported for the three cases in figures from Figure 2.17 to Figure 2.19. As it can be drawn from the results, temperatures in PFC structures reach extremely high values on the TBs and on their supports, especially for the case with TBs in SS 316 Ti and Eurofer97. This happens on a very large area of the inboard supports between TBs and CB, where extremely high temperatures are predicted, as visible in Figure 2.18 and in Figure 2.19. This is due to the relevant volumetric heat loads at which the supports are exposed, together with the lack of a support active cooling system.

Please note that different scales are adopted for the different figures. In particular, for Eurofer97 and CuCrZr the maximum value was set to the maximum temperature of their respective optimal operational range, being 550°C for Eurofer97 [10]. In case of CuCrZr and SS316Ti no specific limits are considered, and the maximum values were arbitrarily set to 300°C and 600°C, respectively. The minimum temperature instead was set to 130°C which is the minimum fluid temperature inside the PFC cooling circuit.

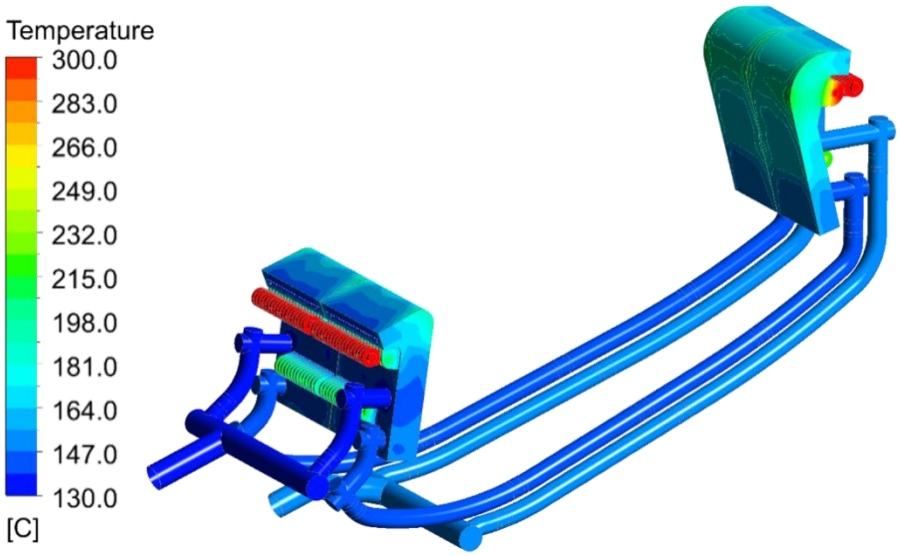

Figure 2.17 Structure temperature distribution with target bodies in CuCrZr.

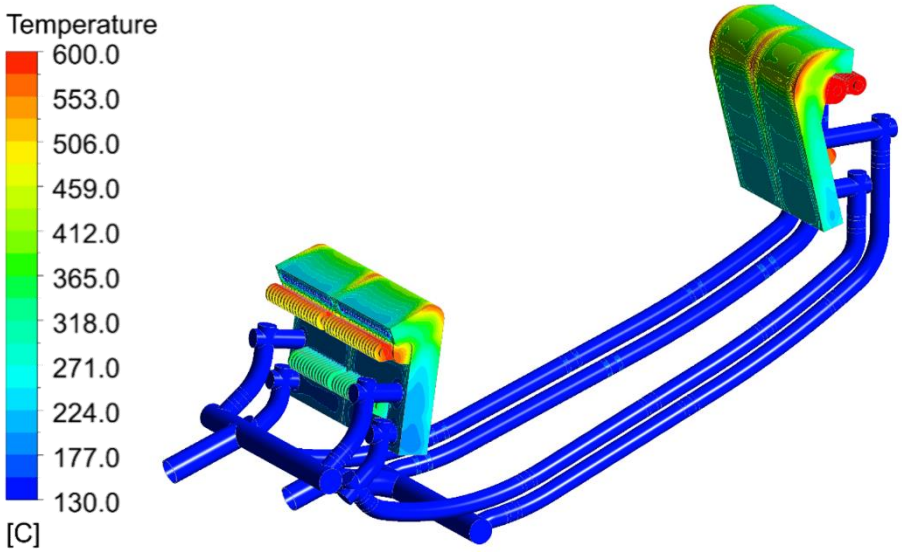

Figure 2.18 Structure temperature distribution with target bodies in SS316Ti.

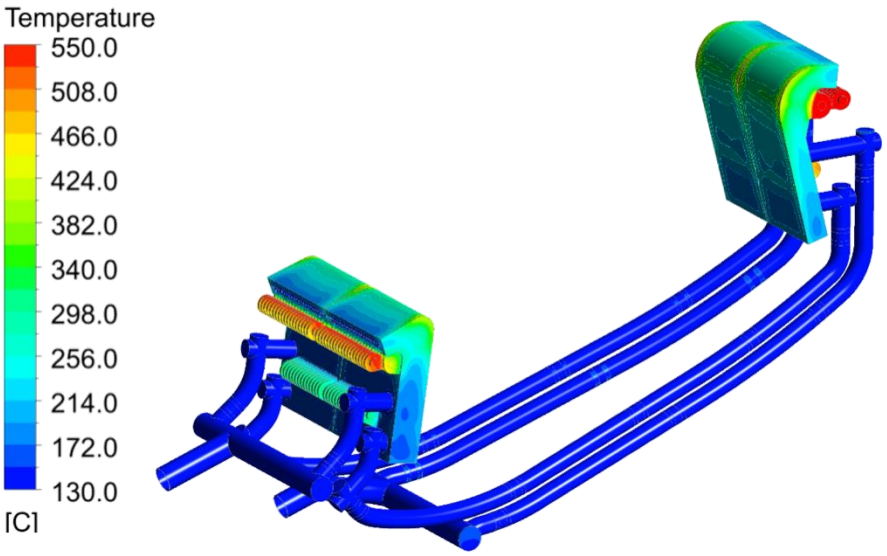

Figure 2.19 Structure temperature distribution with target bodies in Eurofer97.

An outline of the maximum structure temperature is provided in Table 2.20. As it can be drawn from the table, temperatures from 850 to 970°C are predicted of the inboard supports between TBs and CB. Moreover, it can be noted that the worst situation occurs in case of TBs in SS316Ti due to its low thermal conductivity (in the order of 17 W/mK at 200°C) compared to the other two materials. Slightly lower temperatures are noted in the case of TBs in Eurofer97, which has a thermal conductivity around 30 W/mK. The lowest temperatures are instead those relevant to the case with TBs in CuCrZr, in compliance with its highest conductivity around 350 W/mK at 200°C.

However, even in the best case with TBs in CuCrZr, temperatures outside the acceptable operational range are predicted, especially for both IVT and OVT supports and for the IVT structure.

Table 2.20. Maximum PFC structure temperatures in the main components [°C].

	CuCrZr	**SS 316 Ti**	**Eurofer97**
OVT	219.32	580.51	479.00
IVT	329.90	975.56	840.56
Pipes (VTs)	155.80	187.69	170.92
OVT supports (Inconel)	480.88	599.23	549.35
IVT supports (Inconel)	704.09	972.16	845.56

A comprehensive redesign of the IVT and its supports is essential. Simply shortening the upper supports to reduce the distance to the heat sinks is likely insufficient; it is also necessary to increase the thickness of the IVT TB to enhance its neutron shielding capability.

2.5.2 CB cooling circuit results

The coolant total pressure distribution and the total pressure drops between the main sections of the divertor CB cooling circuit (whose nomenclature is given in Figure 1.14) are reported in Figure 2.20 and summarized in Table 2.21, respectively. In addition, the calculated mass flow rate branching between SL and RPs cooling circuit is reported in Table 2.22.

As it may be observed, most of the coolant mass flow rate goes to the SL (≈80 %). This is due to the significantly higher hydraulic resistance of the RPs cooling circuit compared to that of the SL, primarily because of the manifold connecting the ORP to the IRP. Since the

SL and RPs cooling circuits are fed in parallel, the coolant mass flow rate to each circuit is influenced by the hydraulic resistance of the other one.

As done for the PFC cooling circuit, the results relevant to the CuCrZr TBs case are shown in detail in the following. No remarkable differences are encountered for the other two cases, at least concerning pressure and mass flow rate distributions. The maximum deviation with respect to the other two cases in terms of total pressure drop for the CB cooling circuit is lower than 3%.

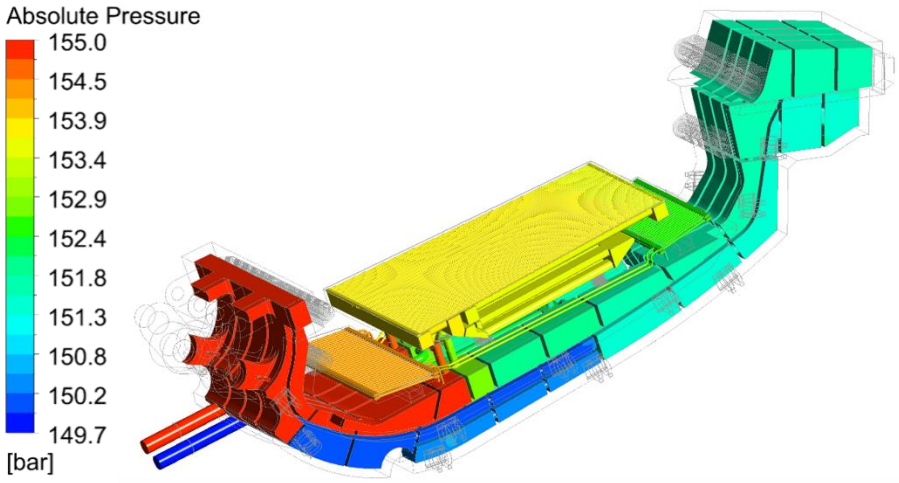

Figure 2.20 Divertor CB pressure drop distribution.

Table 2.21 Total pressure drop distribution.

Pressure point	**Component**	**Δp_{tot} [MPa]**
Inlet → ORP Inlet/Liner Inlet	**Inlet CB**	0.0341
ORP Inlet → ORP Outlet	**ORP**	0.0588
ORP Outlet → IRP Inlet	**RP Manifolds**	0.1265
IRP Inlet → IRP Outlet	**IRP**	0.0786
Liner Inlet → Liner Outlet	**Liner**	0.1893
Liner Outlet → NS Up Inlet	**CB1**	0.0256
NS Up Inlet → NS Up Outlet	**NS Up**	0.0518
NS Up Outlet/IRP Outlet → NS Low Inlet	**CB2**	0.0831
NS Low Inlet → NS Low Outlet	**NS Low**	0.0519
NS Up Outlet → Outlet	**Outlet CB**	0.0703
Inlet → Outlet	**TOTAL**	**0.5033**

Table 2.22 Mass flow rate distribution.

Section	G [kg/s]	G/G_{Tot} [%]
Liner Branch	14.53	82.9
RPs Branch	3.00	17.1
Total	17.53	-

Furthermore, pumping power has been estimated for each component, depending on the product between the mass flow rate and the pressure drop of each section. The results are reported in Table 2.23, while their percentage contribution is shown in Figure 2.21.

Table 2.23. Divertor CB cooling circuit pumping power breakdown.

Component	P [kW]
Inlet CB	0.816
ORP	0.245
RP Manifolds	0.532
IRP	0.342
Liner	3.931
CB1	0.558
NS Up	1.133
CB2	1.824
NS Low	1.381
Outlet CB	1.886
TOTAL	12.68

The results of pumping power breakdown are strongly related to the total pressure loss inside each component. Nevertheless, differently from this last parameter, it makes it easier to relate the losses to each component, even in the case of circuits in parallel. As it may be argued from the results, the most critical component in terms of energy dissipation is the SL, responsible for more than 30% of the total losses. The overall pumping power amounts to almost 13 kW per cassette.

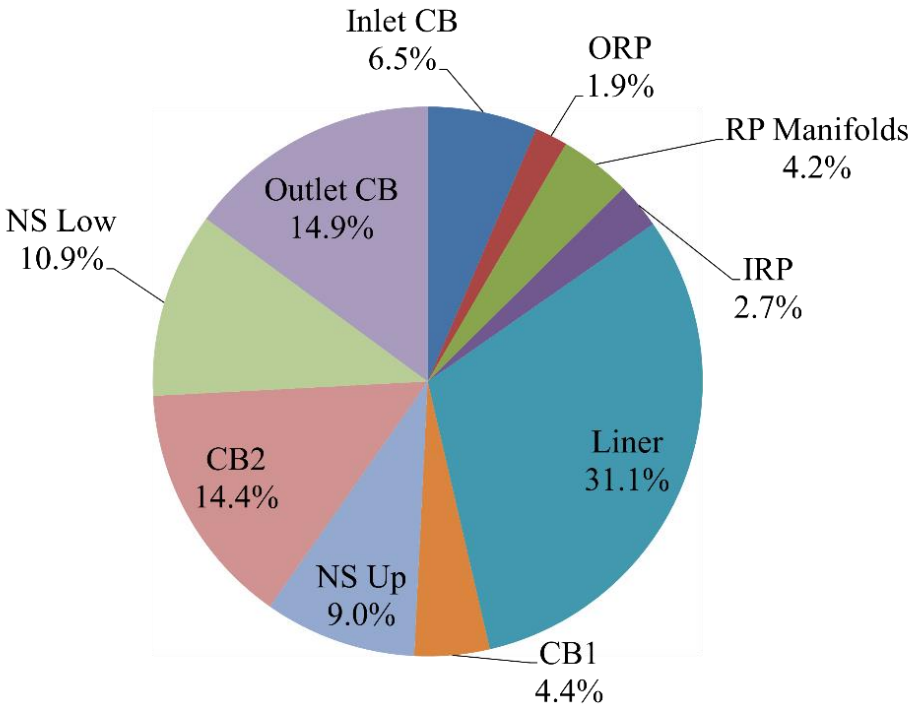

Figure 2.21. Pie chart of divertor CB cooling circuit pumping power.

The results obtained for the CB cooling circuit in terms of axial flow velocity distribution within SL FW and back channels (whose adopted nomenclature is represented in Figure 2.22) are reported in the following Figure 2.23 and Figure 2.24, while the main parameters are reported in Table 2.24 and Table 2.25.

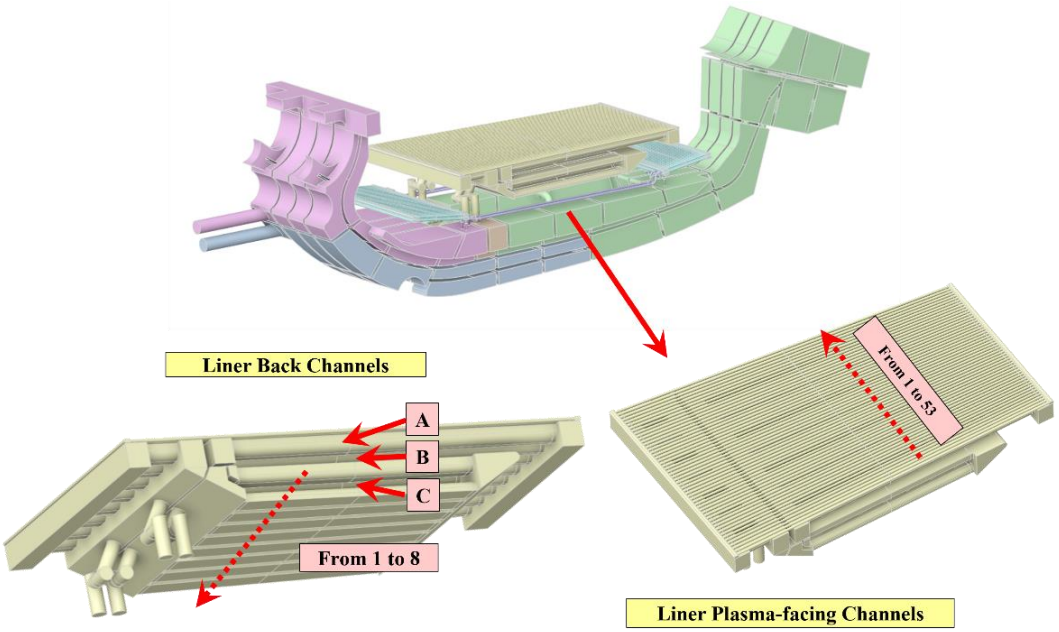

Figure 2.22. SL cooling channels nomenclature.

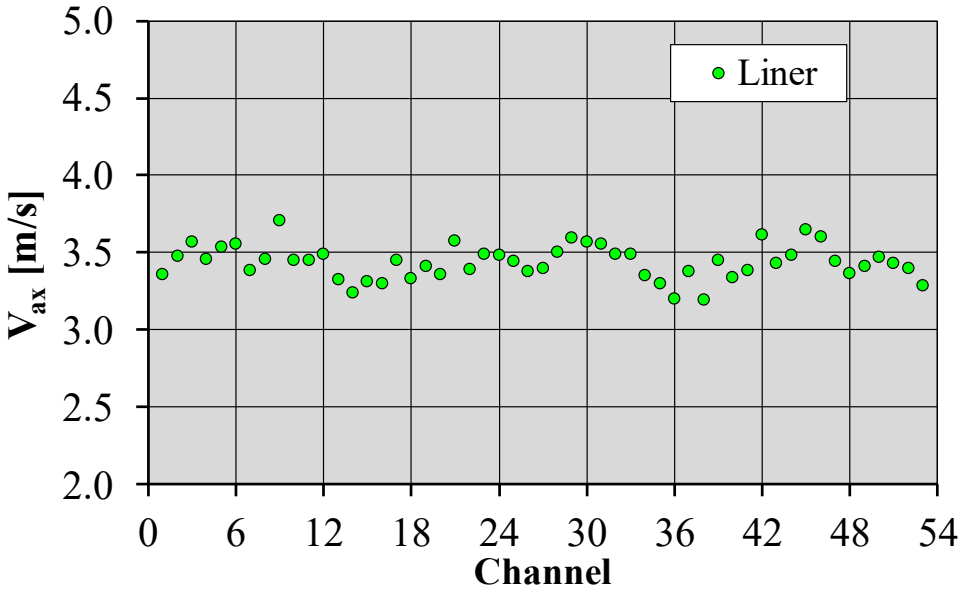

Figure 2.23. Coolant axial velocity distribution among SL FW channels.

Table 2.24. Coolant axial velocity distribution among SL FW channels' main parameters.

V_{Max} [m/s]	3.704
V_{min} [m/s]	3.192
ε_V	13.84%
<V> [m/s]	3.436
σ [m/s]	0.110
CV	3.19%

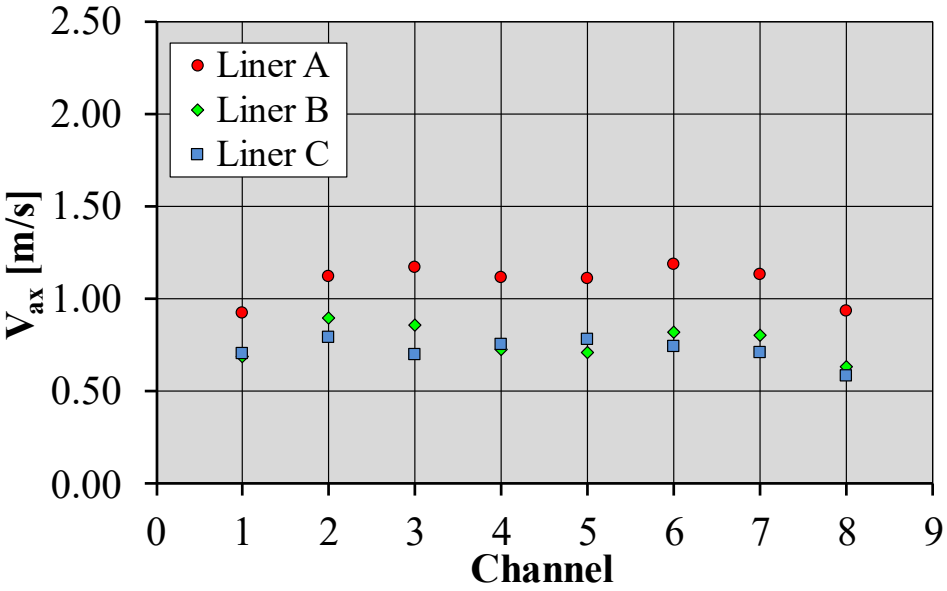

Figure 2.24. Coolant axial velocity distribution among SL back channels.

Table 2.25. Coolant axial velocity distribution among SL back channels' main parameters.

	Level A	**Level B**	**Level C**
V_{Max} [m/s]	1.186	0.894	0.793
V_{min} [m/s]	0.921	0.633	0.584
ε_V	22.38%	29.25%	26.32%
<V> [m/s]	1.087	0.766	0.720
σ [m/s]	0.102	0.090	0.065
CV	9.41%	11.81%	9.06%

From the analysis of the results, it may be noticed that flow velocity distribution among SL FW channels is acceptably uniform with deviations between maximum and minimum values lower than 14%. On the other hand, SL back-channels experience ununiform coolant velocity distributions. In particular, the predicted deviations between maximum and minimum velocities within level B and level C of the SL back-channels amount to 29.25 % and 26.32%, respectively, while the one predicted for the level A channels is 22.38%.

Regarding the coolant axial flow velocity among RPs FW and back channels (whose adopted nomenclature is represented in Figure 2.25 and Figure 2.26, respectively), the results obtained are reported in Figure 2.27 and Figure 2.28 and summarized in Table 2.26 and Table 2.27.

Looking at the flow velocity distributions among RPs channels, they are unacceptably uneven. Their deviations between maximum and minimum values are over 100%. This is a threat in terms of CHF issues as will be detailed in the following, which poses the need for a deep design revision.

A value of deviation higher than 100% is observed. In this specific case it is an indication of backflow occurrence inside some of the channels. In particular, it can be deduced from the presence of negative flow velocities (looking at the V_{min}). This recirculation condition is highly risky for CHF issues and bulk boiling of the fluid.

It can be moreover noticed how the flow distribution becomes more even in the back channels, with deviations around 35%. That occurs mainly because the flow is at first routed inside the FW channels and then, as a second passage, to the back channels. A possible design revision may be the reverting of the RPs cooling scheme, so the coolant would be first routed to the back channels and then to the FW channels, to ease coolant mixing before being directed to the RP plasma-facing channels.

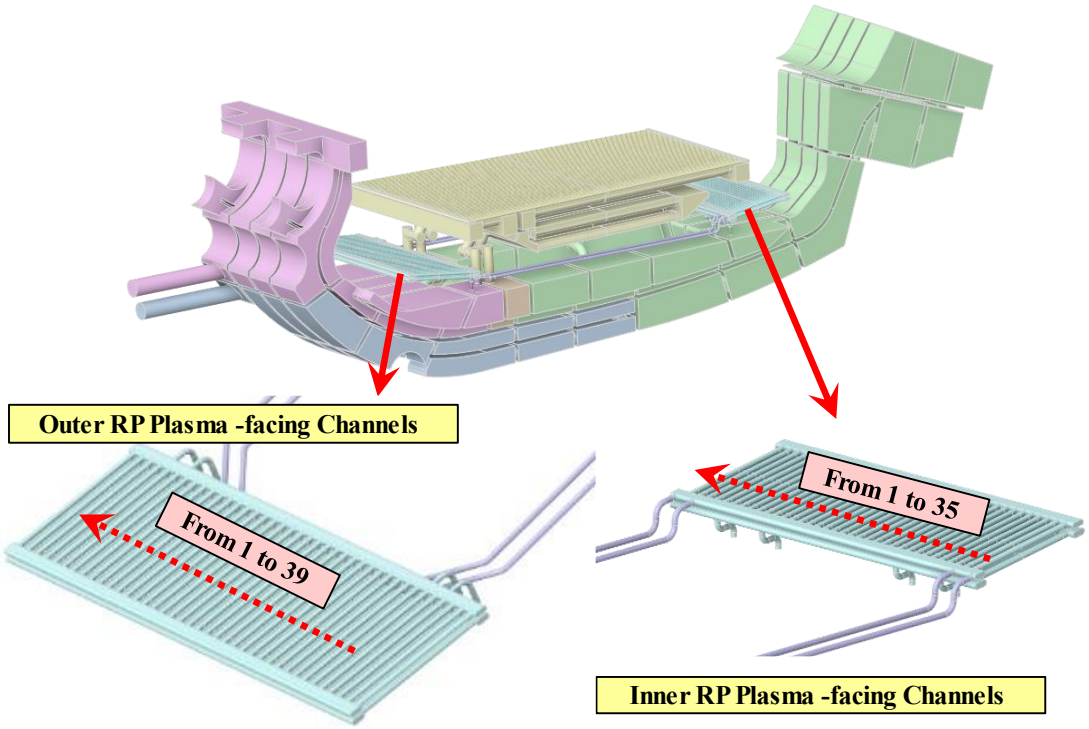

Figure 2.25. RPs FW channels nomenclature.

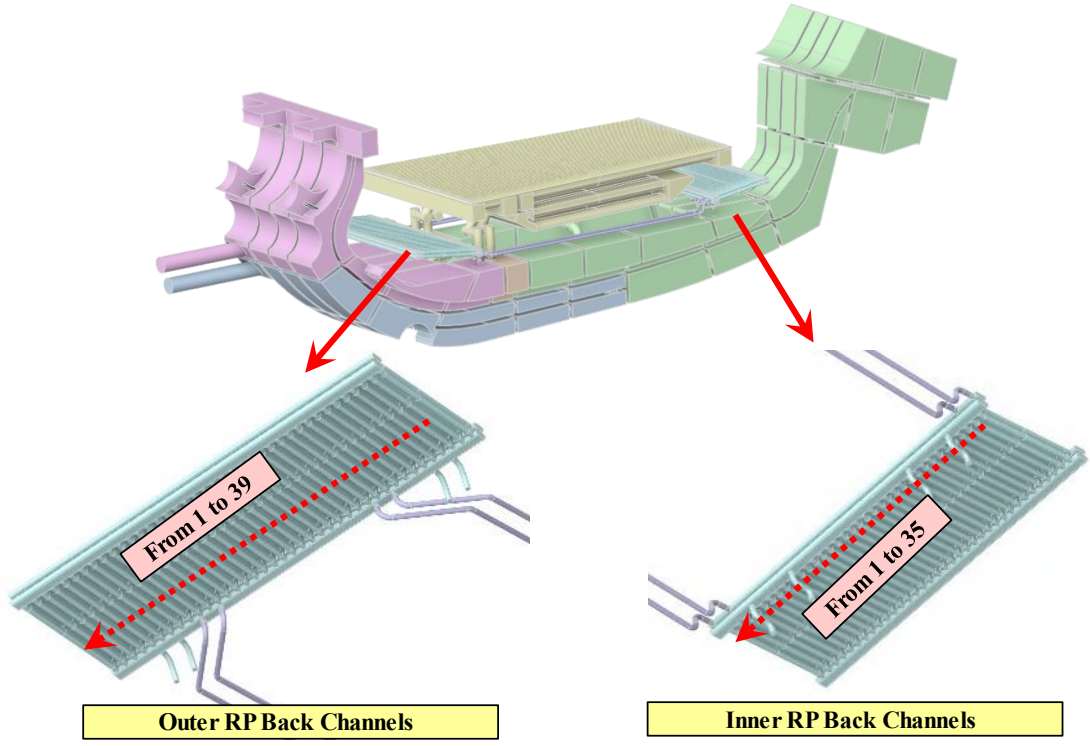

Figure 2.26. RPs back-channels nomenclature.

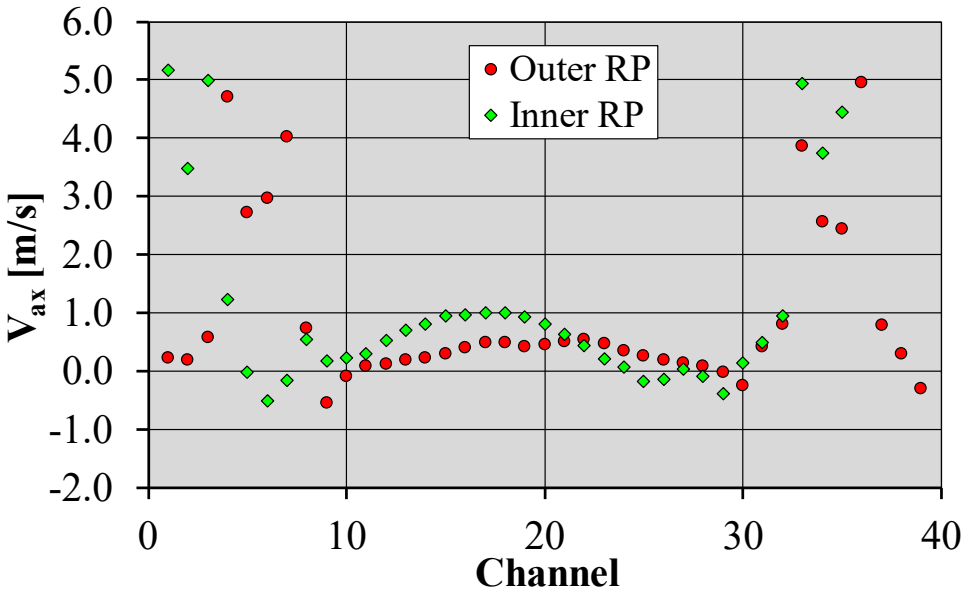

Figure 2.27. Coolant axial velocity distribution among RPs FW channels.

Table 2.26. Coolant axial velocity distribution among RPs FW channels main parameters.

	Outer RP	**Inner RP**
V_{Max} [m/s]	4.949	5.168
V_{min} [m/s]	-0.542	-0.522
ε_V	110.95%	110.11%
<V> [m/s]	0.943	1.094
σ [m/s]	1.425	1.636
CV	151.05%	149.50%

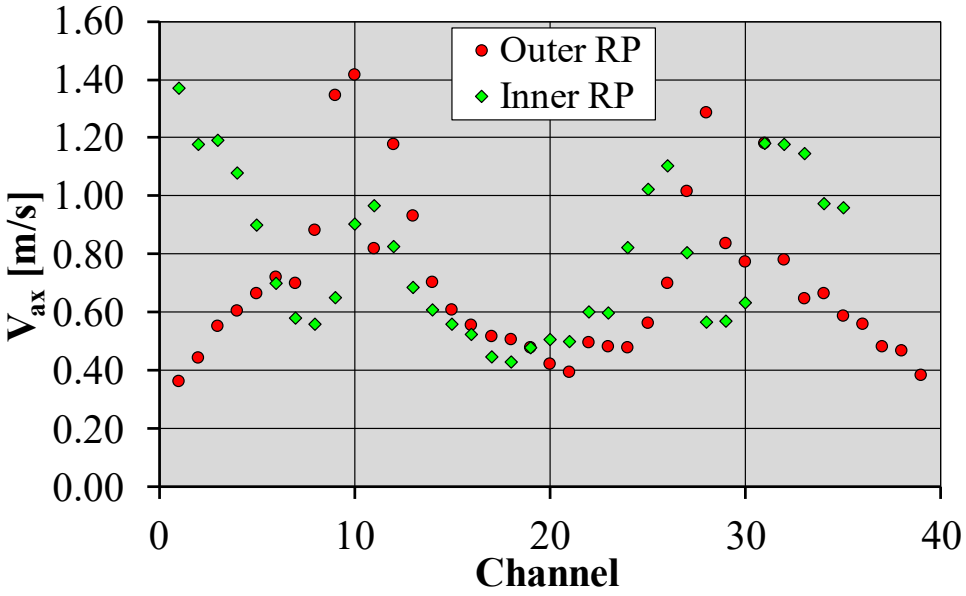

Figure 2.28. Coolant axial velocity distribution among RPs back channels.

Table 2.27. Coolant axial velocity distribution among RPs back channels main parameters.

	Outer RP	**Inner RP**
V_{Max} [m/s]	1.414	1.371
V_{min} [m/s]	0.364	0.429
ε_V	74.23%	68.72%
<V> [m/s]	0.697	0.795
σ [m/s]	0.276	0.267
CV	39.55%	33.65%

At last, regarding coolant distribution within the lower and upper NSs channels, the results obtained are reported in Figure 2.30, while the main parameters are reported in Table 2.28. The NS nomenclature is defined in Figure 2.29, where the left picture is shown from the top and it represents the upper NS cooling circuit and the right one from the bottom, representing the lower NS cooling circuit.

From the analysis of the results obtained, it is evident that flow velocity distributions among NSs channels are acceptably uniform with acceptable values of deviations between minimum and maximum values. Moreover, due to the low thermal loads expected for these components, the coolant distribution is not a critical issue, as will be detailed in the following.

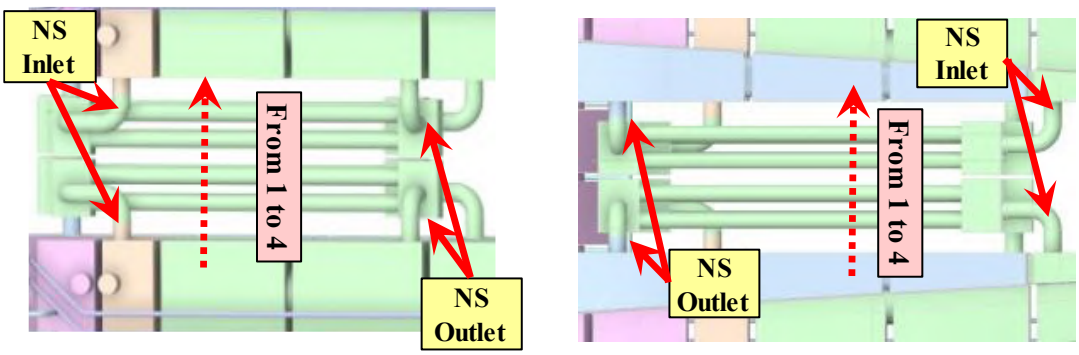

Figure 2.29. Lower NS channels (right) and upper NS channels (left) nomenclature.

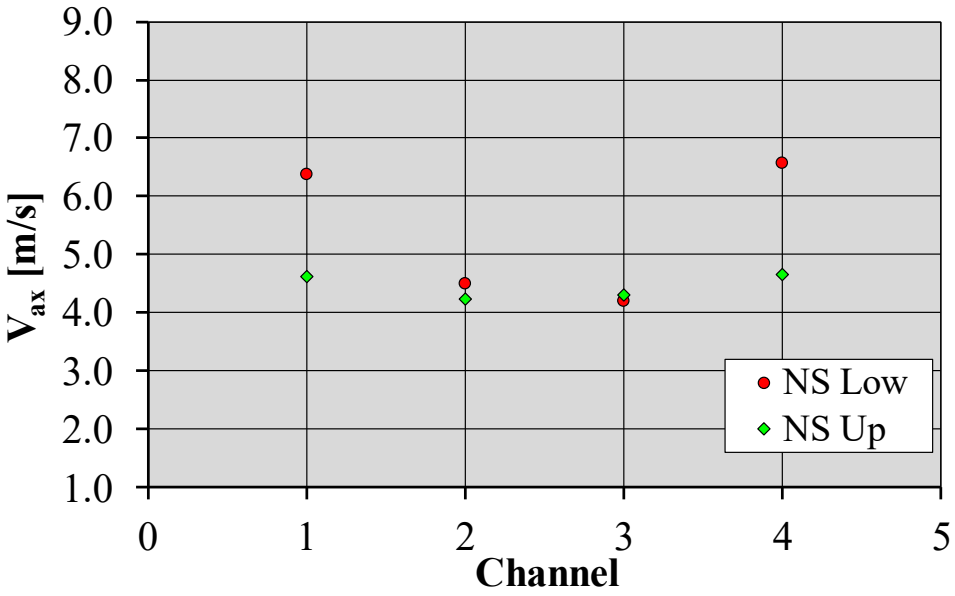

Figure 2.30. Coolant axial velocity distribution among NS channels.

Table 2.28. Coolant axial velocity distribution among NS channels' main parameters.

	Low	**Up**
V_{Max} [m/s]	6.568	4.654
V_{min} [m/s]	4.194	4.239
ε_V	36.15%	8.91%
<V> [m/s]	5.407	4.455
σ [m/s]	1.238	0.211
CV	22.90%	4.73%

The previously observed unbalanced coolant flow distributions in some sub-components might lead to uneven coolant temperature distribution. This could cause excessive thermal stresses in the steel structural components, potentially threatening their integrity. To determine if these issues might arise, the focus was set on analysing the coolant temperature distribution, especially in areas where local coolant vaporization could occur, thus compromising the coolant's heat transfer capabilities.

Therefore, the coolant temperature distributions for the three cases are depicted in figures from Figure 2.31 to Figure 2.33, while the coolant margin against saturation is shown in figures from Figure 2.34 to Figure 2.36.

Moreover, maximum bulk temperatures and minimum margins against saturation in the most relevant subcomponents of the CB cooling circuit are reported in Table 2.29 and Table 2.30.

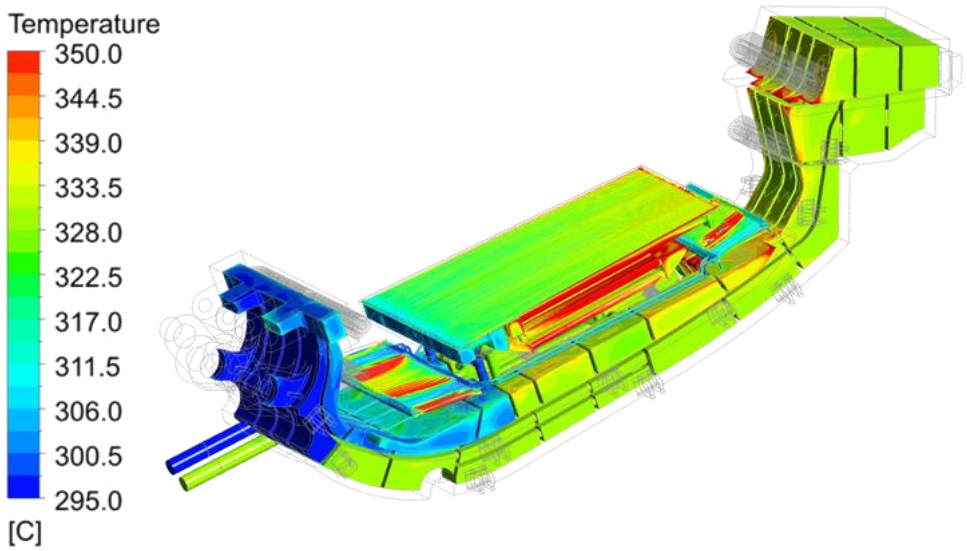

Figure 2.31. Divertor CB coolant temperature field for the case with TBs in CuCrZr.

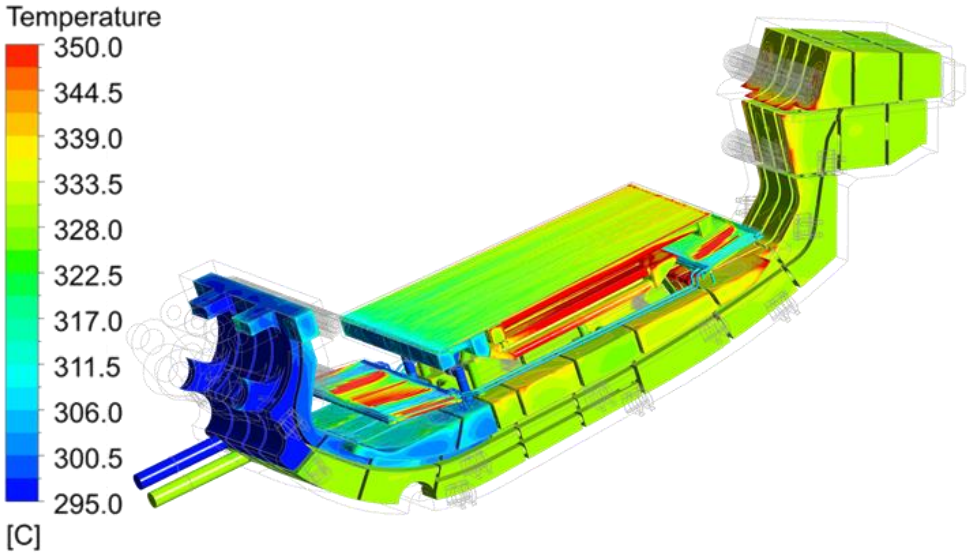

Figure 2.32. Divertor CB coolant temperature field for the case with TBs in SS 316 Ti.

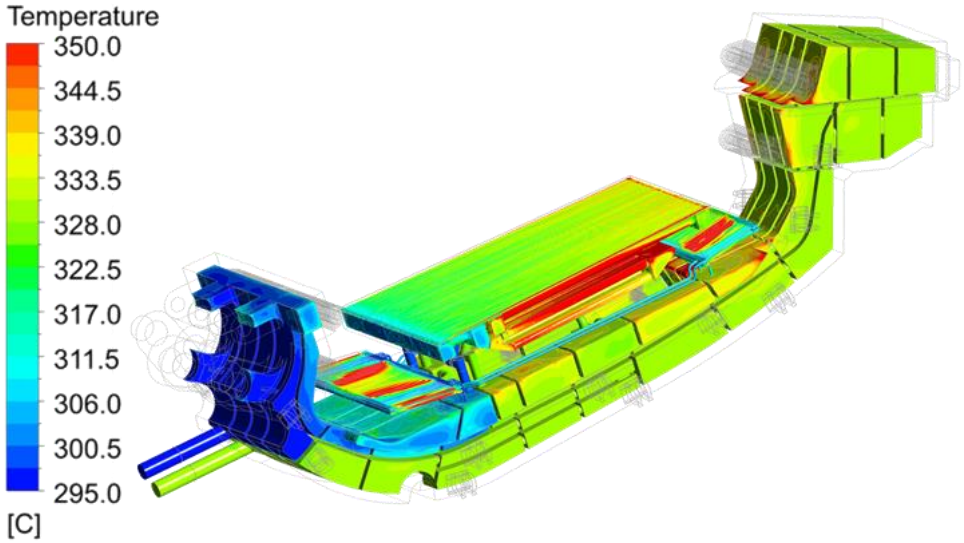

Figure 2.33. Divertor CB coolant temperature field for the case with TBs in Eurofer97.

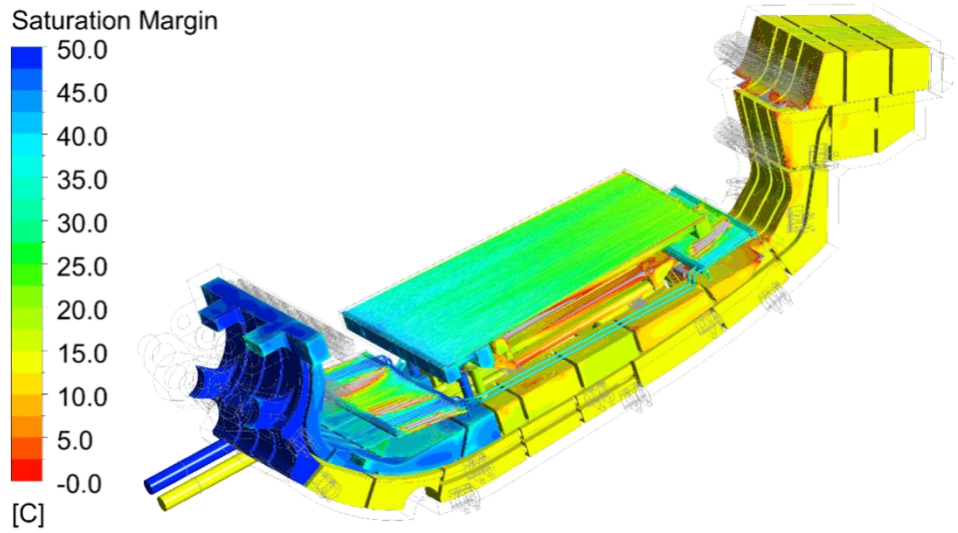

Figure 2.34. Divertor CB coolant margin against saturation field for the case with TBs in CuCrZr.

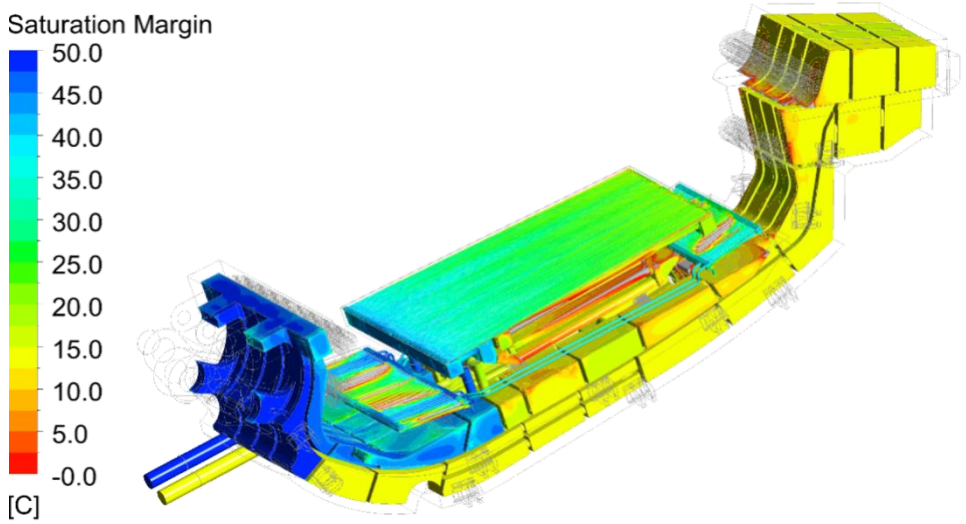

Figure 2.35. Divertor CB coolant margin against saturation field for the case with TBs in SS 316 Ti.

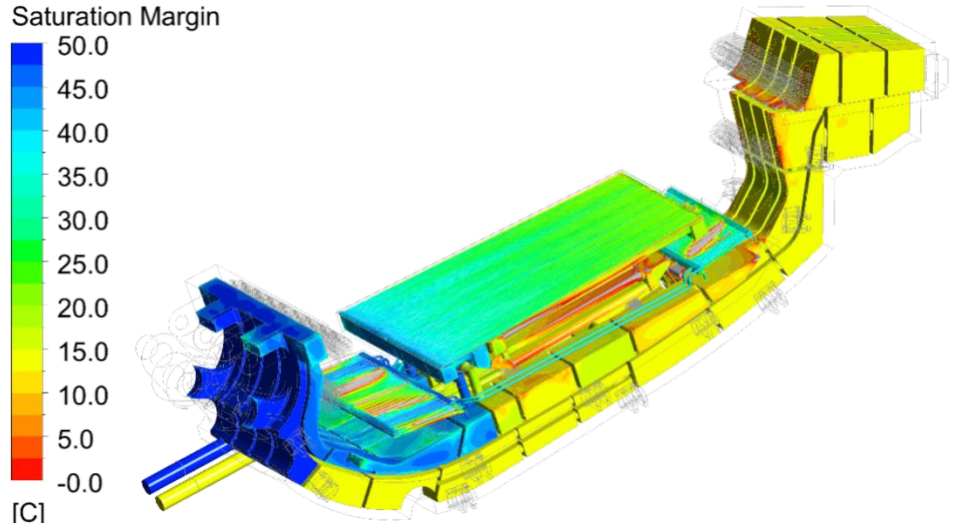

Figure 2.36. Divertor CB coolant margin against saturation field for the case with TBs in Eurofer97.

Regarding the last figures, many areas with a negative margin against saturation are predicted, far away from the desired minimum value of 20°C. These areas are particularly located in the RPs FW channels where velocity approaches zero (as visible in Figure 2.27 and Figure 2.28).

It should be moreover pointed out that the suggested 20°C saturation margin [14] limit is not applicable to a high temperature and pressure divertor cassette cooling circuit, as even supposing zero pressure drop inside the system, the outlet saturation margin cannot be higher than 17°C due to the water properties.

In RPs, the negative saturation margin is related to poor coolant distribution inside the RP channel system and should be avoided by a revision of the cooling circuit. Regarding the SL external C back channels, instead, the problem arises because of the distance of the structure from the outermost channels, which makes the structure reaching high temperatures that the coolant is not able to cool down. Additional negative saturation areas are observed in corner regions of the cassette and could be avoided by changing the shape of the CB.

Table 2.29. Divertor CB cooling circuit maximum coolant temperature [°C].

	CuCrZr	**SS 316 Ti**	**Eurofer97**
CB	354.36	354.39	354.35
Liner	166.12	209.73	168.63
RPs	189.87	234.37	192.03
Manifold	354.83	354.85	354.81

Table 2.30. Divertor CB cooling circuit minimum saturation margins [°C].

	CuCrZr	**SS 316 Ti**	**Eurofer97**
CB	-11.32	-11.28	-11.33
Liner	-10.79	-10.76	-10.81
RPs	-11.11	-11.09	-11.13
Manifold	26.31	27.96	27.91

The bulk temperature distributions within SL and RPs FW and back channels are shown in figures from Figure 2.37 to Figure 2.40 and their key parameters are in tables from Table 2.31 to Table 2.32 for the case with TBs in CuCrZr. Similar results are obtained for the other two cases.

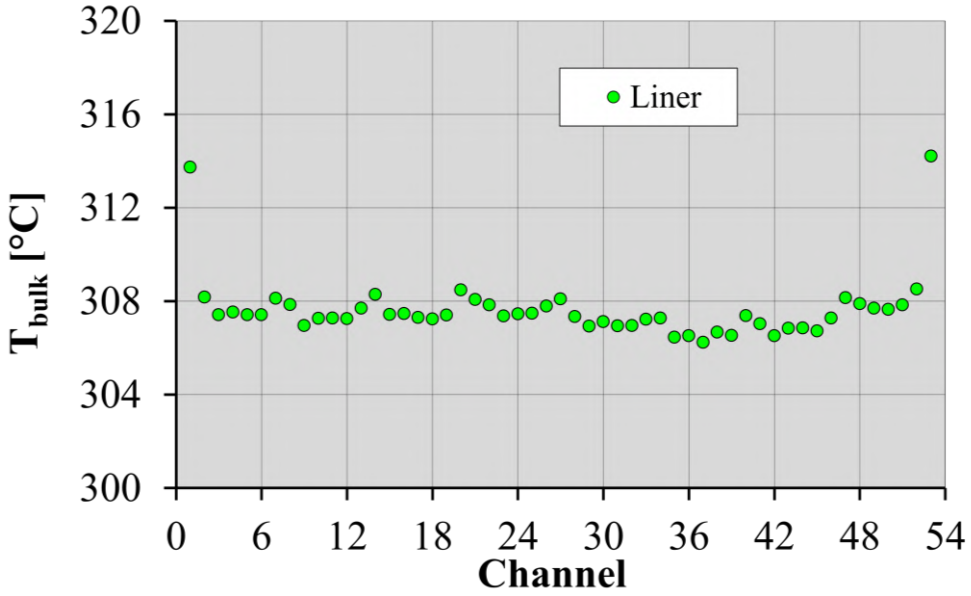

Figure 2.37. Bulk temperature distribution among SL FW channels.

Table 2.31. Bulk temperature distributions among SL FW channels' main parameters.

T_{Max} [°C]	314.20
T_{min} [°C]	306.23
ε_T	2.54%
<T> [°C]	307.63
σ [°C]	1.372
CV	0.45%

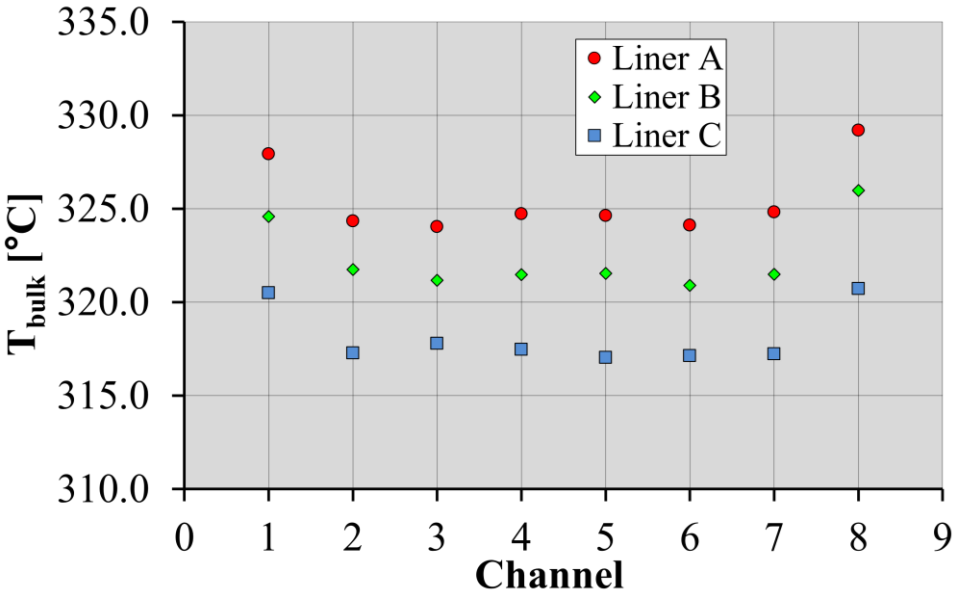

Figure 2.38. Bulk temperature distribution among SL back channels.

Table 2.32. Bulk temperature distributions among SL back channels' main parameters.

	A	**B**	**C**
T_{Max} [°C]	329.20	325.97	320.73
T_{min} [°C]	324.04	320.90	317.03
ε_T	1.57%	1.56%	1.15%
<T> [°C]	325.48	322.36	318.14
σ [°C]	1.957	1.853	1.539
CV	0.60%	0.57%	0.48%

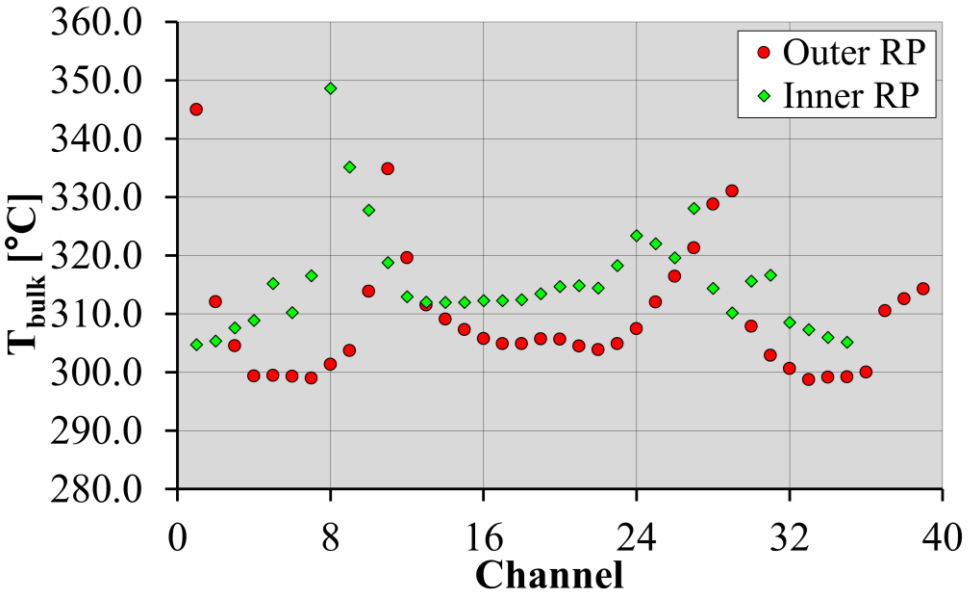

Figure 2.39. Bulk temperature distribution among RPs FW channels.

Table 2.33. Bulk temperature distributions among RPs FW channels' main parameters.

	Outer RP	**Inner RP**
T_{Max} [°C]	344.97	348.58
T_{min} [°C]	298.72	304.74
ε_T	13.41%	12.58%
<T> [°C]	309.30	315.34
σ [°C]	10.70	8.92
CV	3.46%	2.83%

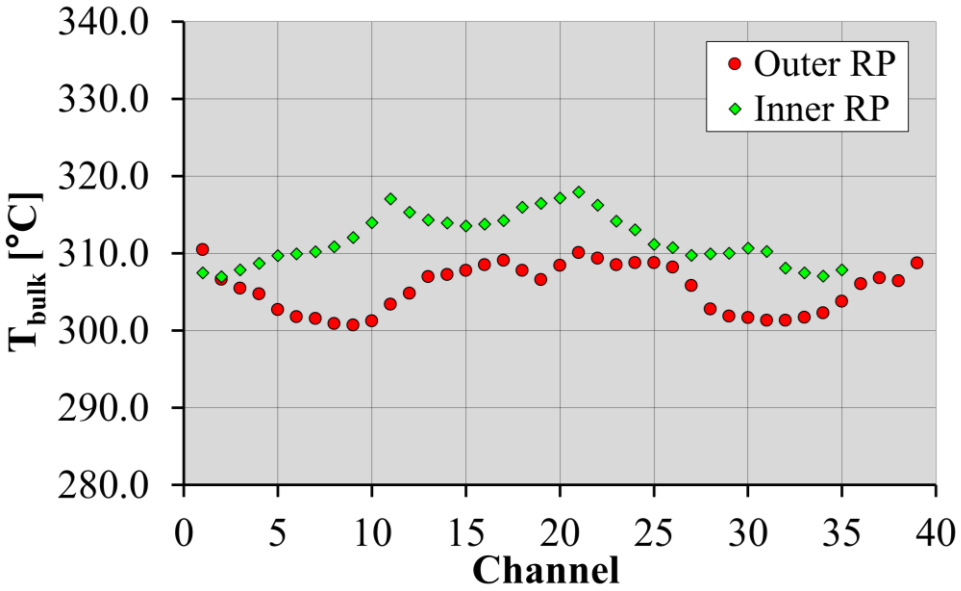

Figure 2.40. Bulk temperature distribution among RPs back channels.

Table 2.34. Bulk temperature distributions among RPs back channels' main parameters.

	Outer RP	**Inner RP**
T_{Max} [°C]	310.48	317.91
T_{min} [°C]	300.71	306.98
ε_T	3.15%	3.44%
<T> [°C]	305.41	311.81
σ [°C]	3.09	3.28
CV	1.01%	1.05%

The CHF margin for the SL and RPs FW channels was calculated using the CHF look-up tables from [47]. For the FW channels, nominal peak heat flux values of 1 MW/m² for SL and 0.2 MW/m² for RPs were used. Conservative peaking factor (f_P) values, derived from the CFD simulation, were selected for both SL and RPs.

The SL FW channels results are depicted in Figure 2.41 and summarized in Table 2.35, calculated with a f_P of ≈2.39, while those relevant to the RPs FW channels are shown in Figure 2.42 and summarized in Table 2.36, calculated with a f_P of ≈3.6.

It must be highlighted that such high f_P estimates are only observed at the extreme channels of the FW, which in general are subjected to higher heat fluxes due to the proper

geometry of these components, which are characterized by a toroidal distance between the external channels and the side walls of SL and RPs higher than the pitch between two neighbouring channels.

Nevertheless, despite the CHF margins are estimated with quite conservative f_P values, they always stay well above the recommended threshold of 1.4 in every single channel.

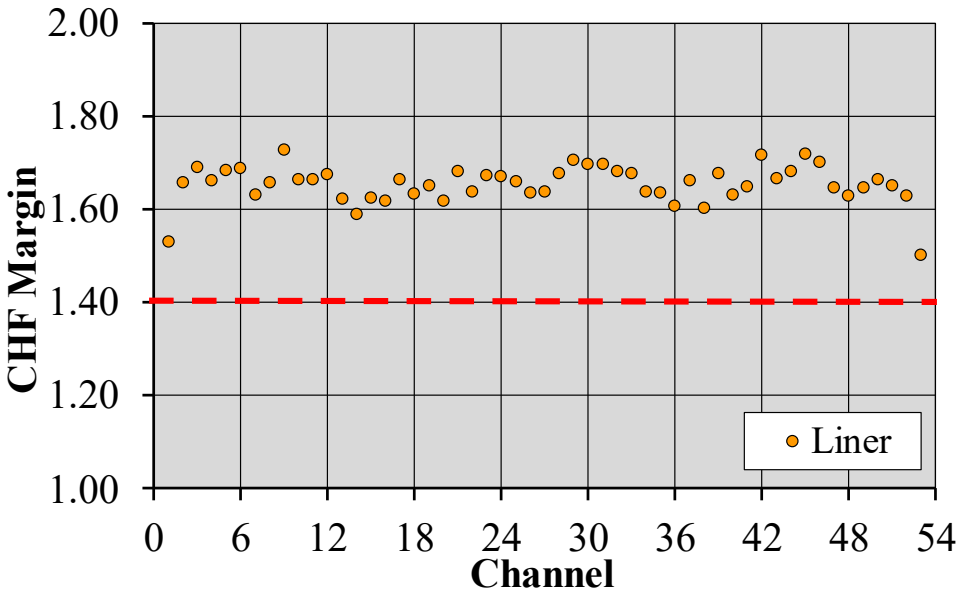

Figure 2.41. CHF margin distribution among SL FW channels.

Table 2.35. CHF margin distribution among SL FW channels' main parameters.

$(CHF\ Margin)_{Max}$	1.727
$(CHF\ Margin)_{min}$	1.529
ε_{CHF}	11.47%
<CHF Margin>	1.653
σ	0.041
CV	2.48%

With reference to the RPs FW channels results, it is possible to observe how a zero CHF margin is obtained for some channels. This occurs because they are characterized by bulk boiling and, therefore, the CHF margin criterion is not applicable.

It has to be pointed out that he correlation to be adopted would require a more specific study and, in the present case, it is not advisable to design a component which is supposed

to operate in these cooling conditions. Therefore, it is suggested to revise the design for a flow distribution improvement.

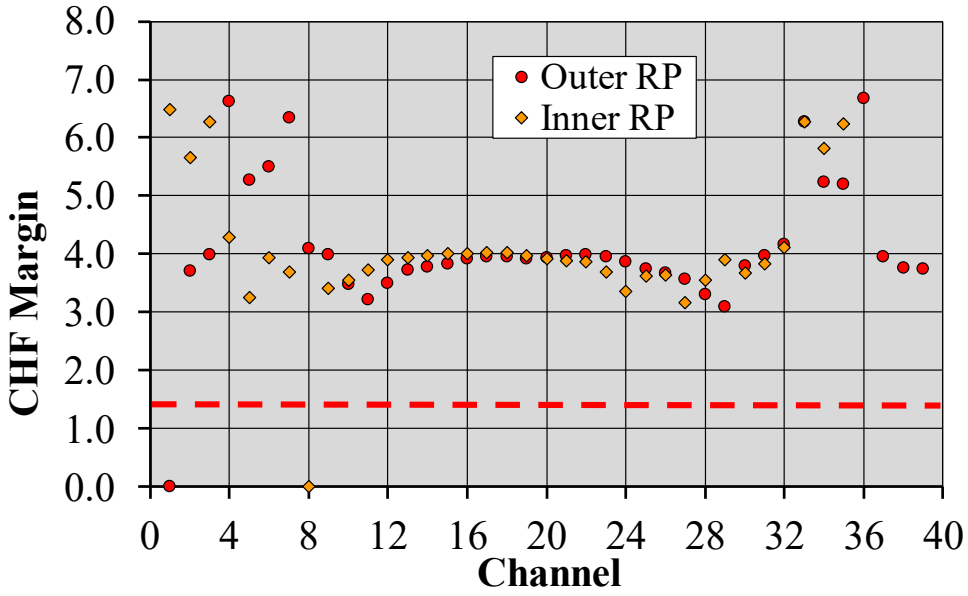

Figure 2.42. CHF margin distribution among RPs FW channels.

Table 2.36. CHF margin distribution among RPs FW channels main parameters.

	Outer RP	**Inner RP**
$(CHF\ Margin)_{Max}$	6.667	6.482
$(CHF\ Margin)_{min}$	0.000	0.000
ε_{CHF}	100.00%	100.00%
<CHF Margin>	4.120	4.077
σ	1.149	1.170
CV	27.89%	28.70%

Finally, the temperature field of the CB structure is reported for the three cases in Figure 2.43 to Figure 2.45. Additionally, the maximum temperatures for the main components of the CB are summarized in Table 2.37.

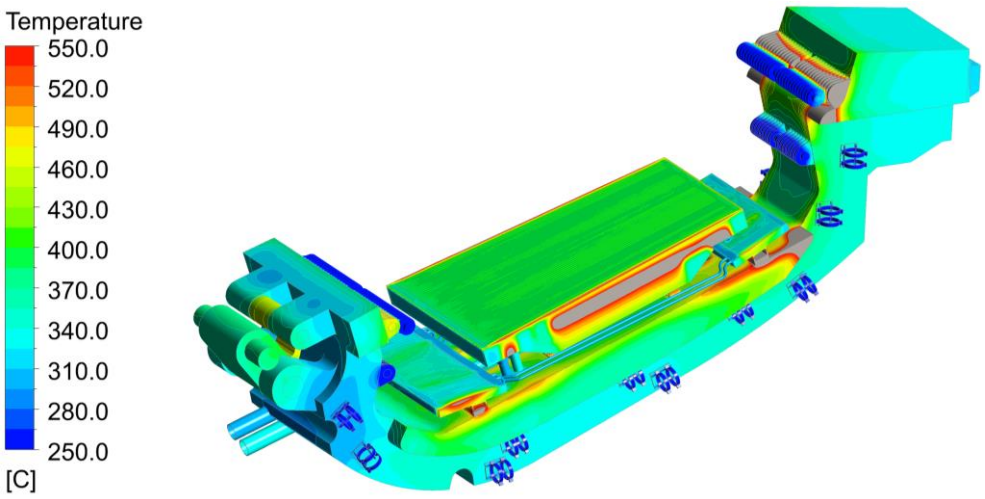

Figure 2.43. Divertor CB structure temperature field for the case with TBs in CuCrZr.

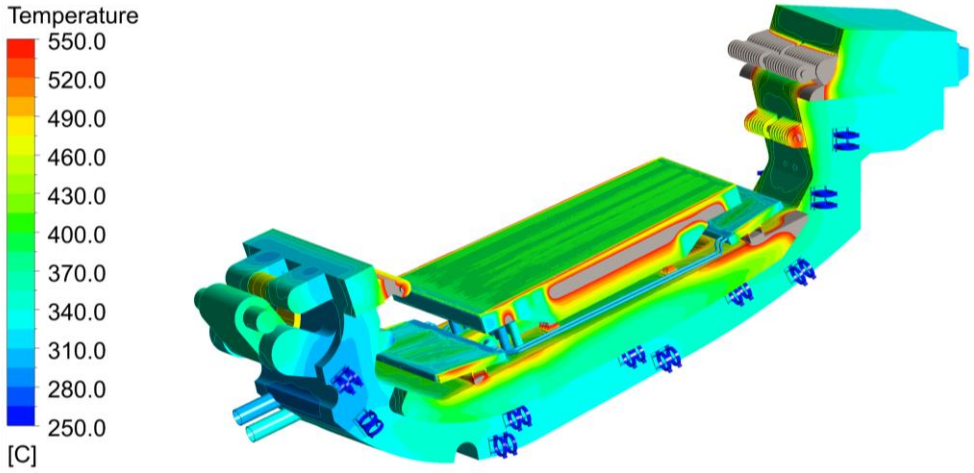

Figure 2.44. Divertor CB structure temperature field for the case with TBs in SS 316 Ti.

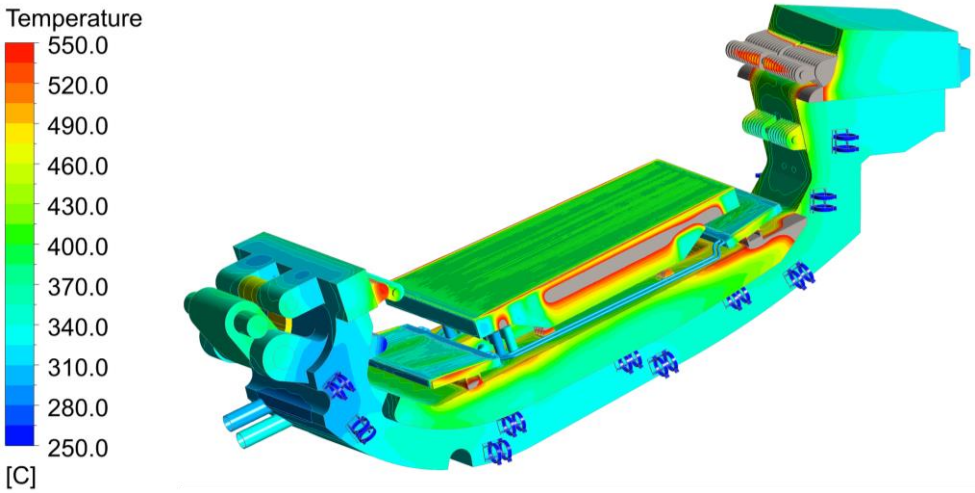

Figure 2.45. Divertor CB structure temperature field for the case with TBs in Eurofer97.

Table 2.37. Maximum structure temperature in the main divertor CB components [°C].

	CuCrZr	SS 316 Ti	Eurofer97
CB	751.13	726.99	726.75
IVT supports (Eurofer)	752.32	917.31	841.20
OVT supports (Eurofer)	480.03	599.51	548.99
SL	683.30	685.62	684.72
SL tungsten	571.55	573.85	571.25
RPs	565.29	552.76	539.29
RPs tungsten	566.55	554.05	540.55
Manifolds (RPs)	321.32	320.06	321.12
Wishbone/pins	495.22/464.01	491.77/461.46	492.23/462.06
Liner supports	573.76	574.17	573.23
IRP Support	647.06	645.16	644.99
ORP Support	560.39	557.07	557.81

2.5.3 Overall considerations on the temperature field in the divertor structure

The temperature distribution of the whole divertor structure is reported in figures from Figure 2.46 to Figure 2.48, where in grey are depicted the regions where temperatures exceeding 550°C are predicted.

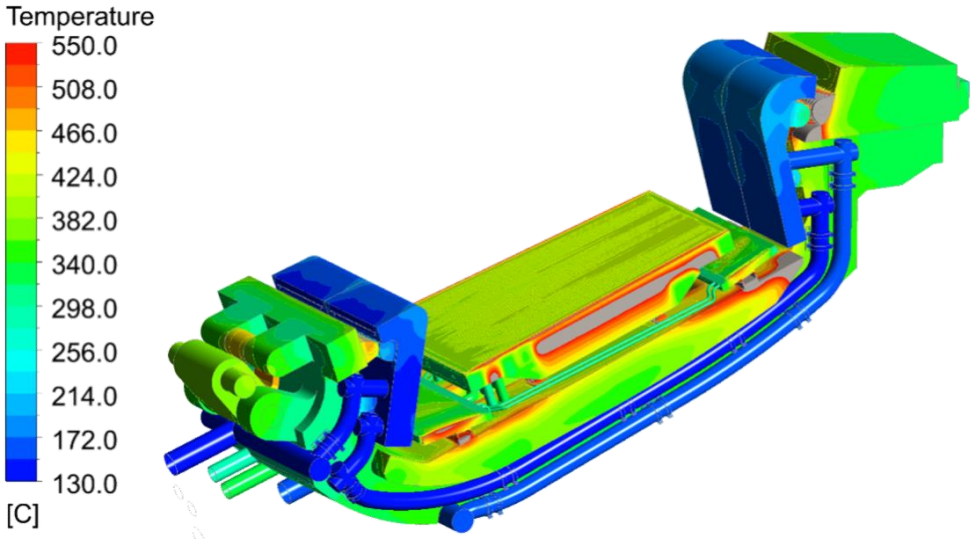

Figure 2.46. Divertor cassette structure temperature field for the case with TBs in CuCrZr.

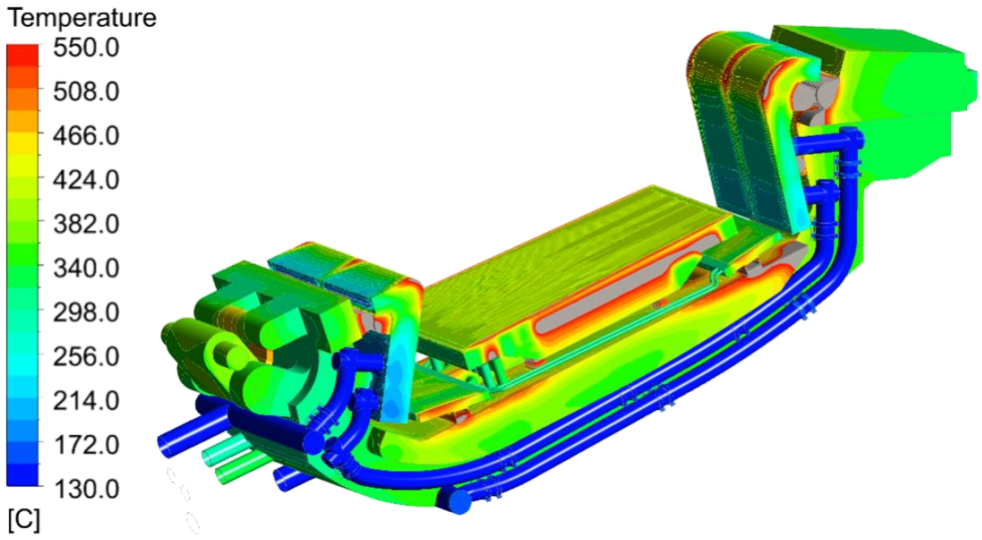

Figure 2.47. Divertor cassette structure temperature field for the case with TBs in SS 316 Ti.

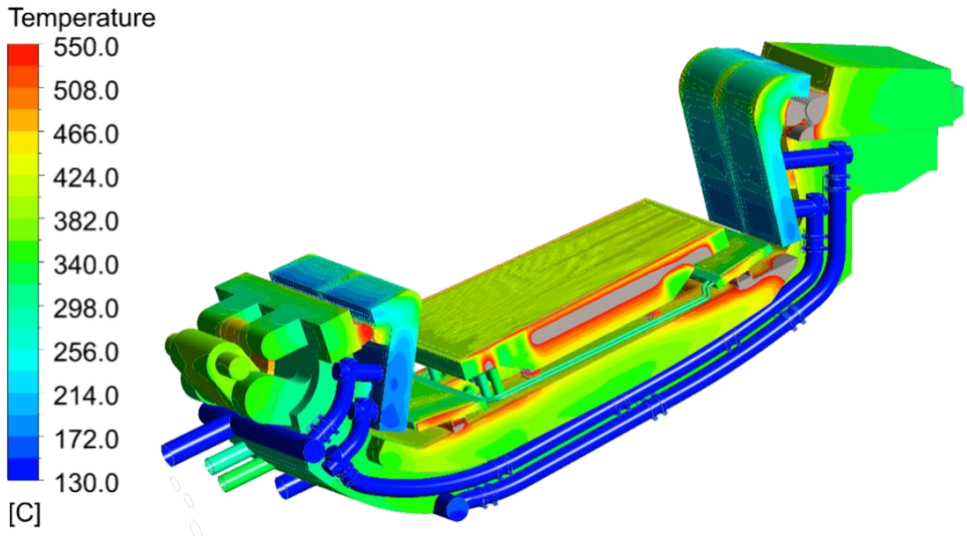

Figure 2.48. Divertor cassette structure temperature field for the case with TBs in Eurofer97.

From the analysis of the results, it might be stated that the CB cooling circuit seems not to be able to globally give quite uniform and effective cooling to the main structural part of the cassette. In fact, unduly high temperatures in the structure are observed in SL, IRP and ORP supports, IVT support systems and some CB inboard regions. In these areas, the temperature significantly overcomes the prescribed limits. Moreover, in the case of TBs in SS 316 Ti, the temperature exceeds 550°C in the Eurofer part of the OVT supports as well, with a maximum value of 600°C.

Regarding the SL, the maximum temperature reaches a value of ≈680°C in the structure of the component (differences in the order of a few degrees for the different materials). As it can be argued from the results shown before, the SL cooling circuit layout can be possibly optimised by shifting the level C of the SL back channels towards the cassette by a few

millimetres to reduce the distance between the structure and the coolant. Additionally, unduly high temperatures are predicted for the SL supports, as can be observed in Figure 2.49 for the case with TBs in CuCrZr (together with an indication of the position of the supports on the CB). This issue is not likely to be solved by rearranging the cooling system, as they require either an improvement of the SL neutron shielding or a revision of the support structure.

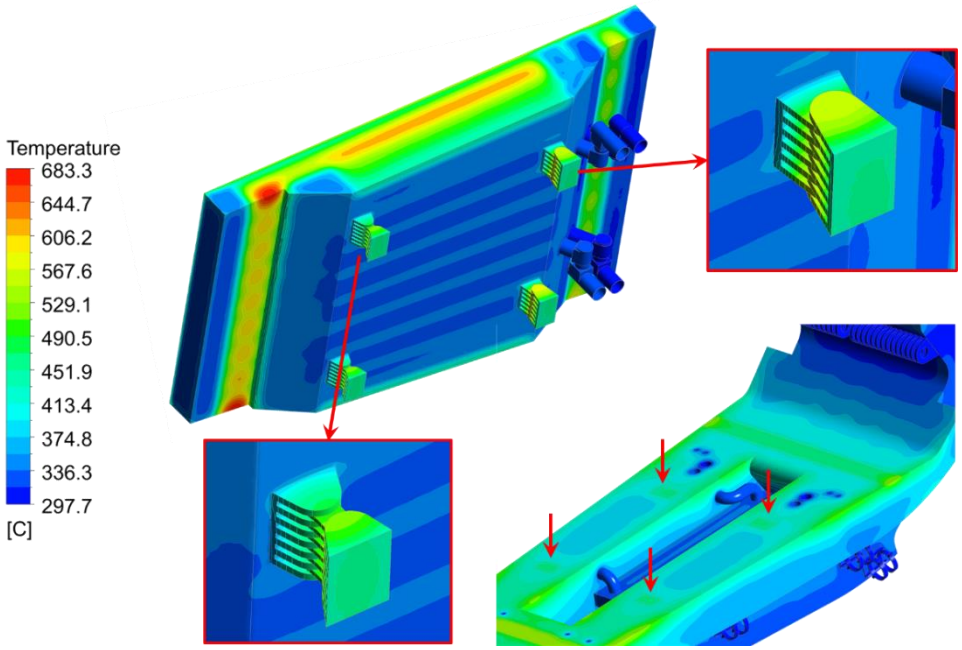

Figure 2.49. Detail of the temperature field in the SL and its supports (TBs in CuCrZr).

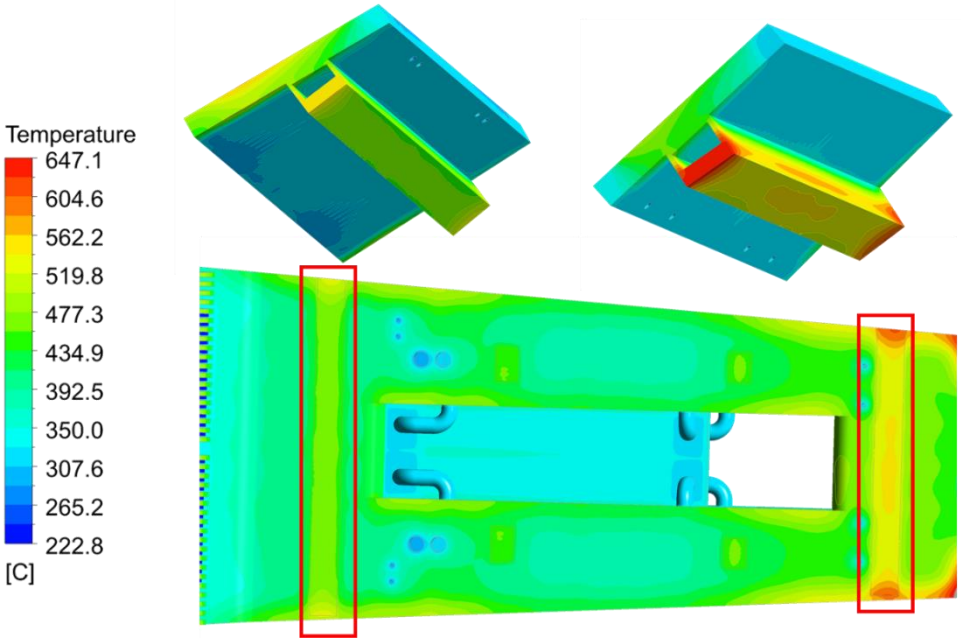

Figure 2.50. Detail of the temperature field in the RPs and their supports (TBs in CuCrZr).

Looking at the RPs dovetail supports, a detail of their temperature distribution is depicted in Figure 2.50, where it is possible to observe the attachment area of the dovetail on the CB. Looking at these regions, the maximum temperatures reach values around 645°C in the inboard RP and lower values for the outboard RP but still over 550°C. The illustrated results are relevant to the CuCrZr TBs, but analogous outcomes are obtained for the other TB materials. A possible solution to overcome the hot spots in the RPs dovetails could be the design of actively cooled supports.

Nevertheless, it is worth mentioning that these results do not take into account the issue of bulk boiling in some channels of the RPs. Therefore, the temperature field in the RPs structure may not be conservative and even higher temperatures may be observed if these effects were considered. Following the previous considerations, a design revision of the RPs cooling circuit is pivotal in order to avoid such problems.

Other design changes would be mandatory for what concerns IVT and OVT. Here, extreme temperatures higher than 600°C are predicted, independently from the TBs material adopted. In particular, the most critical case is the one with TBs in SS 316 Ti where the maximum temperature is 917°C. This is because both VTs supports are not provided with a dedicated cooling circuit and they are passively cooled by the CB and TBs coolants. It should be moreover observed that the highest temperatures are predicted on the IVT supports, as the IVT TBs are thinner (thus reducing the neutron shielding effect) and their supports are longer compared to the OVT.

Detailed pictures showing the temperature distribution in the TBs and their supports are reported in Figure 2.51 to Figure 2.56 for the three cases investigated.

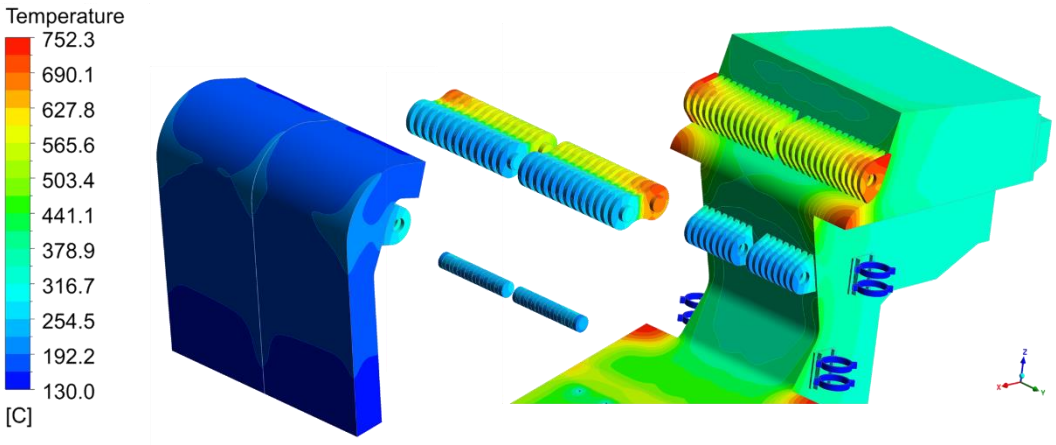

Figure 2.51. IVT fixation system temperature field (TBs in CuCrZr).

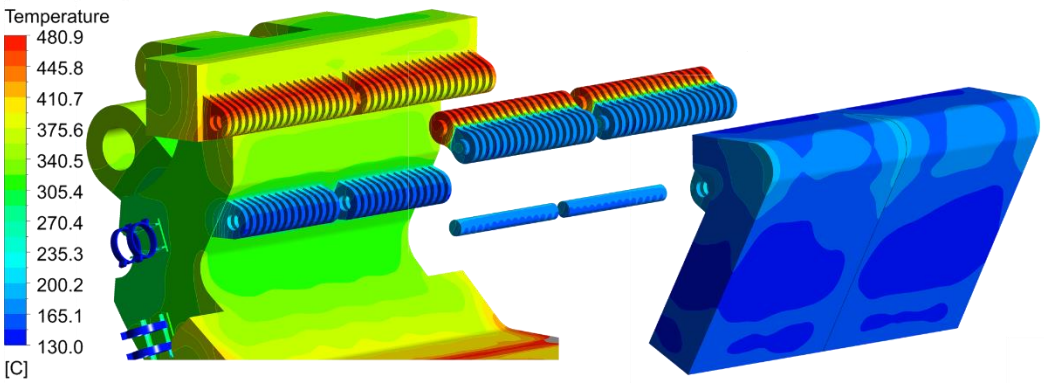

Figure 2.52. OVT fixation system temperature field (TBs in CuCrZr).

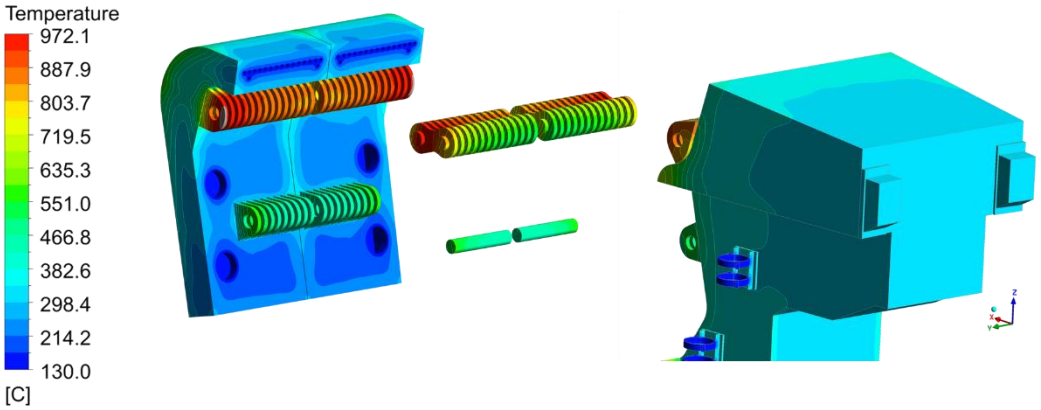

Figure 2.53. IVT fixation system temperature field (TBs in SS 316 Ti).

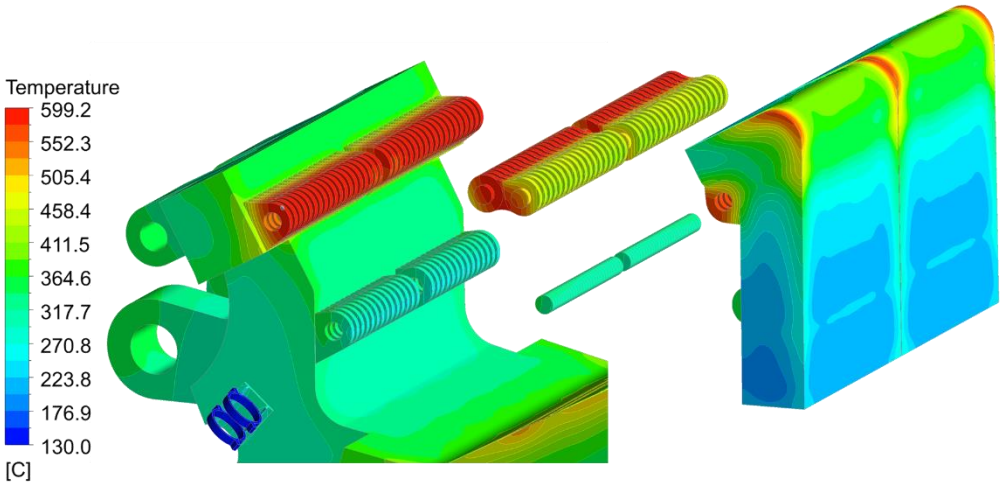

Figure 2.54. OVT fixation system temperature field (TBs in SS 316 Ti).

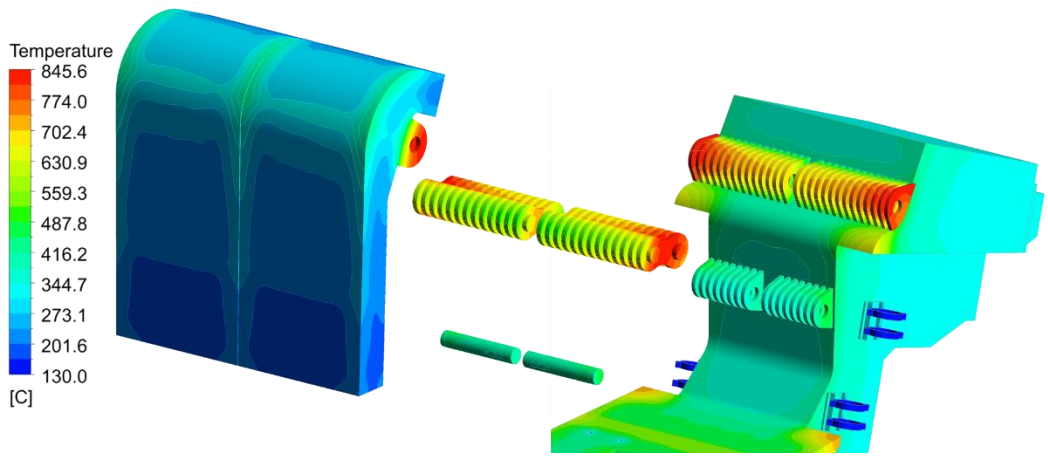

Figure 2.55. IVT fixation system temperature field (TBs in Eurofer97).

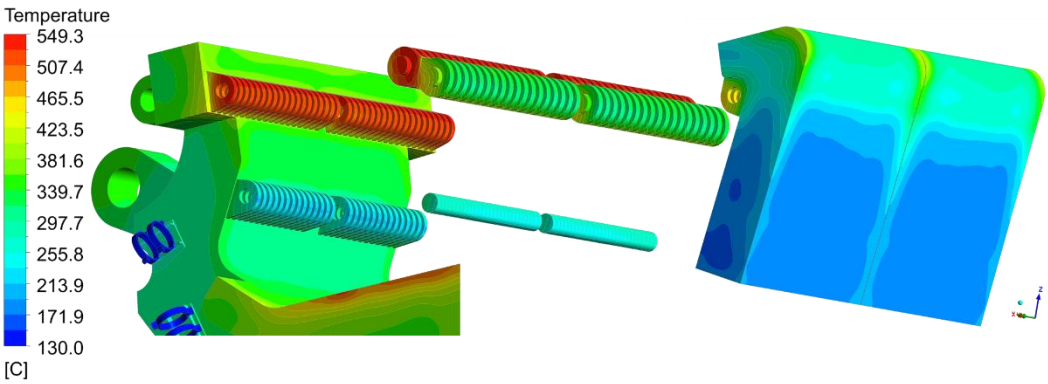

Figure 2.56. OVT fixation system temperature field (TBs in Eurofer97).

In order to improve the temperature distribution on the IVT supports, a small design change was implemented to study its impact on the results. Specifically, the toroidal length of the upper supports was reduced by removing the outermost lugs from both the CB and the TB, together with the coupled links. This solution was explored to check the effect in terms of reduction in maximum temperature on the supports, being the outermost double hinges the most critical in terms of temperature, due to their distance from the coolant and due to their higher nuclear heating. The results obtained were compared with the temperatures of the previous simulations, assuming the same simulation conditions.

The analysis was performed on the case with TBs in SS316 Ti (whose temperature field is reported in Figure 2.53) which represents the worst case in terms of temperature distributions.

The results show a slight decrease in temperature across various measurement points on the component. For instance, the maximum temperature on the Inconel supports decreased from 972.2°C to 911.5°C, on the VT side of the supports (in SS 316 Ti) from 975.6°C to 914.3°C and on the CB side (Eurofer97 supports) from 917.31°C to 831.43°C. These findings are summarized in Table 2.38. Moreover, the exploded view of the overall temperature distribution on the IVT supports is reported in Figure 2.57.

Table 2.38. Comparison of maximum structure temperature on the IVT supports [°C].

	Reference geometry	**Modified geometry**	**Difference**
SS 316 Ti supports	975.56	914.28	61.28
Eurofer97 supports	917.31	831.43	85.88
Inconel supports	972.16	911.50	60.66

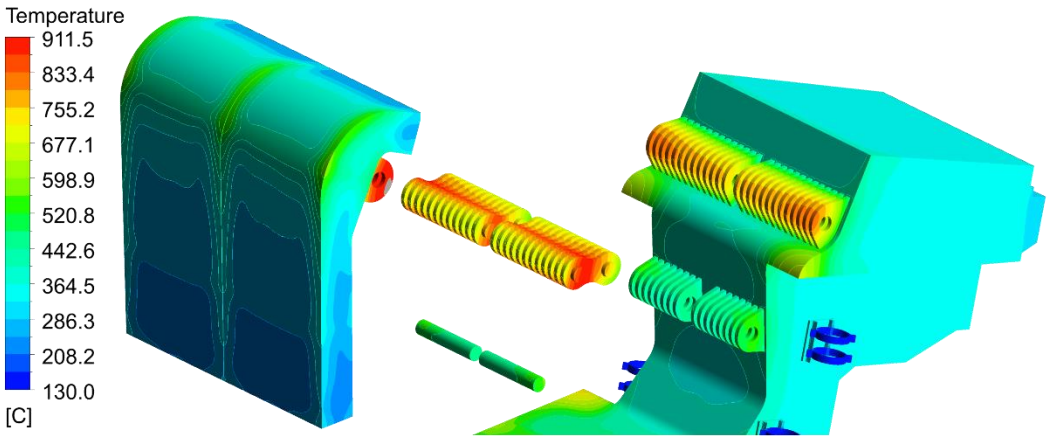

Figure 2.57. Revised IVT fixation system temperature field (TBs in SS 316 Ti).

As it can be observed, the reduction in temperature is appreciable but the overall thermal performance of the component remains largely unchanged, being the temperature still over 800°C and suggesting that the structural integrity and mechanical properties of the supports could be still significantly compromised.

Looking at the CB hot spots, there are some corners just below the inner RP and some corners under the IVT TBs (grey regions in Figure 2.58) where temperatures reach 750°C due to the geometrical features of the cassette design and the distance from the cooled

surfaces. These hot spots could be avoided by eliminating the sharp corners with thick regions of steel far from the coolant and, for example, by reducing the thickness of the inner RP dovetail support. Another solution could be providing the RP supports with an active cooling system.

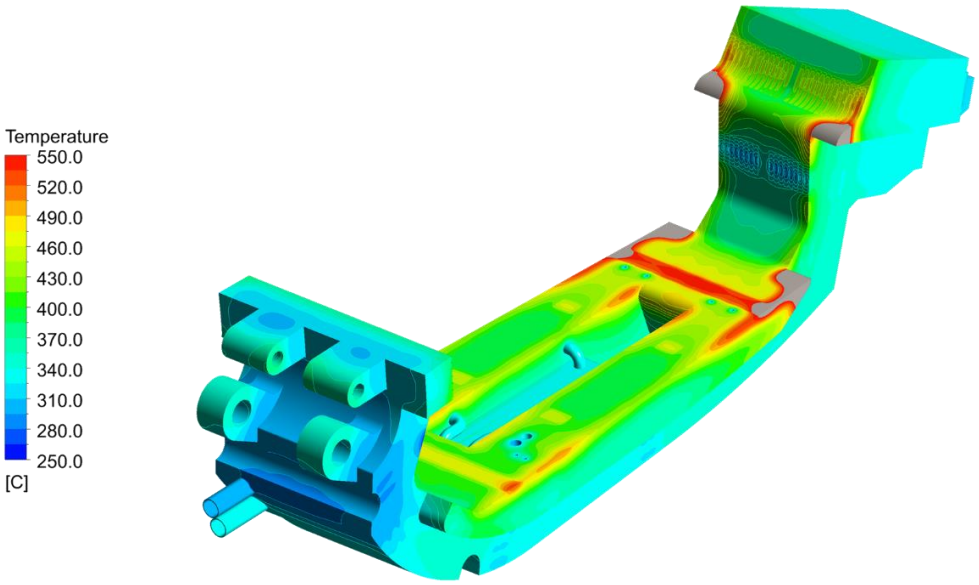

Figure 2.58. Temperature field in the CB structure (TBs in CuCrZr).

As far as the wishbone system is concerned, a detail of temperature distribution including the outboard rail section is reported in Figure 2.59, while the maximum temperature of its components is reported in Table 2.39.

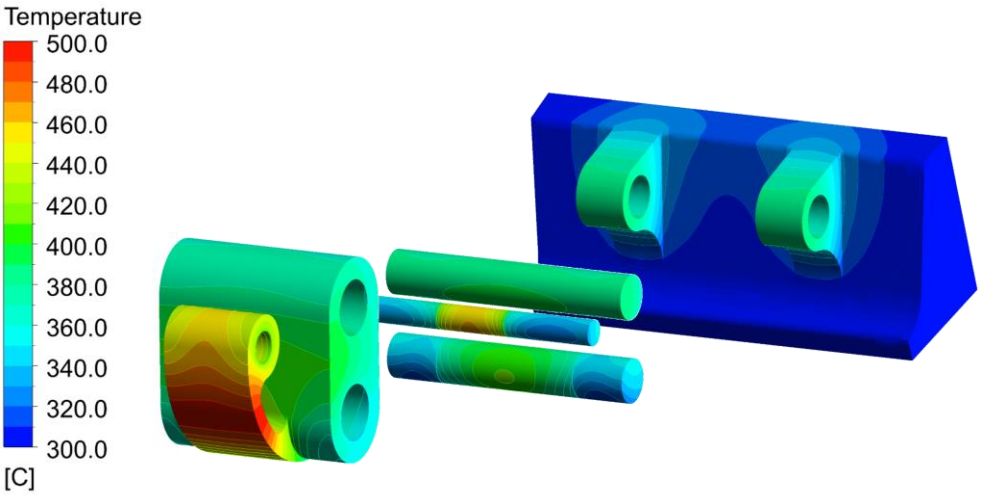

Figure 2.59. Wishbone system (including outboard rail section) temperature field (TBs in CuCrZr).

Table 2.39. Maximum structure temperature in the wishbone components.

	CuCrZr	**SS 316 Ti**	**Eurofer97**
Wishbone	495.22	491.77	492.23
Wishbone Pins	464.01	461.46	462.06
Outboard Rail	386.90	378.65	379.81

Looking at the results, the wishbone and its pins reach quite high temperatures as they are not provided with a cooling circuit. However, the temperatures reached are everywhere lower than 500°C. The maximum calculated temperature is on the wishbone side closer to the CB structure and it is around 490°C. Lower temperatures are encountered in the pins and in the outboard rail fixation system but this is deeply influenced by the BCs used for the simulation (radiation to VV at 40°C not accounting for detailed view factors). Actually, modelling the cassette as well as the primary components (blanket and VV) that are used to produce radiative heat exchange phenomena would be necessary for an accurate prediction of the temperature distribution in this component. Up to now, this is unfeasible with CFD due to the consequent unmanageable increase in computational cost. Probably, a suitable approach to cope with this issue could be the coupling of a global thermal FEM model, taking into account all the interfacing components, with a solid-fluid CFD model.

2.6 Conclusions

The activity reported in this chapter was focused on the study of the thermal-hydraulic performances of the novel DEMO divertor double-circuit cooling option.

The double-circuit cooling option divertor design was recently modified in order to operate its CB cooling circuit with an alternative set of cooling condition, being the same adopted for the WCLL BB.

Thermofluid-dynamic analyses of the entire divertor assembly were carried out introducing some innovations with respect to the previous approach adopted for such kind of studies. The whole divertor, considering both PFC and CB cooling circuits was simulated with a detailed coupled solid-fluid model 3D CFD model.

In order to obtain a realistic temperature distribution in coolant and structure domains, particular attention was given to the divertor supporting structures. For all the fixation system a dedicated material library was implemented. Additionally, as for the outboard

fixation system, including the wishbone, its pins and a section of the outboard rail, a proper radiative heat transfer condition towards the VV was implemented.

Moreover, in order to extend the life of the component, alternative materials to Eurofer97 have been investigated for the TBs of the PFC cooling circuit, i.e. CuCrZr and SS 316 Ti.

The objective of the work was the assessment of the circuit cooling capabilities and its thermal behaviour, to highlight the possible occurrence of hot spots and potential water vaporization issues.

The research campaign was carried out following a theoretical-computational approach based on the FVM and adopting the commercial CFD code ANSYS CFX and the simulations run on the CRESCO ENEAGRID HPC systems.

The results showed many advantages connected to the new divertor design and to the adoption of the alternative operating conditions.

The hydraulic behaviour in terms of pressure drops and velocity distributions can be considered acceptable, respecting most of the constraints. The pressure drops are in both circuits significantly lower than the limit of 1.4 MPa. The flow velocity distribution among SL FW and back channels and NS channels is reasonably uniform as well as in the PFU channels. Moreover, the CHF margin is above the minimum prescribed value of 1.4 for all the SL FW and PFU channels.

However, a critical issue is represented by the RPs cooling performances. In both IRP and ORP FW and back channels the velocity distribution is strongly uneven, posing the risk of bulk boiling. Looking at the saturation margin, negative values result in the RPs and they are related to poor coolant distribution inside the RP channel system. For these reasons, a complete design review of their cooling circuit layout is strongly recommended for the RPs.

Regarding the SL some external back channels, instead, the problem arises because of the distance of the structure from the outermost channels, reaching high temperatures that the coolant is not able to cool down. Moreover, additional negative saturation areas are observed in corner regions of the CB.

As for the thermal fields, it was noticed that temperatures in PFC structures reach extremely high values on the TBs and on their supports, especially for the case with TBs in SS316Ti and Eurofer97. Concerning the CB cooling circuit structure, it reaches temperatures higher than 550°C in some regions of the SL, RPs and their supports and in some inboard corners of the CB, requiring some changes in the divertor design. An interesting insight could be the introduction of actively cooled support and refining the shape of the CB in the critical areas.

Finally, it is worth noting that as possible useful further development of this study, a detailed thermofluid-dynamic model of a single PFU assembly could be performed, to evaluate the temperature distribution in the monoblock structures with a sub-modelling approach, which are currently not taken into account.

Chapter 3

3 Thermomechanical Assessment of DEMO Divertor

3.1 Introduction

The investigation of the structural behaviour of an entire assembly of DEMO divertor is one of the major challenges in the framework of the DEMO research studies. The divertor operates in a challenging loading environment, being subjected to extreme heat fluxes, neutron irradiations and particle bombardment. Thus, a reliable design of the component is needed to assure the structural integrity for the required lifetime. After the current conceptual design phase, a final design of the component is going to be studied in the engineering design phase. At the present stage, it is then necessary to develop optimize and improve the actual configuration. To this end, some preliminary structural analyses are carried out. In this dissertation, a detailed investigation of the thermo-mechanical performances of the divertor in some regions of interest was performed.

In this activity, attention has been focused on the 2022 double-circuit divertor concept, to assess the structural performances of its CB under the revised coolant high inlet pressure and high inlet temperature conditions.

The DEMO divertor is subjected to high mechanical and thermal loads. The mechanical loads are due to coolant pressure and gravitational loads causing primary stresses in the component. The thermal loads are related to the temperature field established in the component under nuclear volumetric and surface loads, generating secondary stresses. Therefore, two complementary thermomechanical aspects were studied in this dissertation. The first one was the mechanical behaviour of the CB structure subjected to the high coolant pressure due to the novel divertor operating conditions. In this regard, the CB structural response under the load combination foreseen for a typical pressure test scenario was assessed, with particular attention to the Von Mises equivalent stress and displacement

fields. Moreover, the verification of the fulfilment of the RCC-MRx structural design criteria was performed. Models, assumptions and results relevant to this first assessment are reported in §3.2.

The second aspect was the structural behaviour of the plasma-facing surfaces, which are subjected to high thermal and particle fluxes. In particular, the study was applied to a divertor plasma-facing surface which is supposed to be coated with a thin layer of Tungsten over a Eurofer97 metallic heat sink, similar to the SL and the RPs surfaces exposed to the plasma. In this framework, a theoretical-numerical assessment of the residual stresses on a typical Tungsten armour was carried out to check whether the influence of temperature-dependent mechanical properties of the materials may affect the results.

At first, a steady-state thermal problem was studied to validate analytically the numerical method adopted to assess the temperature distributions on which the thermomechanical results depend. Therefore, a transient case was studied considering constant and temperature-dependent properties. In particular, the numerical results in terms of one-dimensional armour stress obtained on MATLAB considering temperature-dependent properties were compared with the analytical results calculated with constant thermo-mechanical properties obtained in [48]. Models, assumptions and results are reported in §3.3.

3.2 Structural assessment of DEMO divertor Cassette Body

The scope of the activity was the preliminary investigation of the structural behaviour of the CB structure. under mechanical loads only (gravity and pressure loads). To this purpose, a steady-state overloading scenario that simulates a Pressure Test (PT) has been considered.

The structural performances of the divertor CB cooling circuit were assessed by following the hydrostatic test procedure of the structural design code. In particular, a 3D-FEM analysis campaign was carried out to evaluate the equivalent Von Mises stress field, the structural displacements, and the compliance of the structural behaviour of the divertor with the criteria of the RCC-MRx structural design code [49].

A theoretical-numerical approach was pursued to perform the study and it was based on the Finite Element Method and adopting the ANSYS Mechanical 2022 R1 commercial Computer Aided Engineering (CAE) code.

The assumptions and models relevant to the thermomechanical analysis are herein presented and critically discussed together with the main results obtained.

3.2.1 Description of the methodology

The primary goal of thermo-mechanical analysis for a complex 3D system like the DEMO divertor is to evaluate displacement, stress, thermal and strain fields. These fields arise within the structure due to the applied BCs and loads (of mechanical and/or thermal nature) chosen to accurately represent the problem under investigation. For the divertor, thermal loads primarily come from the heat generated in its structure and in the coolant due to heat flux coming from the plasma and from particles interactions between photons/neutrons and the structural materials.

By utilizing the pure conduction equation, which is derived as a specific instance of the thermal balance equation applied to solid bodies [50] and enforcing a series of thermal BCs designed to accurately depict the physical conditions at the boundaries of the studied domain from a thermal perspective, it becomes feasible to integrate the governing heat equation to derive the thermal field function $T(x,y,z,t)$.

It is difficult to reach an analytical solution unless the system is very regular in its geometric and physical properties and can be reduced using conjectures. On the other hand, the geometric and physical characteristics of the DEMO divertor are extremely complicated. It is therefore nearly hard to find an analytical solution to the thermal problem. Therefore, numerical methods are employed to approximate the solutions.

Concerning the stress and strain fields, they are both tensors of the second order and functions of the spatial and temporal variables. The displacement field, instead, is a vector function of spatial and temporal variables.

Under the assumption of small strains and applying the Theory of Elasticity, the solution to the thermo-mechanical problem can be derived by solving a system of equations. This system comprises indefinite equilibrium equations, strain-displacement equations, and constitutive equations [51]. The indefinite equilibrium equations represent the elementary volume equilibrium condition, encompassing translation and rotation, of a continuous 3D elastic body under stationary conditions. They are formulated as a system of 6 PDEs, with the unknowns being the 9 stress field functions.

The strain-displacement equations establish the functional relationship between the components of strain and displacement functions. This relationship ensures the continuity of the body without encountering self-penetrations or separation of fibers. The equations are formulated as a system of 9 PDEs, where the unknowns consist of the 9 strain field functions along with the 3 displacement field functions [52].

The constitutive equations, which describe how a body responds to the application of thermo-mechanical stresses, express the functional relationship between the stress and strain fields. A set of six algebraic equations represents these responses, assuming the body is homogenous, isotropic, and linear-elastic. In this system, the stress and strain fields serve as the unknowns, capturing the body's response to the applied loads [52].

To obtain the thermomechanical behaviour of the structure, it is necessary to solve a system of 21 linearly independent algebraic and PDEs (indefinite-equilibrium equation, congruence equation and constitutive equations) with 21 unknowns composed of the 9 stress field functions, the 9 strain field functions and the 3 displacement field functions.

The problem can be simplified to three coupled, second-order PDEs with non-constant coefficients, where the unknowns are the three displacement field functions [52]. The system can be solved assuming adequate BCs and the 3 displacement filed functions can be calculated.

After determining the displacement field, it is possible to evaluate the strain field using the strain-displacement equations and subsequently derive the stress field function using the constitutive equations. This sequential process allows for the solution of the thermo-mechanical problem for a three-dimensional domain.

However, obtaining an analytical solution is exceedingly complex and often unattainable, except for models with extremely regular geometry and physics. Therefore, for complex 3D systems, theoretical-numerical methods are indispensable. Various BCs can be defined based on the specific phenomena being investigated.

Numerical methods, such as the Finite Element Method (FEM), are commonly employed to approximate the solution of thermo-mechanical problems in 3D systems characterized by a high degree of structural and physical complexity. FEM, in particular, is widely utilized for its effectiveness in handling such complex problems [53].

The Finite Element Method (FEM) operates by dividing a continuum body into discrete regions called finite elements. These elements are made up by volumes with simple shapes that are juxtaposed with each other. Each element is characterized by a set of nodes, which are points where the field functions are evaluated. These nodes are connected to the nodes of adjacent elements. This approach allows for the topological approximation of a continuum body using simple domains, facilitating the resolution of governing equations.

The main assumption of FEM is that the values of the field functions within a given element are dependent on the values at its nodes through specific shape functions. These shape functions, which are analytical expressions, vary depending on the type of element selected for the analysis. [53].

At each node, a certain number of degrees of freedom are defined, each corresponding to physical variables such as temperature, stress, displacement, and pressure. The specific number of degrees of freedom is contingent upon the type of element chosen for analysis and dictates the level of approximation of the trend of the field function. This, in turn, influences the behaviour of the element.

The development of a FEM model is articulated in the following steps [53]:

- Meshing. The domain is divided into finite elements. In order to collect the node locations and element relationships, several arrays must be created. The nodal variables are assigned based on the selected element and the problem under investigation.
- Interpolation functions of governing equations. The equations for continuous field functions are simplified into algebraic equations and interpolated across elements using shape functions.
- Assembly of FE equations. The equations governing finite elements are combined to construct a matrix linking unknown node values to other parameters. Various techniques like the variational approach or Galerkin method are employed for this assembly.
- BCs selection: A set of BCs is chosen and applied according to the physical problem at hand. These conditions modify the original structure of the matrix of discretized field equations.
- Solution of the global matrix of equations. The global system of equations for finite elements, often sparse, symmetric, and positive definite, is solved using numerical methods, which can be direct or iterative.
- Post-processing of the results. Following the solution of the displacement field using the global system of equations, additional parameters such as strain and stress are computed based on the calculated independent nodal variables.

The approach above described is adopted even in several FEM codes like ANSYS Mechanical which was for the thermo-mechanical calculations reported hereafter.

3.2.2 FEM model setup

The structural analysis of the divertor CB was carried out considering the loading scenario of a PT to study the CB structural behaviour when it is subjected only to mechanical loads (pressure and gravity loads).

A 3D FEM model has been set up, starting from its geometric configuration (Figure 3.1). At first, a computational grid was generated and then, the proper sets of loads and BCs to reproduce the corresponding loading scenario were considered.

Considering this work as a preliminary stress assessment, the model geometry only includes the CB of the divertor. Instead, VTs, RPs (both IRP and ORP), and the SL were not directly included in the model, so they were considered by means of proper gravity loads aimed at simulating their weights.

Figure 3.1 Divertor CB structure.

For each of them, a point mass was placed at their centre of gravity. Here, a remote force acting along the Z-direction was applied, to reproduce their weights (see Table 3.1). Then, each reference point has been coupled to the respective attachment surfaces. A schematic representation is reported in Figure 3.2.

Moreover, the fluid weight inside the CB was considered being ≈12% of the CB weight. In particular, its hydrostatic pressure on the CB internal surface was considered to simulate the fluid weight contribution. CB and subcomponents' structure masses and CB fluid mass are reported below and evaluated at the reference temperature (22°C).

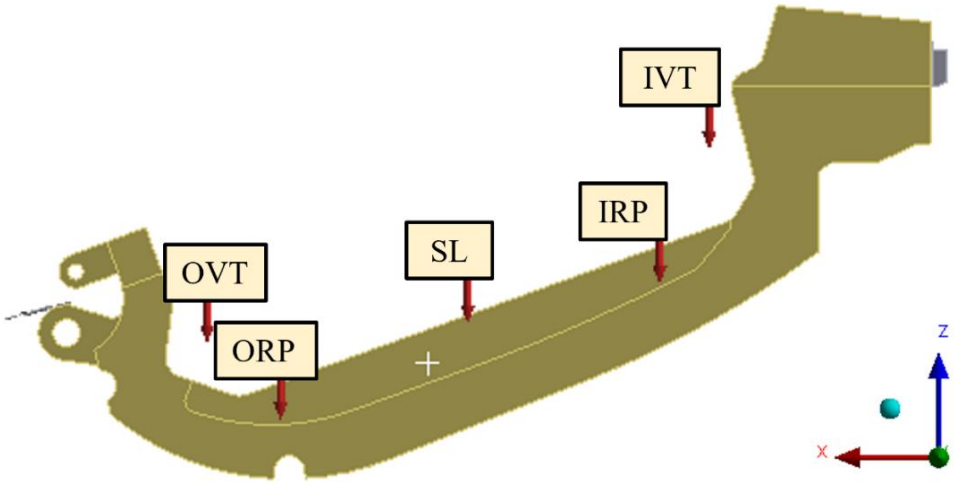

Figure 3.2 Divertor CB structure with weight loads.

Table 3.1. Masses considered for the analysis.

	Mass [kg]
CB Structure	5063.0
Liner Structures	1221.3
IRP Structure	89.6
ORP Structure	130.7
IVT Structure	1052.2
OVT Structure	1131.8
CB Fluid	595.0

As far as the mesh is concerned, a spatial discretization grid, depicted in Figure 3.3, composed of 1.65 million nodes connected in 8.7 million linear tetrahedral elements, including Inboard and Outboard support regions, has been developed.

Concerning the adopted materials, Eurofer97 steel was considered as structural material. The mechanical properties for Eurofer97, according to [54] and [39] respectively, have been considered.

Moreover, since only the mechanical loads were considered in this phase, a uniform temperature value of 22 °C (equal to the reference temperature) was imposed to the structure.

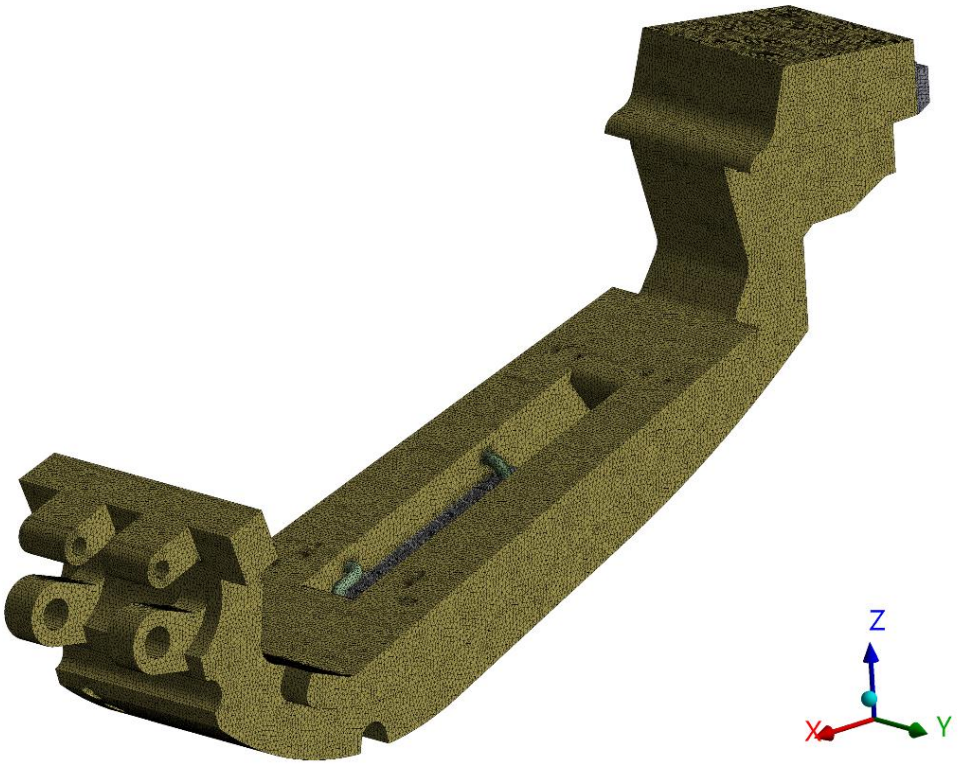

Figure 3.3 Detail of the mesh adopted for the structural analysis of the divertor CB.

The divertor is connected to the VV through two different support systems on the inboard and outboard sides, which are described in §1.3.

The wishbone system of the outboard region has been simulated by means of a spring connected to the outboard support, properly modelled, as reported in Figure 3.4. The spring acts along its longitudinal direction with an elastic spring constant equal to 19600 N/mm [14]. The spring was placed at the centre of gravity of the two-pin system. Moreover, at the surface of the outboard supports, displacements along Y_L and Z_L directions (in the spring coordinate system) were suppressed (surfaces in yellow in Figure 3.4).

In the inboard region, two nose supports were considered and all the displacements were prevented to the nodes lying on the green surfaces depicted in Figure 3.5.

Finally, considering the internal pressure, to reproduce the presence of the coolant inside the divertor CB internal channels, an increased pressure value compared to the normal operating one was adopted for the PT scenario. In particular, a value of 25.6 MPa has been considered, according to the hydrostatic test procedure reported in REC 3257.4 of RCC-MRx-2012 [49].

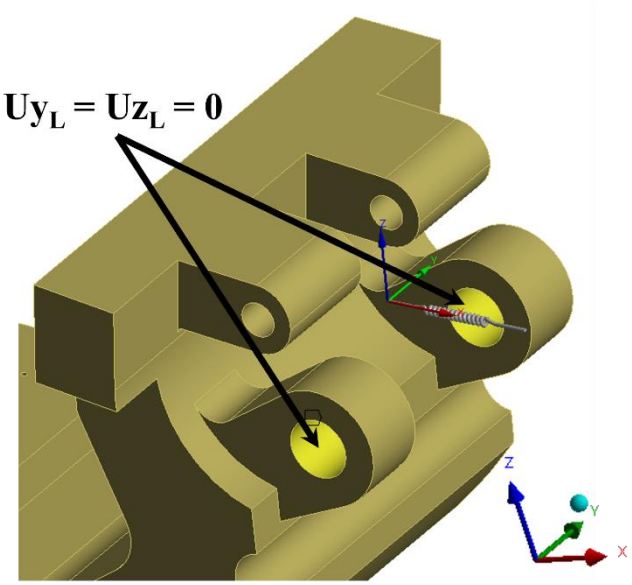

Figure 3.4 Outboard supports mechanical constraints.

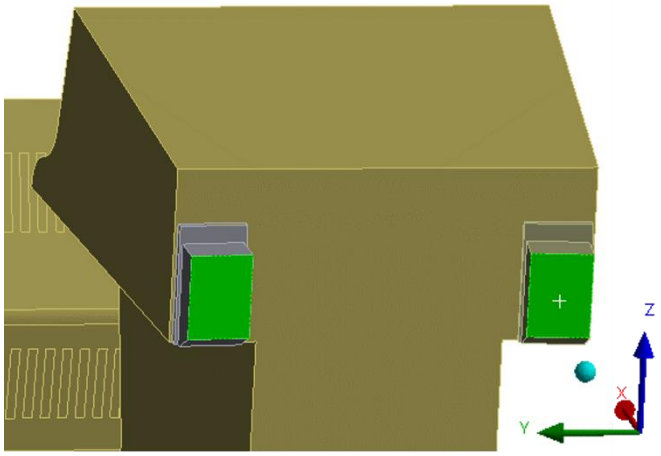

Ux = Uy = Uz = 0

Figure 3.5 Inboard supports mechanical constraints.

3.2.3 Results

Steady-state analyses have been run to study the mechanical behaviour of the divertor under the PT loading scenario, in compliance with the RCC-MRx structural design code. In Figure 3.6 the Von Mises equivalent stress field is reported. Looking at these pictures, it is possible to notice that the component appears to be globally poorly stressed with some exceptions, in particular in the regions below the RPs and SL and in the inboard side structure.

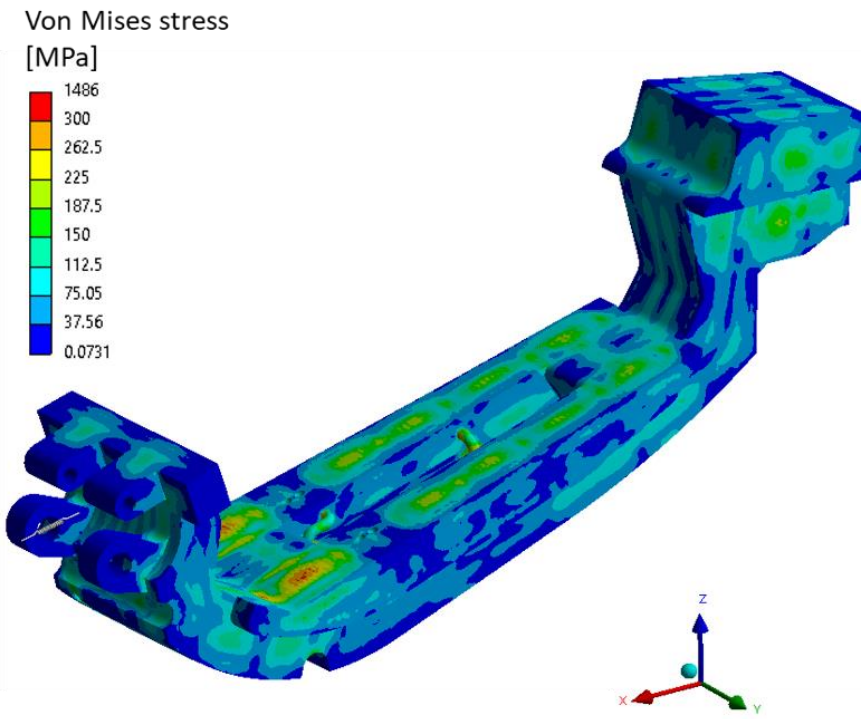

Figure 3.6 Divertor CB Von Mises stress field.

The displacement fields and the deformed versus undeformed shapes, isotropically amplified 3 times, are reported in Figure 3.7. Looking at the deformation fields, it can be noted that small displacements have been obtained (maximum displacement of ~ 1.4 mm), probably due to the connection strategy adopted for the divertor inboard and outboard fixation systems.

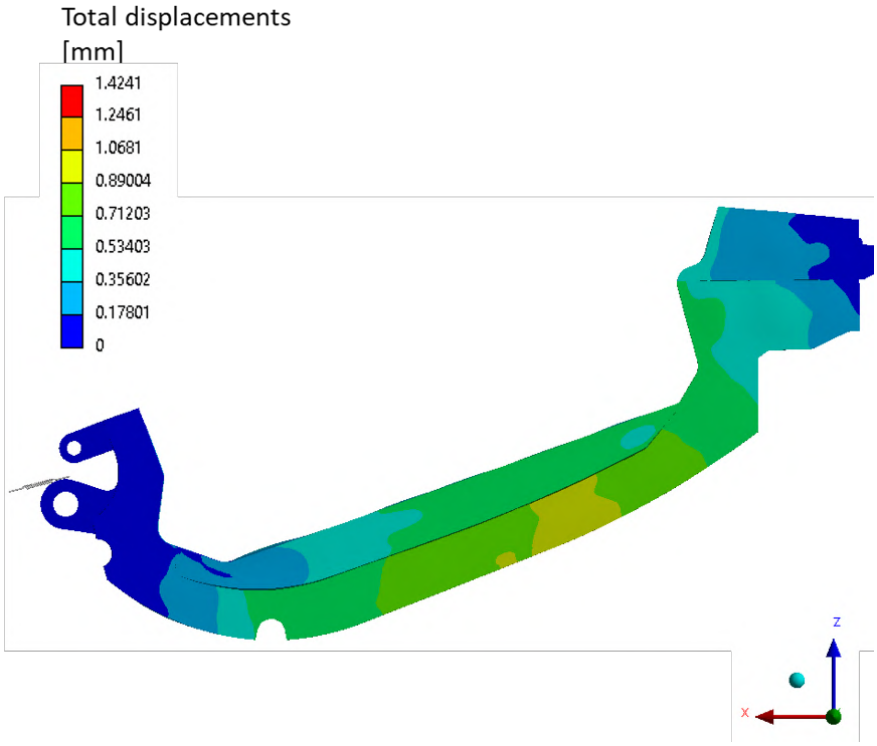

Figure 3.7 Divertor CB total displacement field.

A stress linearization procedure was done to verify the fulfilment of the RCC-MRx design criteria [49]. As prescribed by the rules, a PT loading condition is considered among the 3rd category of operating conditions and the criteria to be met for this category shall be at least as severe as those of level C. Moreover, since the PT scenario is operated at room temperature, the criteria which take into account the primary stresses were involved in the verification (referred to as type P damages in the design code), since this analysis was performed considering only mechanical loads.

In this regard, two criteria were considered and reported in Table 3.2 being the Immediate Excessive Deformation (IED) and the Immediate Plastic Instability (IPI). The parameters that appear in Table 3.2 have to be chosen according to the relative Level of criteria, defined to protect the component from different kind of damages.

Therefore, the S_m is the maximum allowable primary membrane stress intensity of the material, related to the level C. The factor K_{eff} is, instead, a "plastic collaboration coefficient". Conservatively, the value of S_m, for the PT scenario, the corresponding S_m value at 22°C was considered, as this scenario is intended to reproduce a component test condition in which the component does not reach nominal temperatures.

Table 3.2. Summary of divertor cooling circuit operative conditions.

Damage mode	Criterion
Immediate Excessive Deformation (IED)	$\frac{P_m}{S_m} < 1$
Immediate Plastic Instability (IPI)	$\frac{P_m + P_b}{K_{eff} \cdot S_m} < 1$

The stress linearization procedure was performed along some significant paths located within the most stressed regions of the structure. These areas are reported in Figure 3.8 where all the regions characterized by a VM equivalent stress higher than 450 MPa are highlighted in red.

The nomenclature of the selected paths has been arranged by subdividing the central part of the CB in the 7 toroidal-radial regions (from Y1 to Y7) and poloidal sections, so to ease the understanding of the path location. These regions are highlighted in Figure 3.9.

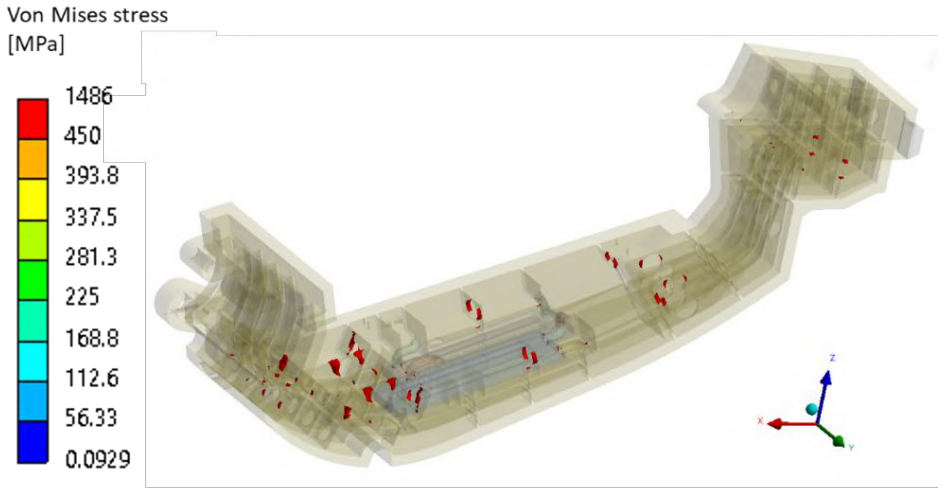

Figure 3.8 Most stressed regions of the model.

The paths selected within the Y1 and Y2 regions are, respectively, reported in Figure 3.10 and Figure 3.11. The paths within the outboard side of regions Y3, Y4 and Y5 and on the inboard side of regions Y3 and Y5 are respectively reported in Figure 3.12 and Figure 3.13. Finally, the paths selected in regions Y6 and Y7 are reported in Figure 3.14 and Figure 3.15. In all these pictures, the paths are shown as superimposed on the VM stress field obtained. Moreover, it has to be highlighted that the path selection figures only aim at qualitatively showing the path locations as the paths are selected inside the material thickness.

The RCC-MRx results relevant to the aforementioned paths are reported in Figure 3.16 and Figure 3.17.

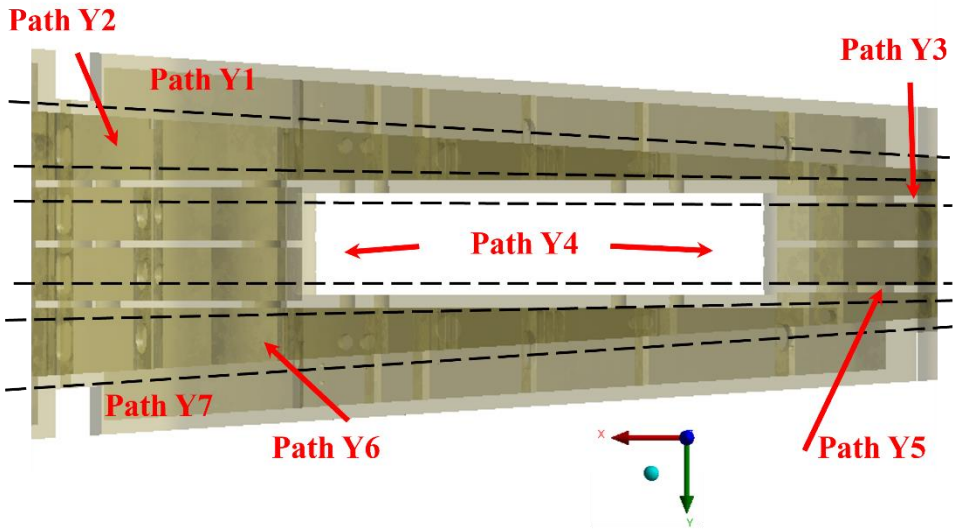

Figure 3.9 Toroidal-radial regions Y1, Y2, Y3, Y4, Y5 and Y6.

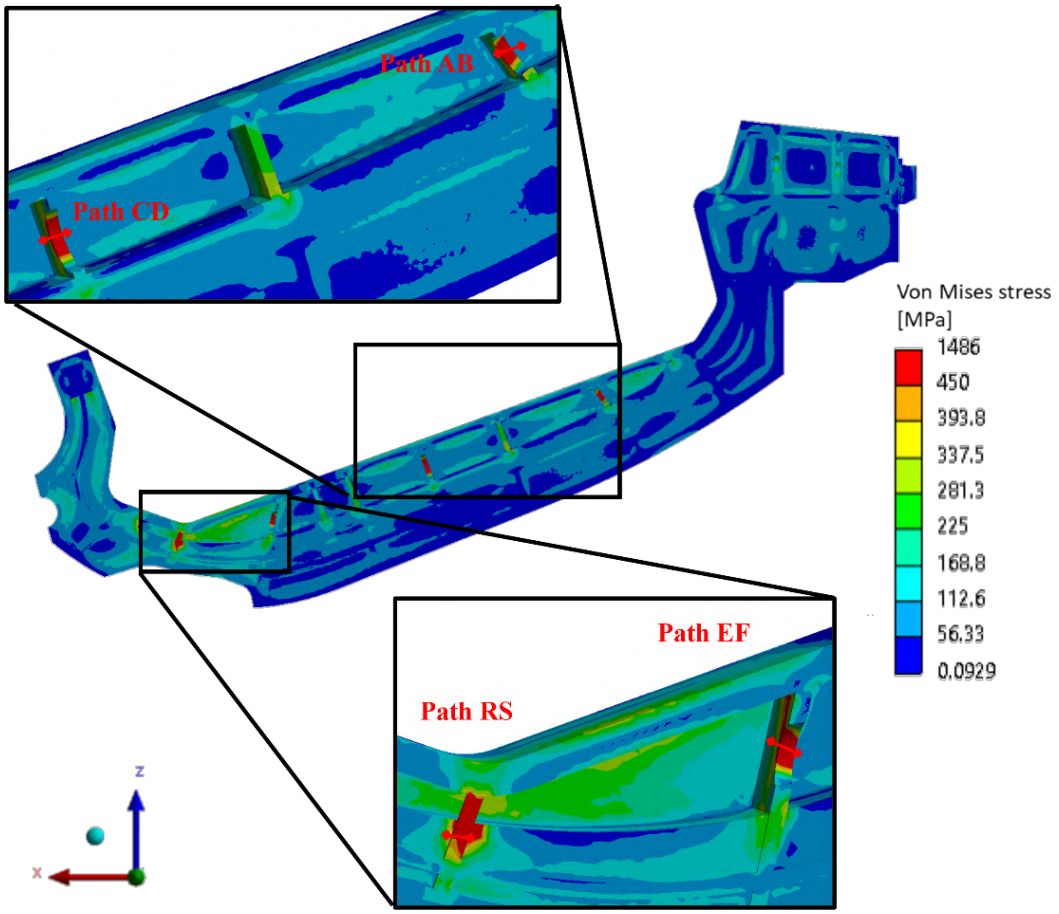

Figure 3.10 Path selected within region Y1.

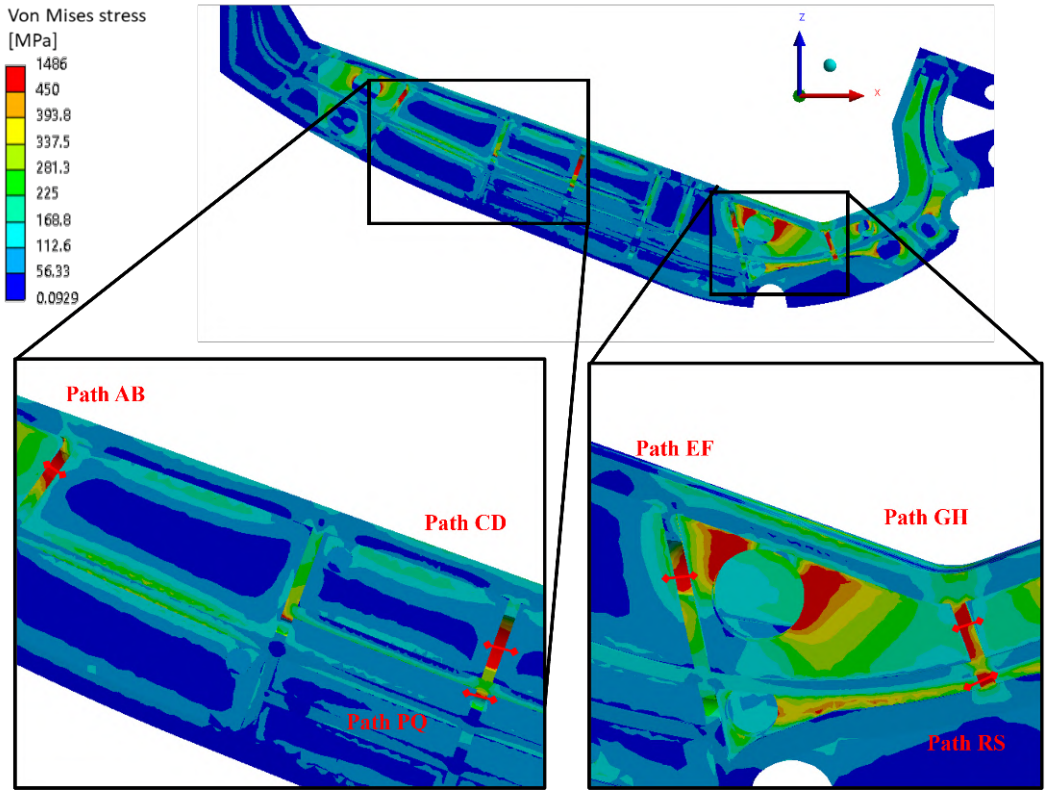

Figure 3.11 Path selected within region Y2.

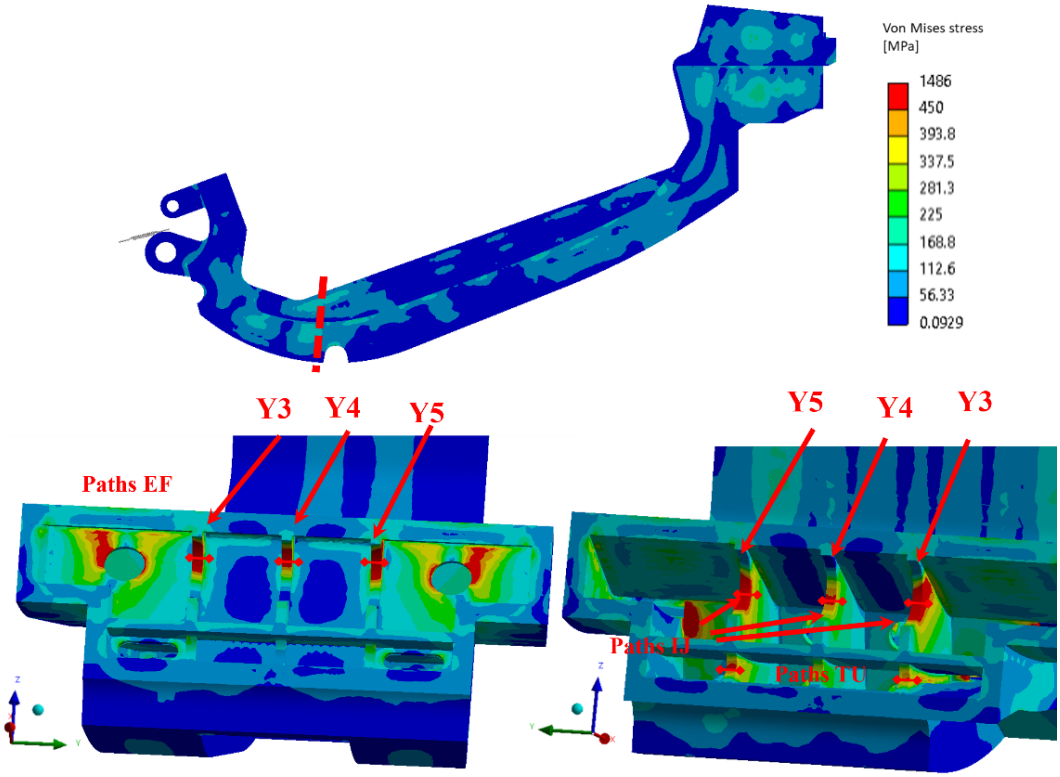

Figure 3.12 Path selected within outboard regions Y3, Y4 and Y5.

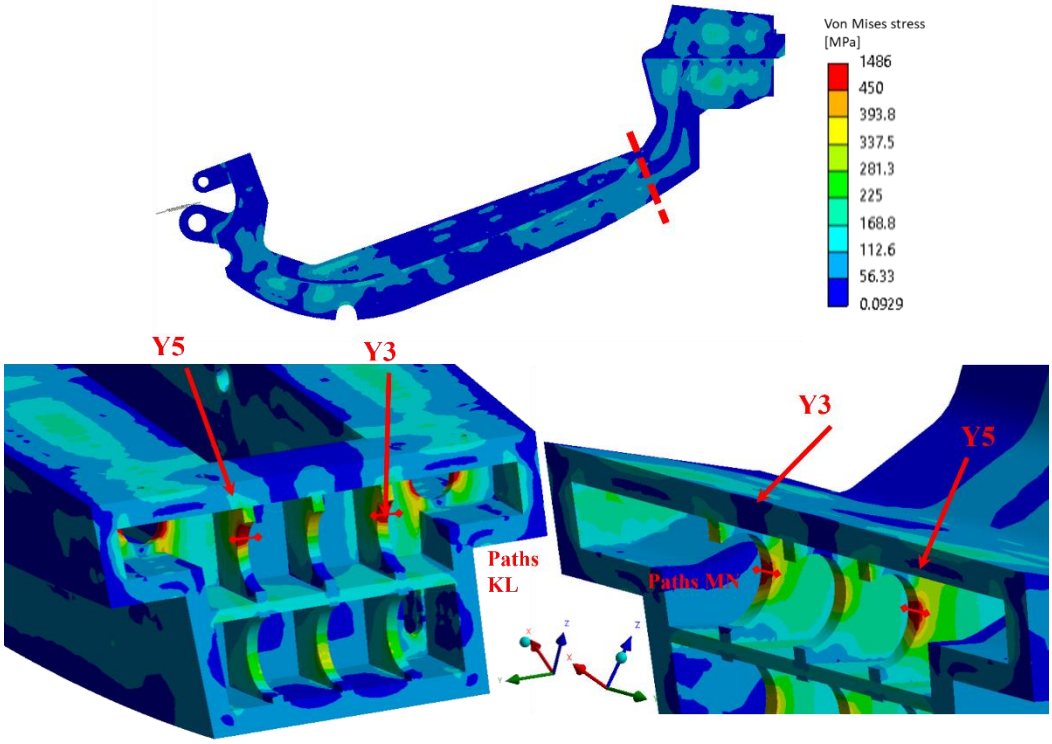

Figure 3.13 Path selected within inboard regions Y3 and Y5.

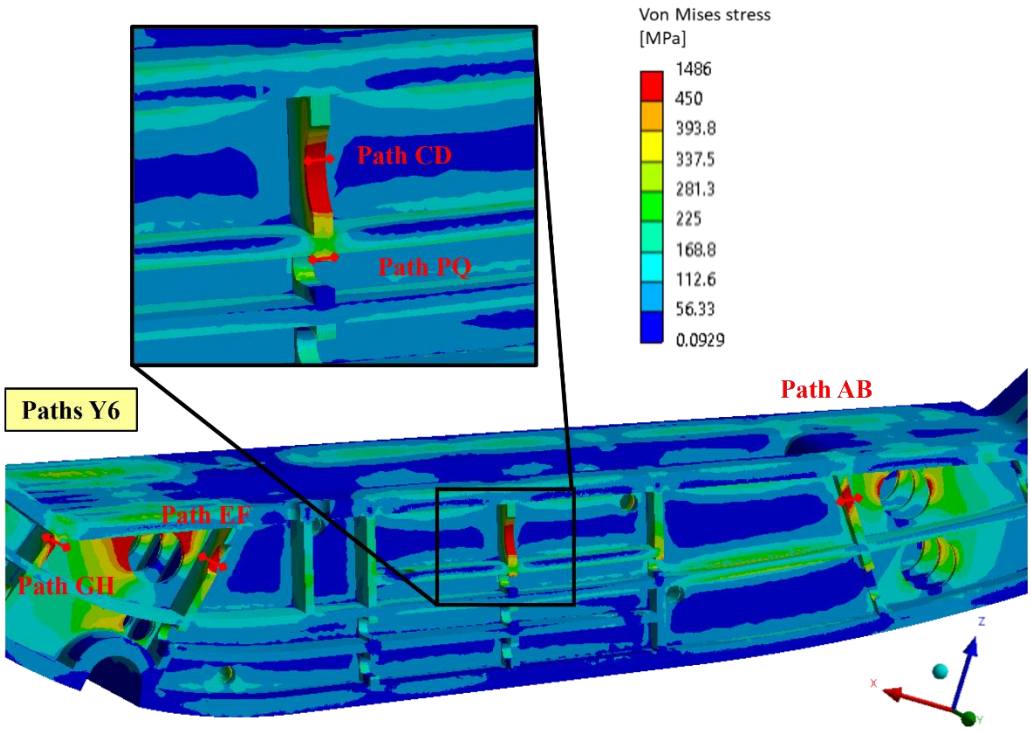

Figure 3.14 Path selected within regions Y6.

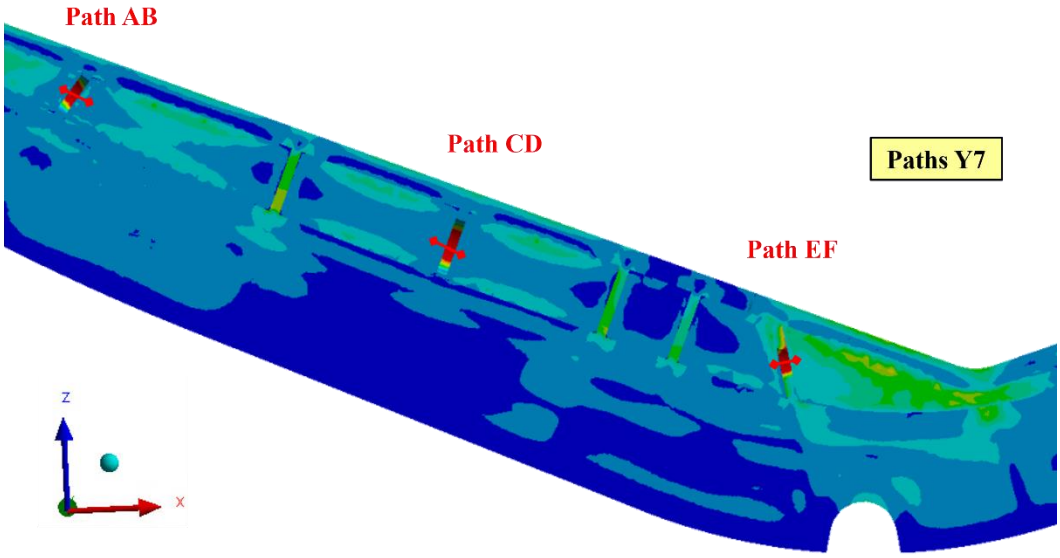

Figure 3.15 Path selected within regions Y7.

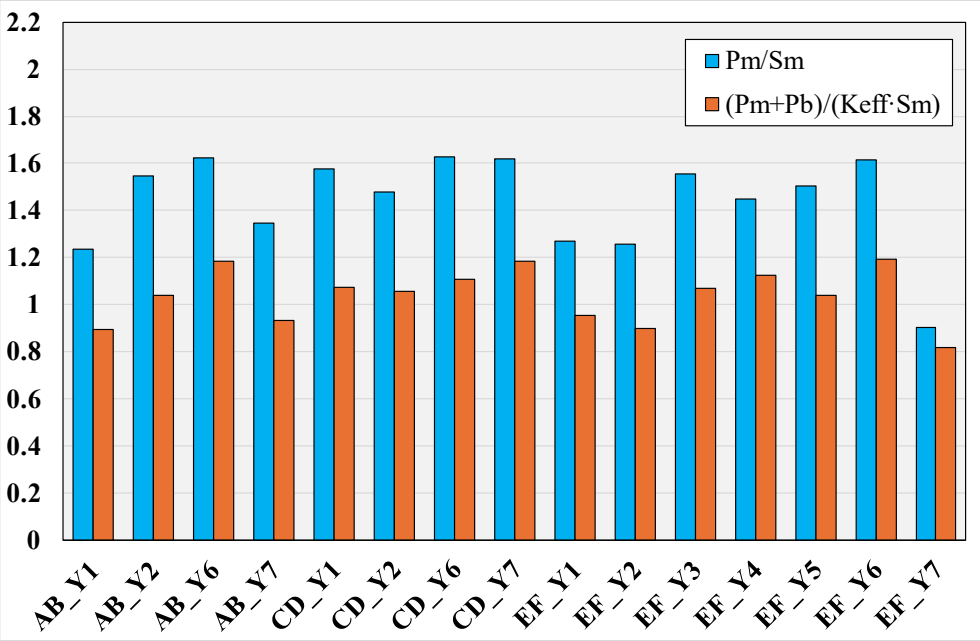

Figure 3.16 RCC-MRx criteria verification within regions from Y1 to Y7.

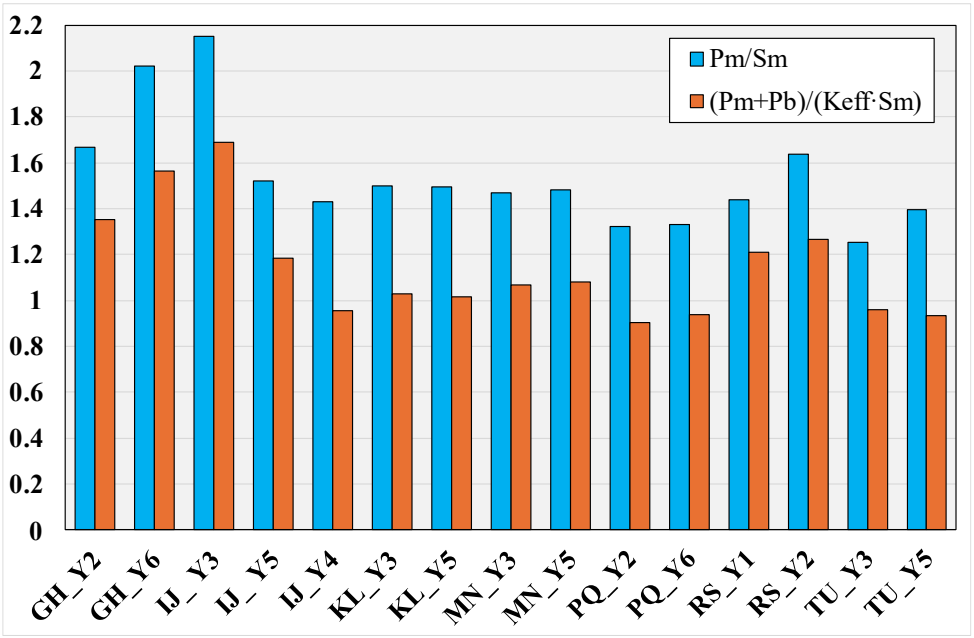

Figure 3.17 RCC-MRx criteria verification within regions from Y1 to Y6.

Other paths were identified in some other stressed regions, highlighted in Figure 3.8. In particular, some paths were chosen on the inboard and outboard CB regions, and they are reported in the following Figure 3.18 and Figure 3.19. The pertaining RCC-MRx results are reported for the inboard and outboard CB paths in Figure 3.20.

Moreover, additional paths were identified in the NS structures. They were reported in Figure 3.21 and Figure 3.22. the RCC-MRx results for NS paths are reported in Figure 3.23.

The outcomes in terms of RCC-MRx criteria verification allowed to select the most critical regions where further design improvements and refinements should be focused on.

Considering the whole CB structure, the selected paths do not fulfil the two criteria with some exceptions for the IPI. This behaviour could be a combined effect of the small thickness of the CB stiffening plates subjected to the high pressure and the CB constraints. In any case, most of the paths slightly overcomes the limit.

Most critical regions have been highlighted near paths GH Y6 and IJ Y3 where the primary membrane stress is two times higher than the limit, and close to the inboard path AB 1. In particular, attention to design improvements should be particularly paid to increasing the CB internal ribs thickness.

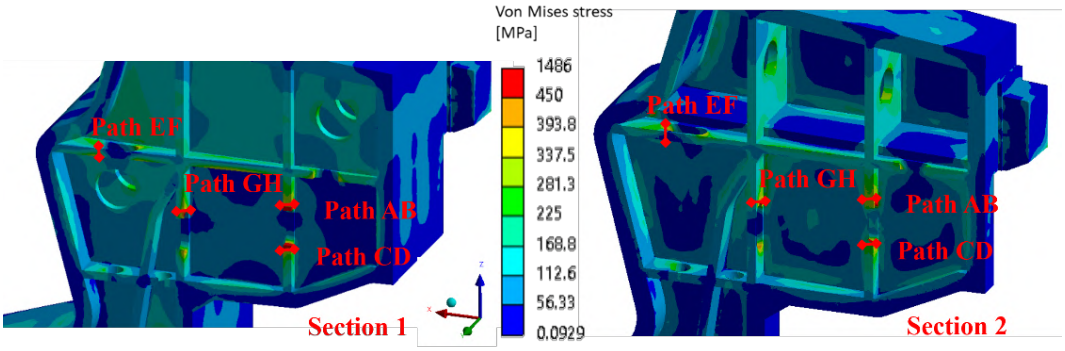

Figure 3.18 Path selected within inboard divertor cassette.

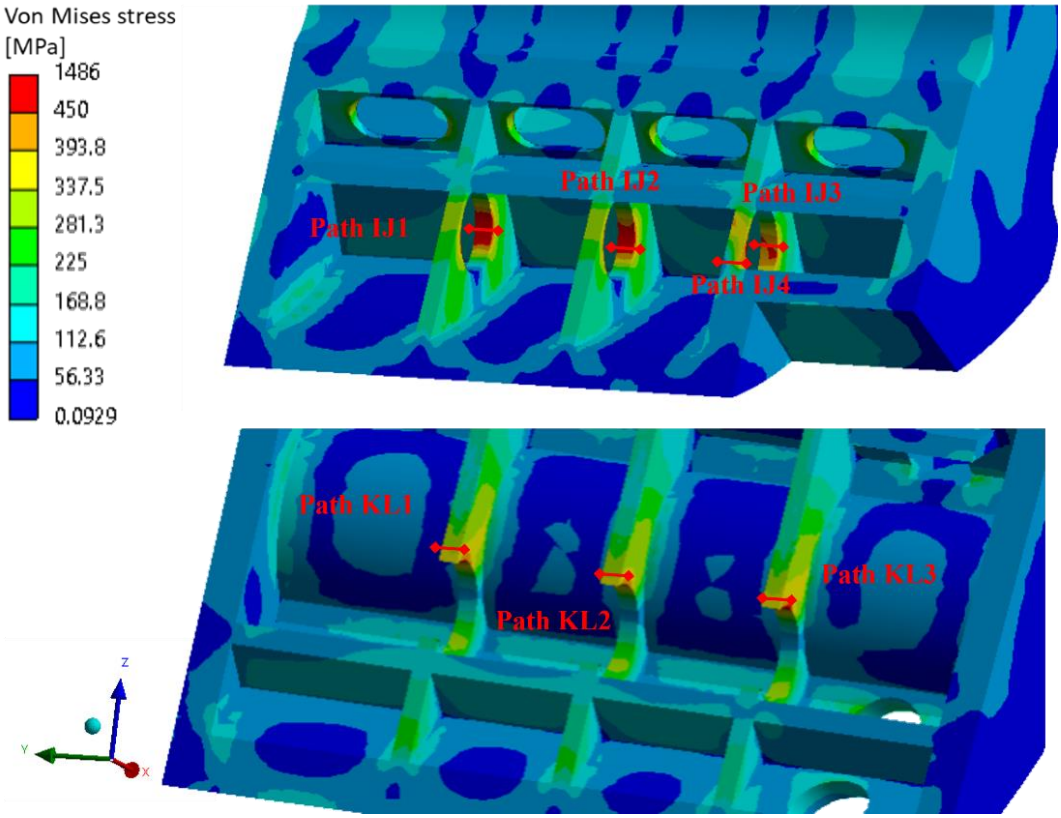

Figure 3.19 Path selected within outboard divertor cassette.

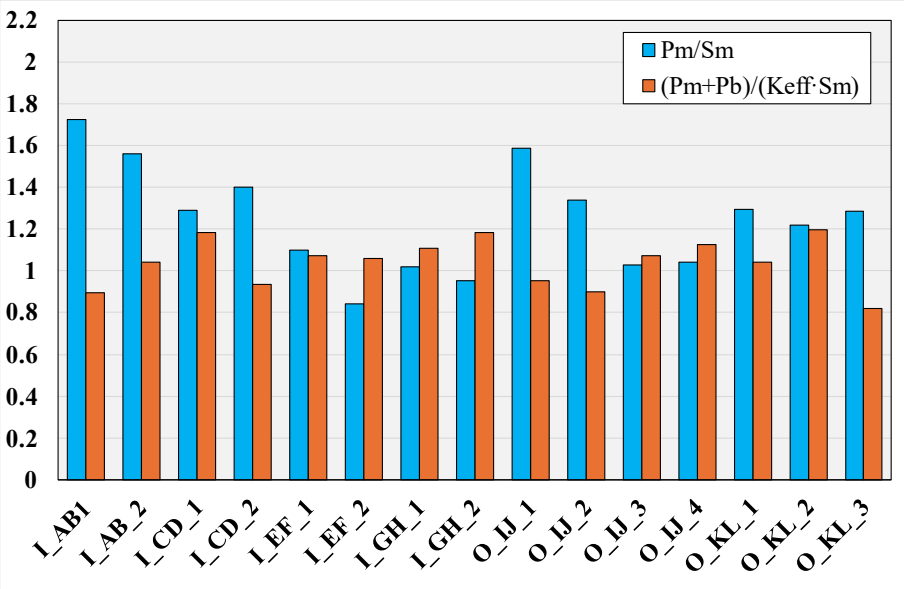

Figure 3.20 RCC-MRx criteria verification within inboard (I) and outboard (O) regions.

As for the Upper and Lower NSs, results showed that almost all the paths fulfil the selected criteria, with the exception of the paths A1 and A2 in the Lower NS and C4 in the Upper NS. However, some paths reach high values of the same criterion without overcoming the limit.

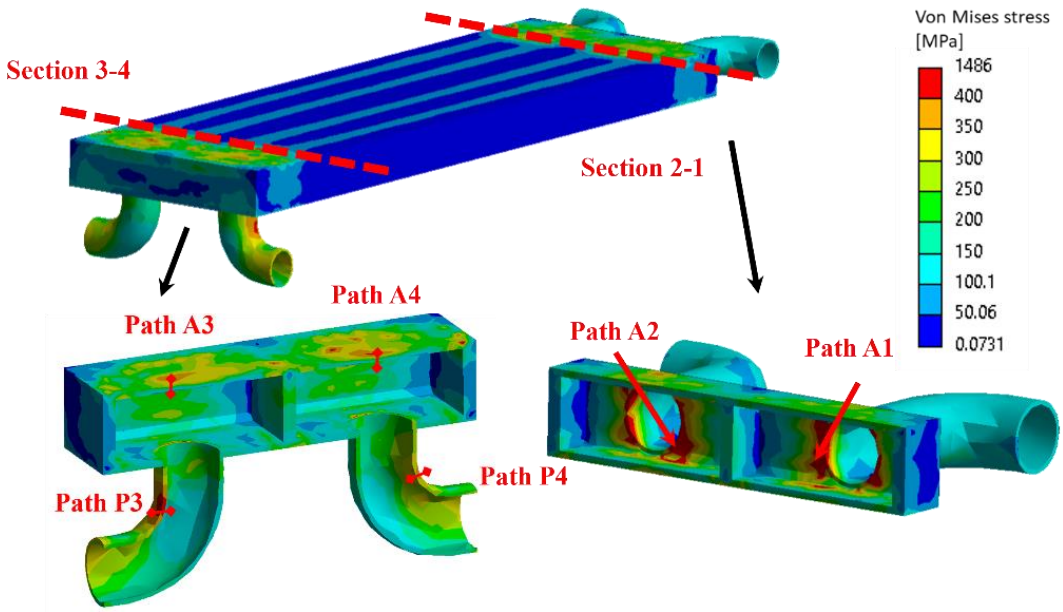

Figure 3.21 Path selected within lower NS.

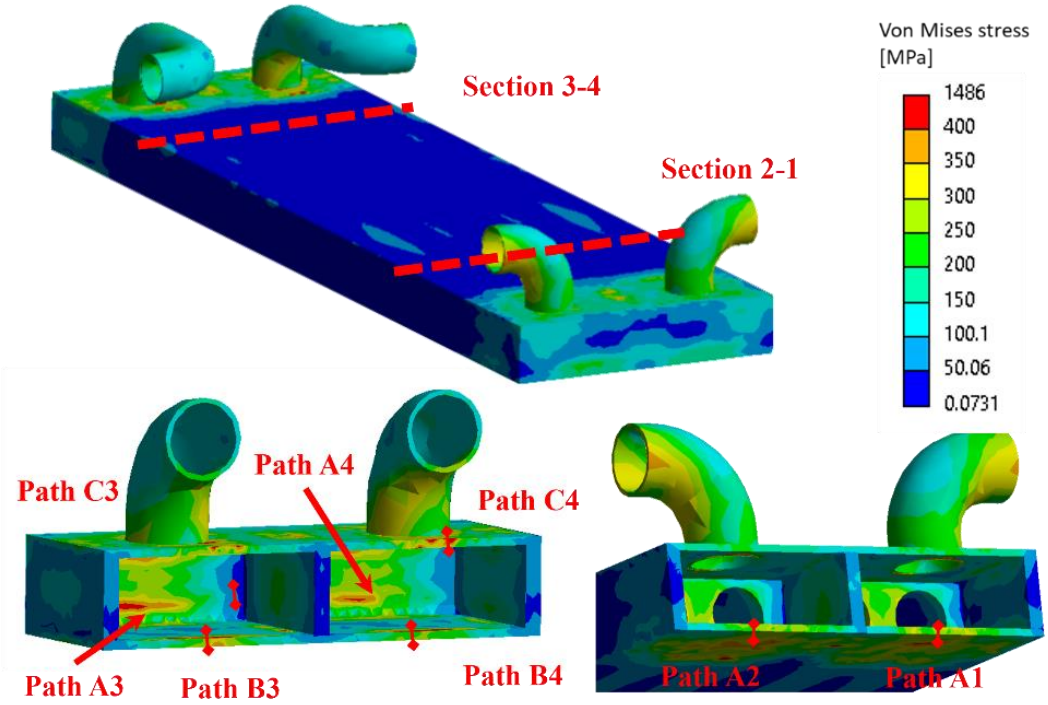

Figure 3.22 Path selected within upper NS.

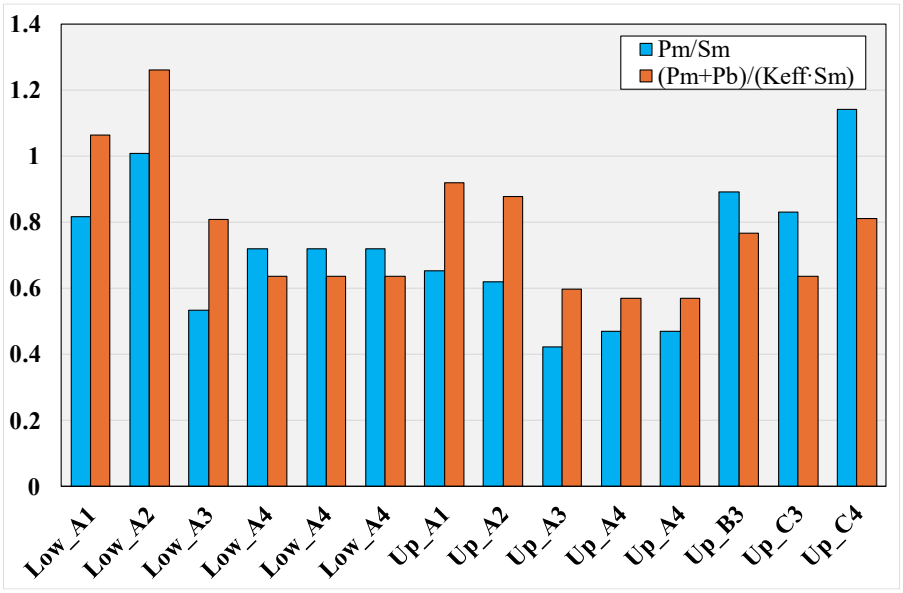

Figure 3.23 RCC-MRx criteria verification within region Y7.

Future design improvements of the CB internal geometry could be suggested and attention should be particularly paid to thin stiffening plates and some connection areas.

Finally, it is useful to remember that this activity has to be intended as a preliminary study that reproduces an overloading test scenario in which the component does not reach nominal temperatures so, a future planned activity aimed at obtaining a global thermo-mechanical response of the divertor CB should involve the study of its behaviour considering both primary and secondary loads.

3.3 Stress assessment on coating

The thermo-mechanical behaviour of Plasma Facing Materials (PFM) subjected to high heat fluxes from fusion plasma is one of the crucial issues for fusion technology.

In fusion devices, plasma-facing armours are bonded to metallic heat sinks provided with coolant channels. The thermal loads generate secondary stresses in the plasma-facing components. Moreover, the difference in the Coefficient of Thermal Expansions (CTE) of the constituting materials provokes a significant misfit stress, especially in the areas close to the interfaces between PFM and heat sink material. Of course, the thermal stress induced by the mismatch of the CTEs is controlled by the change of temperature at the interface from the stress-free state.

The mismatch stress can depend even on the manufacturing of joints resulting in residual stress within the joint. As the temperature gradient that develops in the PFM causes a further thermal stress, attention must be also paid to the influence on the temperature field of the time evolution of reactor power. The initial temperature evolution will be transient during the start-up phase, and the temperature distribution will have a sharp curvilinear shape. Once the steady state is reached, the temperature profile becomes a slope that just slightly deviates from a linear profile based on the thermal conductivity's temperature dependency. If yielding has not yet occurred, the equivalent thermal stress in the PFM progressively rises with a profile similar to that of the temperature.

Numerical methods, such as FEM analyses, are necessary for a precise assessment of the thermal stress fields of PFMs, considering the particular geometry and the realistic loads. By the way, a simplified analytical approach can still provide, at first attempt, a comprehensive vision of the thermomechanical behaviour of PFMs requiring lower computational effort. In the latter case, strong assumptions are often envisaged, regarding complicated BCs or dependence of properties from the thermal field. These aspects would be, in fact, handled with difficulties with a purely analytical approach. In this case, the focus was on the hypothesis of independence of thermomechanical properties on temperature. In particular, the thermal stress fields computed with constant properties were validated against a numerical solution enclosing temperature-dependent thermomechanical property.

For this purpose, the superposition method was adopted, according to [48], to evaluate separately the two stress contributions, i.e. the stress field due to the temperature gradient in the armour and the stress due to the CTEs mismatch.

An equivalent model to the one reported in [48] was reproduced. The purpose of this procedure is to calculate thermal stresses in PFM subjected to very high heat flux such as

divertor SL or RPs. Thus, in this work it is applied to the SL, being the component with the highest heat flux. For this reason, the geometry, the loads and the BCs were tuned to match those relevant to the DEMO divertor SL.

At first, a steady-state analytical solution of the thermomechanical problem was studied to validate the numerical method to be adopted for transient calculations. Therefore, a transient case was studied considering both an analytical solution calculated with constant properties and a numerical solution considering temperature-dependent properties.

The assessment was carried out considering both elastic and plastic regimes.

3.3.1 Description of the methodology

The model presented in this section refers to a particular temperature history of the PFM. For all the calculations, it is assumed that the components are cooled down from a stress-free temperature of 750°C to a room temperature equal to 20°C. The assumed temperature value for the stress-free state is taken from the data for a typical plasma-sprayed plasma-facing component under normal operating conditions [55]. Afterwards, they are subjected to further heat flux load (this successive load is referred to as re-heating) with increasing temperature at the bonded surface up to the steady-state value of 400°C.

The stress superposition method was applied to calculate the thermal field. To this purpose, two main contributions are considered in the analytical evaluation of the thermal stress field, expected to be generated in the actively cooled armour surface under fusion loading conditions. Considering each contribution as a separate problem with proper BCs, it is possible to adopt a more concise approach. The resultant total stress σ_1 in the PFM is given by the linear superposition of two contributions, acting separately. The two BCs representing the stress sources are:

- the temperature profile caused in the armour by the bonding constraint by the substrate, which induces the $\sigma_1^{gradient}$;
- the interface temperature T_0 which generates the $\sigma_1^{mismatch}$.

Therefore, in case of elastic regime, the total stress field on the armour can be written as the sum of the two contributions, as stated in (3.1). Please note that in the following the subscript 1 is referred to the PFM, while the subscript 2 is referred to the heat sink material.

$$\sigma_1^{total} = \sigma_1^{gradient} + \sigma_1^{mismatch} \tag{3.1}$$

Applying the strain suppression method [52], the stress field is given by (3.2), where E_1, α_1 and ν_1 are, respectively, the elastic module, Poisson's ratio and the coefficient of thermal expansion of the PFM.

$$\sigma_1^{gradient}(z,t) = -\frac{E_1\alpha_1}{1-\nu_1}\left[T(z,t) - T_0\right] \tag{3.2}$$

The solution is valid only for the bulk region distant form the side surfaces due to the principle of Saint Venant.

As far as the temperature field is concerned, it was determined from the heat equation in an analytical form in the following cases:

- Steady state regime, temperature-dependent thermodynamic properties;
- Transient regime, constant thermodynamic properties, according to [48].

The temperature field was calculated by a numerical approach in the case of transient regime considering temperature-dependent properties.

For the sake of simplicity, the following BCs were applied to the thermal problem. The top surface of the armour is heated by constant and uniform heat flux Q_0, whereas the bottom surface interfacing the structural material is at constant temperature T_0. The heat flow is one-dimensional, considering the simplified model of Figure 3.24. Therefore, the temperature and, consequently the stress field, will be only function of the vertical position z. In the real transient case, the temperature at the contact interface with the heat sink would vary, reaching a stationary value determined by the heat removal rate due to coolant.

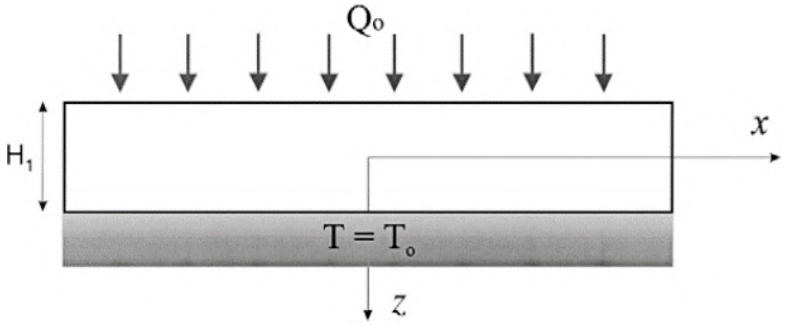

Figure 3.24 Geometry and BCs of the thermal problem.

The analytical solution for the thermal problem, valid only in case of thermal properties independent of temperature, is:

$$T(z,t) = \frac{Q_0(H_1/2 - z)}{\lambda} - \frac{8Q_0H_1}{\lambda\pi^2}\sum_{n=0}^{\infty}\frac{(-1)^n}{(2n+1)^2} \\ e^{\frac{-\kappa(2n+1)^2\pi^2}{4H_1^2}t}\sin\frac{(2n+1)\pi(H_1/2 - z)}{2H_1} + T_0 \tag{3.3}$$

where Q_0 is the heat flux at $z = -H_1/2$ and T_0 is the temperature at $z = H_1/2$, which are constant for $t > 0$. Moreover, the λ and κ are respectively the thermal conductivity and the thermal diffusivity of the armour material. Therefore, substituting the (3.3) in the (3.2) the stress field contribution related to temperature gradient will be:

$$\sigma_1^{gradient}(z,t) = -\frac{E_1\alpha_1}{1-\nu_1}\left[\frac{Q_0\left(\frac{H_1}{2} - z\right)}{\lambda} - \frac{8Q_0H_1}{\lambda\pi^2}\sum_{n=0}^{\infty}\frac{(-1)^n}{(2n+1)^2}\right. \\ \left. e^{\frac{-\kappa(2n+1)^2\pi^2}{4H_1^2}t}\sin\frac{(2n+1)\pi\left(\frac{H_1}{2} - z\right)}{2H_1}\right] \tag{3.4}$$

As clear from (3.4), the stress solution does not include anymore the T_0 which, thus, is not necessary a priori to obtain the analytical stress solution $\sigma_1^{gradient}$.

Concerning the stress contribution due to the mismatch of the CTEs of the materials, the simple analytical solution adopted is given in [48, 56] and it is based on the method of Timoshenko. It describes the thermal stress distribution along the thickness of joint materials and it is valid only for the bulk regions distant from the free surfaces edge. Therefore, in case of elastic regime, the solution of mismatch thermal stress field is described by:

$$\sigma_1^{mismatch}(\tilde{z}) = E_1^*\left[\varepsilon_0^{el} + (\alpha_1 - \alpha_2)\Delta T\right] + \frac{E_1^*\left(\tilde{z} - t_n^{el}\right)}{\rho^{el}} \tag{3.5}$$

In equation (3.5), the vertical coordinate $\tilde{z}$ has the value 0 at the interface and $\tilde{z} = H_1$ at the plasma-facing surface. The ΔT is the temperature difference from stress-free state temperature of 750°C [55] to room temperature of 20°C.

The individual parameters of (3.5) are given by:

$$\varepsilon_0^{el} = \frac{E_1^*(\alpha_1 - \alpha_2)\Delta T H_1}{2(E_1^* H_1 + E_2^* H_2)} \tag{3.6}$$

$$t_n^{el} = \frac{E_1^* H_1^2 - E_2^* H_2^2}{2(E_1^* H_1 + E_2^* H_2)} \tag{3.7}$$

$$\rho^{el} = \frac{E_1^{*2} H_1^4 + E_2^{*2} H_2^4 + 2E_1^* E_2^* H_1 H_2 (2H_1^2 + 2H_2^2 + 3H_1 H_2)}{6E_1^* E_2^* H_1 H_2 (H_1 + H_2)(\alpha_1 - \alpha_2)\Delta T} \tag{3.8}$$

where the E* is either referred to E for plane stress condition or E/(1-ν) for plane strain condition.

In case of plastic regime, the total stress field on the armour can be written as the sum of the two contributions, as in (3.1). In this case, the superposition method is again adopted for the computation of the resultant mismatch stress field which is reported in equation (3.10). In particular, considering the loading history of the PFM and under the assumption of plastic yielding suppression during re-heating, it is necessary to consider a second stress term. It develops during the reheating process and it is computed adopting the elastic solution.

$$\sigma_{1,pl}^{mismatch} = \sigma_{1,pl}^{residual} + \sigma_{1,el}^{reheating} \tag{3.9}$$

In case of partial-plastic yielding of the substrate, the residual mismatch thermal stress in the armour tile can be described by:

$$\sigma_{1,pl}^{mismatch}(\tilde{z}) = E_1^* \left[\varepsilon_0^{pl} + (\alpha_1 - \alpha_2)\Delta T_c \right] + \frac{E_1^* \left(\tilde{z} - t_n^{pl} \right)}{\rho^{pl}} \tag{3.10}$$

In case of large work hardening rate, the individual parameters are given by:

$$\varepsilon_0^{pl} = \frac{1}{2\rho^{pl}} \frac{E_1^* H_1 (H_1 + 2h_y) - E_2^* H_2 (H_2 - 2h_y)}{E_1^* H_1 + E_2^* H_2} + \frac{\sigma_y}{E_2^*} \tag{3.11}$$

$$t_n^{pl} = \frac{E_1^* H_1^2 - E_2^* H_2^2}{2(E_1^* H_1 + E_2^* H_2)} \tag{3.12}$$

$$\rho^{pl} = \frac{E_1^{*2} H_1^4 + E_2^{*2} H_2^4 + 2E_1^* E_2^* H_1 H_2 (2H_1^2 + 2H_2^2 + 3H_1 H_2)}{6E_1^* E_2^* H_1 H_2 (H_1 + H_2)(\alpha_1 - \alpha_2)\Delta T} \tag{3.13}$$

where the parameter h_y is the position of the yield front and is calculated by the equation (3.14). The yield stress σ_y is a function of temperature and it was drawn from [57].

$$h_y = \frac{\left[E_1^{*2}H_1^4 + E_2^{*2}H_2^4 + 2E_1^*E_2^*H_1H_2(2H_1^2 + 2H_2^2 + 3H_1H_2)\right]\sigma_y}{6E_1^*E_2^{*2}H_1H_2(H_1+H_2)(\alpha_1-\alpha_2)\Delta T_c} + \\ + \frac{\left[E_1^*H_1^4 + E_2^*H_2^2H_1(3H_1+4H_2)\right]}{6E_2^*H_1H_2(H_1+H_2)} \tag{3.14}$$

Moreover, the secondary mismatch term is given by:

$$\sigma_{1,el}^{reheating}(\tilde{z}) = E_1^*\left[\varepsilon_0^{el} + (\alpha_1-\alpha_2)\Delta T_h\right] + \frac{E_1^*\left(\tilde{z} - t_n^{el}\right)}{\rho^{el}} \tag{3.15}$$

where the elastic individual parameters are those of equations from (3.6) to (3.8). In this case, the temperature difference ΔT_h is considered between ambient temperature and operational temperature of 360°C, drawn from the thermal-hydraulic results of §2.5.2.

The aforementioned methodology was applied to a case study considering the material and geometry of a SL section of the DEMO divertor. Loads and BCs of the problem are detailed in Table 3.3.

Table 3.3. Summary of load and BCs.

Analysis type	Steady State/ Transient
Materials	Tungsten, Eurofer97
Temperature at interface (T_{H1})	400°C
Free-stress state temperature of armour	750°C [55]
Temperature difference on cooling (ΔT_c)	-730°C
Temperature difference on reheating (ΔT_h)	380°C
Wall Heat Flux - Liner	0.5 MW/m^2
Liner armour thickness (H_1)	2 mm
Heat sink thickness (H_2)	8 mm

The thermal stress field was investigated considering two cases with both constants and temperature-dependent material properties for tungsten to check which is the influence on the results. More in detail, the following steps were considered for the calculation of the σ_1^{total}:

- validation of the numerical method (to be adopted for the calculation of the transient solution) considering a steady-state thermal problem, carried out against a full

analytical solution. The temperature dependence of the material thermophysical properties was taken into account;

- assessment of the thermal field T(z, t): analytical in case of constant properties and numerical in case of temperature-dependence;
- analytical assessment of the stress $\sigma_1^{gradient}$ field considering both constant properties and temperature-dependent properties;
- analytical assessment of the $\sigma_1^{mismatch}$ field considering both constant properties and temperature-dependent properties in the elastic and plastic regimes.

3.3.2 Analytical models

With regard to the above-described methodology, different cases of the heat diffusion problem were considered to calculate the thermal field necessary to assess the stress distribution of the armour.

In order to determine the temperature distribution in a solid body, the energy conservation law is applied. Considering a homogeneous and isotropic medium without advection phenomena, whose temperature distribution T(*x,y,z*) is written in Cartesian coordinates, it is possible to write the heat equation as follows:

$$\rho c_p \frac{\partial T}{\partial t} = \frac{\partial}{\partial x}\left(\lambda \frac{\partial T}{\partial x}\right) + \frac{\partial}{\partial y}\left(\lambda \frac{\partial T}{\partial y}\right) + \frac{\partial}{\partial z}\left(\lambda \frac{\partial T}{\partial z}\right) + \dot{q} \tag{3.16}$$

where the time rate of change of energy per unit volume (left-hand side of (3.16)) is given by the sum of net conduction heat fluxes for each coordinate direction (evaluated from the Fourier's law) and of the volumetric heat generation $\dot{q}$. Due to the assumption of one-dimensional heat flux varying only in the z coordinate, it is possible to simplify the (3.16) as follows:

$$\rho c_p \frac{\partial T}{\partial t} = \frac{\partial}{\partial z}\left(\lambda \frac{\partial T}{\partial z}\right) + \dot{q} \tag{3.17}$$

To determine the temperature distribution T(z) as a function of time, it is necessary to solve the PDE (3.16), coupled with the pertaining BCs.

Since the heat equation is of the second order in the spatial domain, two BCs are necessary for each coordinate to properly explain the problem. However, considering that the equation is in the first order in the time domain, only one initial condition is required.

As already mentioned in § 3.3.1, two different analytical solutions were considered in this dissertation. Representative BCs to study the temperature – and the stress – field of the tungsten armour of the DEMO divertor SL were chosen. In particular, a Neumann condition at $x = 0$ and a Dirichlet condition at $z = H_1$ were applied.

At first, the thermal steady state problem was considered in order to validate the numerical method adopted in this work. Therefore, in case of the absence of a volumetric heat source and temperature distribution varying only in the vertical direction, the thermal problem considered can be written as in equations from (3.18) to (3.27).

$$\begin{cases} \dfrac{d}{dz}\left(\lambda(T)\dfrac{dT}{dz}\right) = 0 & (3.18) \\ -\lambda(T)\left.\dfrac{dT}{dz}\right|_{z=0} = q_0'' & (3.19) \\ T(z = H_1) = T_{H_1} & (3.20) \end{cases}$$

In this case, a closed analytical solution to the ordinary homogeneous differential equation can be easily found adopting the separation of variables. In order to find the solution, it is necessary to integrate the equation and find the integration constant by substituting the BCs.

It has to be pointed out that the thermal conductivity is described as a function of temperature by a fourth-degree correlation [57].

$$\lambda(T) = 164.4 - 8.522 \cdot 10^{-2} T + 5.405 \cdot 10^{-5} T^2 - 2.017 \cdot 10^{-8} T^3 + 3.032 \cdot 10^{-12} T^4 \quad (3.21)$$

For the sake of simplicity, the correlation was considered as linear with temperature (see equation (3.22)) with a maximum relative error of about 1% on a wide temperature range considered in this problem, being 300°C – 1000°C. Therefore, the solutions for the problem are given by equation (3.23), where the coefficient $\omega(z)$ is reported in equation (3.24).

$$\lambda(T) = a + bT \quad (3.22)$$

$$T_{1,2}(z) = \frac{-a \pm \sqrt{a^2 + 2b\omega(z)}}{b} \tag{3.23}$$

$$\omega(z) = \frac{b}{2} T_{H_1}^2 + aT_{H_1} + q_0^{"}\left(\frac{H_1}{2} - z\right) \tag{3.24}$$

The steady-state thermal analytical solution was adopted to calculate the $\sigma_1^{gradient}$ and compare it with the respective $\sigma_1^{gradient}$, calculated using the steady-state thermal numerical solution aiming at validating the numerical method adopted.

The second analytical solution considered in this work is relevant to the transient problem presented in equations from (3.25) to (3.28).

In this case, constant thermodynamic properties were considered and the pertaining solution was found according to [50] and already reported in equation (3.3)

$$\begin{cases} \rho c_p \dfrac{\partial T(z,t)}{\partial t} = \lambda \dfrac{\partial^2 T(z,t)}{\partial z^2} & (3.25) \\ -\lambda \left.\dfrac{dT}{dz}\right|_{z=0} = q_0^{"} & (3.26) \\ T(z = H_1) = T_{H_1} & (3.27) \\ T(z = 0) = T_{in} & (3.28) \end{cases}$$

The $\sigma_1^{gradient}$ was then calculated using the analytical solution of the mentioned transient problem, as reported in §3.3.1, equation (3.4). The same quantity was then compared with the one calculated adopting a numerical thermal solution of the same problem, considering instead the temperature-dependent properties, obtained solving the following equations.

$$\begin{cases} \rho(T) c_p(T) \dfrac{\partial T(z,t)}{\partial t} = \dfrac{\partial}{\partial z}\left(\lambda(T) \dfrac{\partial T(z,t)}{\partial z}\right) & (3.29) \\ -\lambda(T) \left.\dfrac{dT}{dz}\right|_{z=0} = q_0^{"} & (3.30) \\ T(z = H_1) = T_{H_1} & (3.31) \\ T(z = 0) = T_{in} & (3.32) \end{cases}$$

The objective of this comparison was to check whether the adoption of constant or T-dependent properties would affect the results in terms of stress field.

The thermodynamic properties adopted to calculate the temperature profile and perform the steady-state calculations and the transient numerical calculation were drawn from the correlations shown in [57]. They are the conductivity λ(T), already reported in equation

(3.22), the mass density $\rho(T)$ and the specific heat capacity $c_p(T)$ reported below, where ρ_{ref} is the reference mass density at the reference temperature T_{ref}=25°C, equal to $1.928 \cdot 10^4$ kg/m^3.

$$\rho(T) = \frac{\rho_{ref}}{1 + 3\alpha_{ave}(T)(T - T_{ref})} \tag{3.33}$$

$$\alpha_{ave}(T) = (4.401 + 5.991 \cdot 10^{-5} T + 2.374 \cdot 10^{-7} T^2) \cdot 10^{-6} \tag{3.34}$$

$$c_p(T) = 1.387 \cdot 10^2 + 9.747 \cdot 10^{-3} T + 4.671 \cdot 10^{-6} T^2 \tag{3.35}$$

As already done for the conductivity, for the sake of simplicity, the correlations for the mass density and the specific heat capacity were approximated with linear functions of temperature (same form of equation (3.22)). In these cases, maximum relative errors lower than 0.5% were encountered in the wide temperature range considered, between 300°C – 1000°C.

Concerning the thermomechanical properties, being Young's modulus E_i, Poisson's ratio ν_i and the coefficient of thermal expansion α_i (3.34), they were drawn from [57] for tungsten and depicted below. Considering the heat sink in Eurofer97, the thermomechanical properties i.e. E_2, α_2 and ν_2, at the temperature of 400°C were drawn from [36].

$$E_1(T) = 3.961 \cdot 10^2 - 5.893 \cdot 10^{-3} T - 2.752 \cdot 10^{-5} T^2 \tag{3.36}$$

$$\nu_1(T) = 0.28005 + 5.744 \cdot 10^{-6} T + 5.40 \cdot 10^{-9} T^2 \tag{3.37}$$

For the analytical solution, the constant values of the properties at the initial temperature of 400°C were considered.

3.3.3 Numerical models

The numerical results were obtained with a calculation tool executed in the MATLAB environment. The differential equations presented in this section were numerically solved using the MATLAB *pdepe* solver, based on the numerical differentiation formulas of orders 1 to 5 [58].

To solve the PDEs in MATLAB, it is needed to code the equation, writing it as a function in a form that the *pdepe* solver expects. Then, to properly define the problem, the initial

conditions and the BCs shall be written as functions considering the standard form expected by the code.

Two differential equations were coded and solved adopting the *pdepe* solver. The first one is equation (3.18), with the relevant BCs (equations (3.19) and (3.20)) and it is relevant to the steady-state problem.

The second thermal problem solved is the transient thermal problem of equations (3.25) to (3.28). However, in the numerical resolution, thermodynamic properties linearly dependent on temperature were adopted.

The steady-state thermal diffusion problem, reported in equations from (3.18) to (3.20), and the transient thermal diffusion problem of equations from (3.30) to (3.37) were numerically solved adopting the *pdepe* solver.

Finally, before calling the *pdepe* solver it is necessary to select a suitable spatial discretization, specified as a vector which includes the points at which the *pdepe* will evaluate the solution. In this case, for both problems, a vector of 100 points was created along the z direction of the armour thickness.

3.3.4 Results

As mentioned above, this activity started with the validation of the numerical algorithm set up to get the transient solution to the heat equation with temperature dependent coefficients. Therefore, the analytical solutions shown in the previous paragraph were compared with the numerical ones, in the case of steady-state regime with varying coefficients and in the transient case with constant coefficients, using data reported in Table 3.3.

As far as the first case is concerned, Figure 3.25 shows both the analytical and the numerical profiles as functions of the distance from the plasma facing surface, which is the heated surface, adopting an abscissa normalized with respect to the armour thickness.

As it can be argued from Figure 3.25, the numerical temperature profile perfectly matches the numerical profile with errors approaching zero. Then, the numerical method was fully validated and adopted for the transient calculation to compare the effect of adopting constant thermomechanical properties or temperature-dependent thermomechanical properties on the stress results.

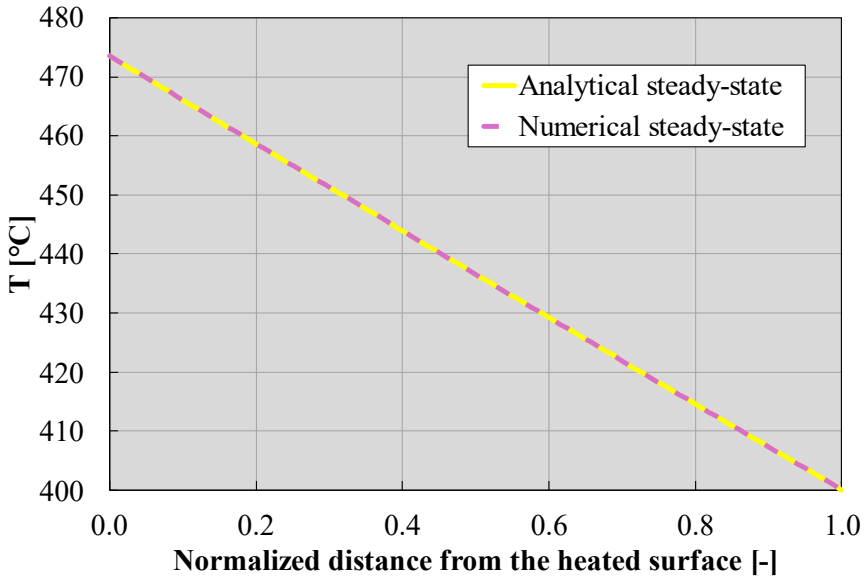

Figure 3.25 Steady-state temperature profiles, temperature-dependent coefficients.

In Figure 3.26 the transient temperature profiles are reported for both analytical (3.3) and numerical solutions. In particular, case "1" refers to the thermal field calculated with the numerical algorithm and the temperature-dependent properties, while case "2" refers to the analytical solution of the thermal field (equation (3.3)) calculated with constant properties. The temperature profiles at the steady state were reported (t=10s), along with the profiles at two different time points, respectively t=0.01s and t=0.05s.

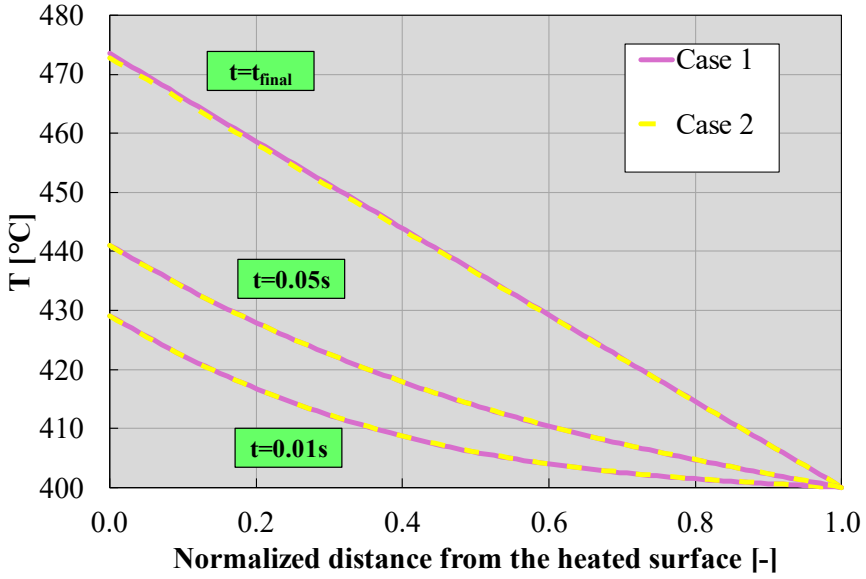

Figure 3.26 Temperature profiles at three different instants.

As can be noticed from the results, the temperature profiles match at every instant of time. It is worth highlighting how, despite the differences between the constant and temperature-

dependent thermodynamic properties in the two calculations, the profiles stay in perfect agreement with each other. Maximum relative errors between the two cases, for each time instant, are in the order of 0.2%.

The temperature profiles shown in Figure 3.25 and Figure 3.26 were adopted to calculate the respective stress term due to the temperature gradient (see equation (3.2)) and to their influence on the properties adopted.

It is interesting to investigate the behaviour of the gradient tension, taking into account that the involved mechanical quantities (Young's modulus, Poisson's modulus and the coefficient of thermal expansion) vary with temperature. Before treating this problem comprehensively with a numerical approach, it is useful to outline a first, simple analytical method to better decipher the underlying phenomenology.

For this reason, the stationary case is considered for which the following formula applies:

$$\sigma(T) = -\frac{E(T)\alpha(T)}{1-\nu(T)}\left(T - T_0\right) \tag{3.38}$$

The functional form of every quantity of equation (3.38) is reported in §3.3.2. It is clear that the function F(T), given by

$$F(T) = \frac{E(T)\alpha(T)}{1-\nu(T)} \tag{3.39}$$

is crucial for the task. This function varies very slowly with temperature and in fact in the range of interest, between $T_{min}=T_0=300°C$ and $T_{Max}=370°C$, its maximum value (at 337°C) is only 0.0017% higher than the smallest value which is at T_0. It can be deduced that the variation of mechanical quantities with temperature can be considered negligible and that therefore the tension is a linear function of temperature.

It is observed, then, that it is permissible to express the tension by its development in Taylor series arrested at the first term:

$$\sigma(T) \cong \sigma(T^*) + \left.\frac{d\sigma(T)}{dT}\right|_{T^*}\left(T - T^*\right) \tag{3.40}$$

Then, it is found that the percentage variation of tension with temperature can be expressed as follows:

$$\frac{\sigma(T)-\sigma(T^*)}{\sigma(T^*)}=\frac{1}{\sigma(T^*)}\frac{d\sigma(T)}{dT}\bigg|_{T^*}\left(T-T^*\right) \tag{3.41}$$

In particular, the quantity

$$\frac{1}{\sigma(T^*)}\frac{d\sigma(T)}{dT}\bigg|_{T^*} \tag{3.42}$$

is small (in the order of ~10^{-2}) in the temperature range considered and it is a decreasing function of T*. It follows that the higher the temperatures involved, the less the tension changes with temperature.

What has been observed with this simplified analytical approach is confirmed by numerical results under stationary and transient conditions. The steady-state cases with varying coefficients were reported in Figure 3.27.

As expected, the two profiles match each other with negligible errors. As expected, they are proportional to the temperature behaviour of Figure 3.25.

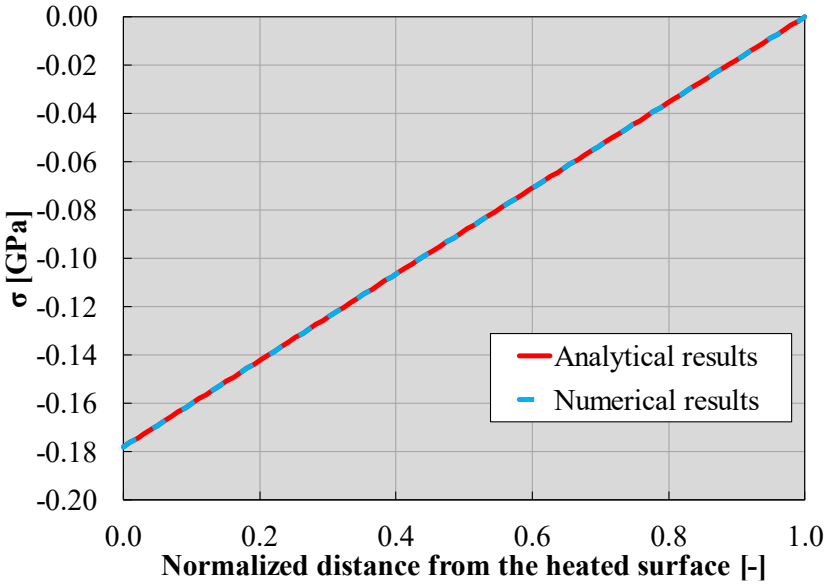

Figure 3.27 Steady-state stress field due to temperature gradient.

Analogous consideration can be done for the transient cases, shown in Figure 3.28. In particular, both cases were reported, being case “1” the stress field calculated with the numerical thermal field and the temperature-dependent properties, and case “2” the stress field calculated with the analytical thermal field of equation (3.3) and constant properties.

Both cases are reported in figure for two different times, respectively at t=0.01s and t=0.05s, along with their relevant stationary solutions ($t=t_{final}=10s$).

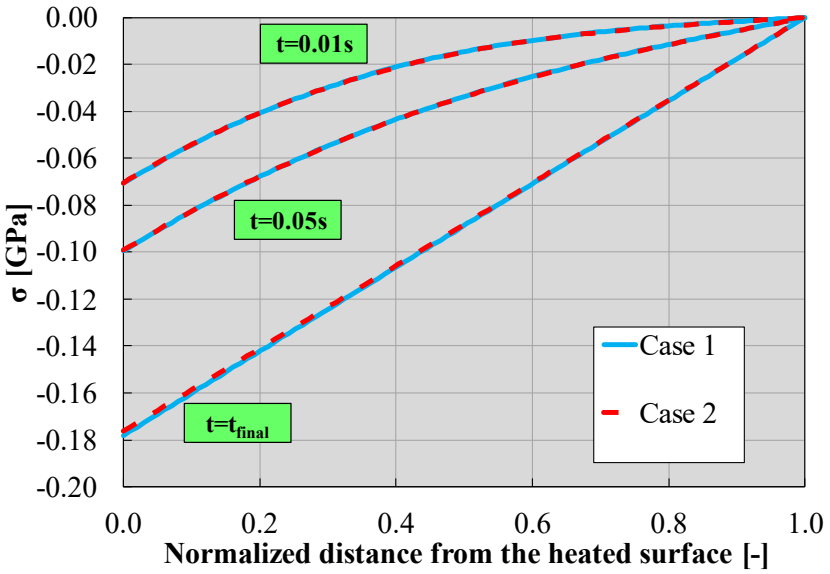

Figure 3.28 Stress profiles due to temperature gradient at different instants.

As it can be noticed from the results, the temperature profiles match at every instant of time. It is worth highlighting how, despite the differences between the constant and temperature-dependent thermodynamic properties in the two calculations, the profiles match at each time. Maximum relative error between the two cases, for each time instant (0.01s, 0.05s and 10s), are respectively 2.7%, 0.7% and 0.9%. It has to be pointed out that the higher error shown at the first instant of time (0.01s) occurs at the interface where stress values approach zero due to the full constraint with the heat sink.

The results relative to the stress contribution due to the CTEs difference, referred to as mismatch stress, were evaluated for elastic regime, as in equation (3.5) and plastic regime (equation (3.10)) and reported in the following. In this case, the tensions were reported as functions of the distance from the interface between the two materials. This distance was normalized with respect to the armour thickness.

Starting from the elastic case, for the sake of completeness, the steady-state analytical (constant properties)-numerical (varying coefficients) comparison is depicted in Figure 3.29.

The numerical stress results are qualitatively the same of the analytical ones with errors close to zero. In fact, the mismatch tension profile depends only on the individual parameters varying with temperature. Then, the profiles totally reflect the steady-state temperature profiles of Figure 3.25.

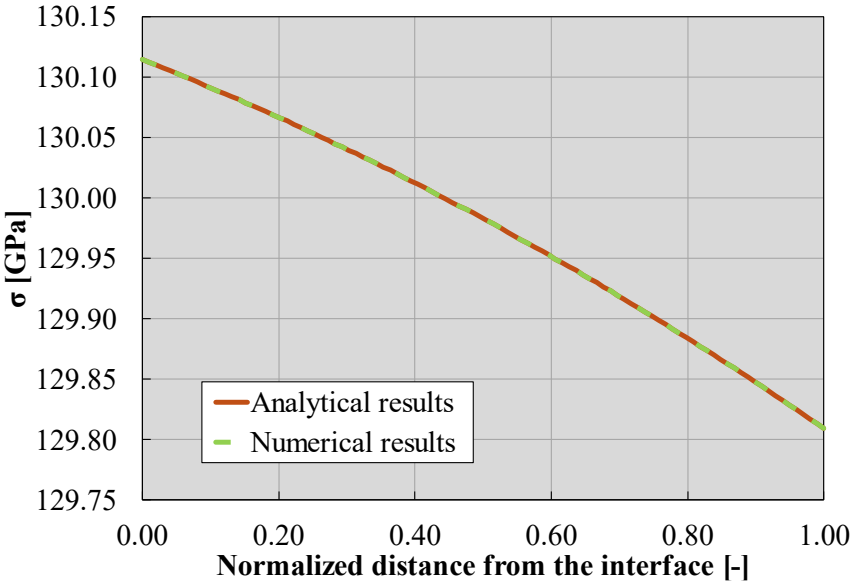

Figure 3.29 Steady-state stress profiles due to CTEs mismatch (elastic regime).

The elastic mismatch tension profiles calculated for the case "1" and "2" are reported in Figure 3.30. Unlike as it was done previously for the gradient stress contribution, for case "1", the results at each time are depicted in the graph. Instead, for case "2" only the stationary results are shown. Indeed, looking at equation (3.5), it has to be noticed that, case "1" provides a stress solution which depends on the transient thermal field only through the thermomechanical properties varying with temperature. On the contrary, the same cannot be affirmed about the case "2", where the equation (3.5) is a function only of the spatial coordinate. In this case, the time-dependent thermal field does not influence the case "2" results, because they are computed with constant thermomechanical properties and no other temperature variations are included in the equation (3.5).

Looking at Figure 3.30, the mismatch stress value differences are higher going from the interface (where the difference is low) to the plasma-facing surface. The reason is that the thermomechanical properties for case "1" are calculated as functions of the thermal field, which varies with the spatial temperature distribution. Instead, for case "2" the constant properties are evaluated at 400°C (which is the interface temperature).

However, despite the difference discussed, the maximum relative error at the plasma-facing surface between the two stationary results (green and dark red curve) is around 0.5%.

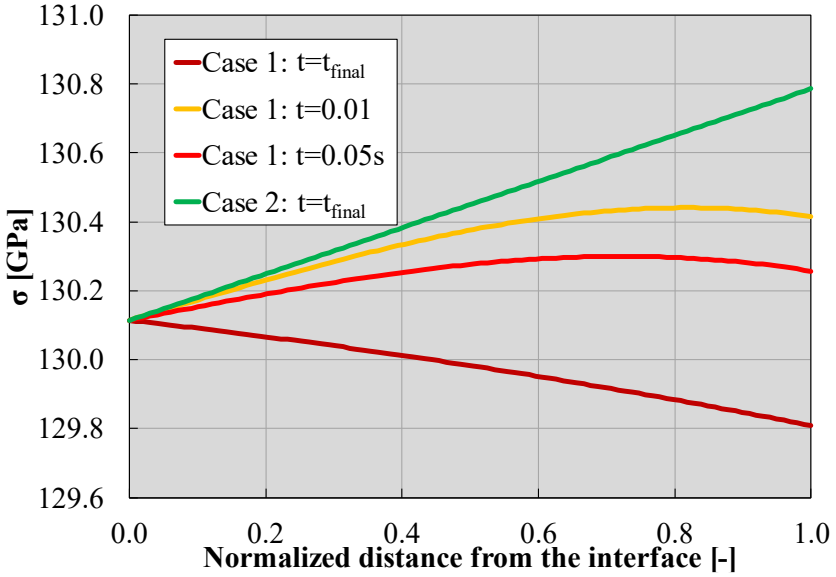

Figure 3.30 Stress profiles due to CTEs mismatch (elastic regime) at different instants.

Considering the plastic regime, for the sake of completeness, the steady-state analytical-numerical comparison is reported in Figure 3.31. The numerical and analytical results coincide perfectly, with the relative error being close to zero. In fact, the mismatch tension profile depends only on the individual parameters varying with temperature. Then, the profiles totally reflect the steady-state temperature profiles of Figure 3.25. Moreover, the profiles are analogous to those of Figure 3.29. In fact, looking at equation (3.10), the only difference from the elastic case is given only by the formulation of the individual parameter ε_0^{pl} (equation (3.11)).

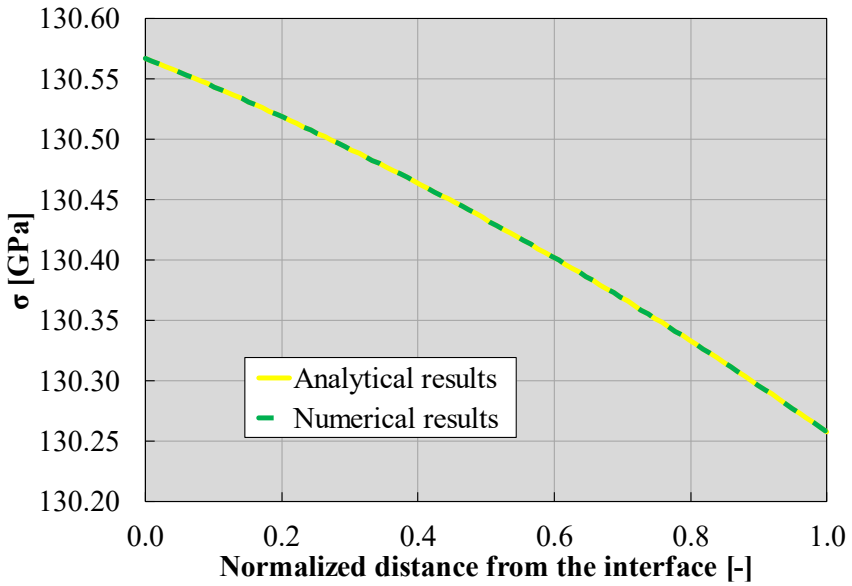

Figure 3.31 Steady-state stress fields due to CTEs mismatch (plastic regime).

The plastic mismatch tension profiles calculated for the case "1" and "2" are reported in Figure 3.32. As previously done for the elastic case and for the same reason, for case "1", the results at each time step are depicted in the graph. Instead, for case "2" only the stationary results are shown.

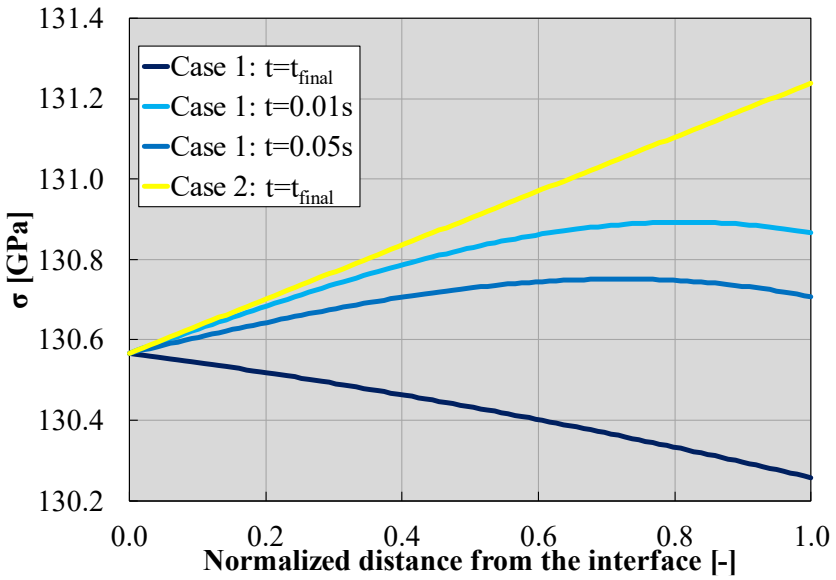

Figure 3.32 Stress fields due to CTEs mismatch (plastic regime).

Looking at stationary results in Figure 3.32, the mismatch stress value differences are higher going from the interface (where the difference is low) to the plasma-facing surface. Once again, the reason is that the thermomechanical properties for case "1" are calculated as functions of the thermal field, which varies with the spatial temperature distribution. Instead, for case "2" the constant properties are evaluated at 400°C (which is the interface temperature).

However, despite the difference, the maximum relative at the plasma-facing surface between the two stationary results (yellow and dark blue curves) is around 0.5%.

The stationary profiles of the mismatch stress term, for both elastic and plastic regimes are reported in Figure 3.24.

As may be noticed from the graph, the results in the two regimes are analogous with lower values in case of elastic regime. The two couples of curves are respectively shifted by about 0.5GPa, corresponding to a relative difference of 0.4%. This can be confirmed by looking at the equations (3.10). In fact, as already mentioned, the difference between the plastic mismatch stress and the elastic mismatch stress is given by the difference $\varepsilon_0^{pl} - \varepsilon_0^{el}$.

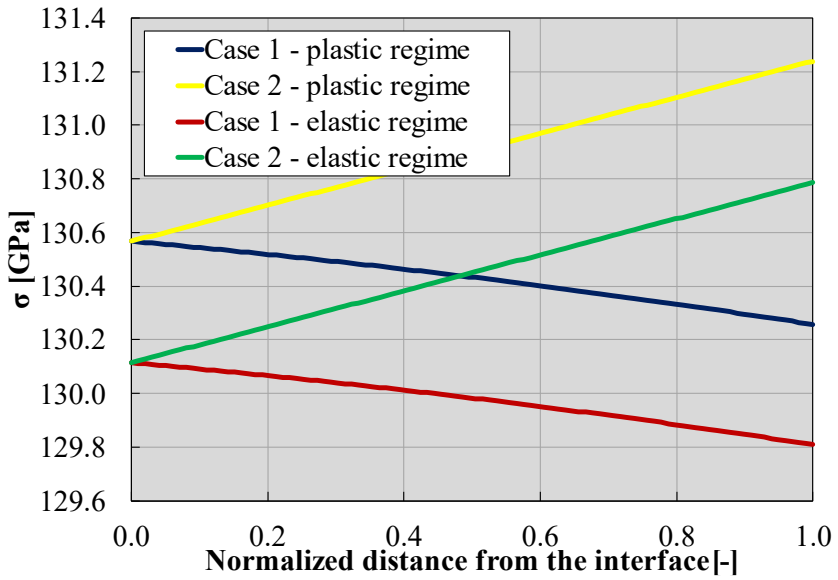

Figure 3.33 Stress fields due to CTEs mismatch.

Finally, the thermal stress field due to the reheating of the joints from room temperature to the operational temperature is reported in Figure 3.34. In particular the results at the three considered times of Case "1" are compared to the results of Case "2".

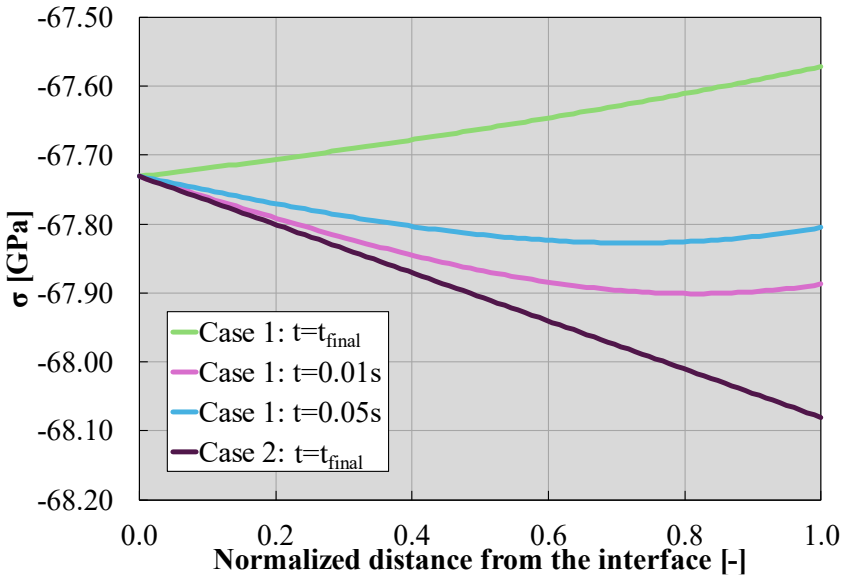

Figure 3.34 Re-heating stress fields.

Looking at the results, it can be noticed that the thermal stress has a compressive behaviour in case of reheating the structure from the room temperature to the operational temperature. The maximum value of thermal stress due to reheating is localized at the heating surface, where, moreover, the two stationary results are more distant. However,

despite the differences, the maximum relative error at the plasma-facing surface between the two stationary results (green and dark purple curves) is less than 0.5%.

3.4 Conclusions

In this section two peculiar aspects of the thermomechanical performances of the DEMO divertor were thoroughly examined and discussed. Extreme mechanical and thermal loads act on the entire DEMO divertor, generating stresses in its internal and external structural components. For the design of the component, a comprehensive understanding of its response under such conditions is deemed necessary. The study comprised two parallel investigations, each focusing on distinct aspects of the divertor's behaviour.

The first one is the study of the thermomechanical behaviour of the CB structure subjected to the high coolant pressure due to the novel divertor operating conditions (inlet pressure of 15.5 MPa and inlet temperature of 295°C). In this regard, the CB structural response under the load combination foreseen for a typical PT scenario was assessed. Attention was directed towards analysing the equivalent stress and displacement fields, along with verifying the fulfilment of the pertinent RCC-MRx structural design criteria.

Considering the whole CB structure including its inboard and outboard regions, the selected criteria are not satisfied, with some exceptions. This behaviour could be a combined effect of the small thickness of the CB stiffening plates subjected to the high pressure and the CB constraints. For what concerns the NS structure, results showed that almost all the paths fulfil the selected criteria. However, some paths reach high values of the same criterion without overcoming the limit.

Future design improvements of the CB internal geometry could be suggested by paying the attention to thin stiffening plates and internal ribs, increasing their thickness, where necessary. Moreover, it is important to note that this preliminary study replicates an overloading test scenario, during which the component does not reach nominal temperatures. Therefore, a comprehensive assessment considering both primary and secondary loads will be crucial for obtaining a more holistic understanding of the divertor CB's thermomechanical response. This further development will provide essential insights for refining design strategies and ensuring the component's resistance under real operating conditions.

As a complementary aspect of the thermomechanical assessment of the DEMO divertor, the structural behaviour of the plasma-facing surfaces was investigated. A theoretical-

numerical assessment of the thermal stresses on a typical tungsten armour was carried out to check whether a simplified analytical approach would be capable of reproducing a comprehensive thermal stress response of a plasma-facing component, with less computational effort with respect to detailed numerical calculations. In particular, the aim was to assess the influence of temperature-dependent thermomechanical properties on the results.

At first, the numerical approach adopted for the temperature profile and for the consequent thermal stress calculations was validated through an analytical solution, for a steady-state scenario. Therefore, a transient problem was studied considering both cases with constant and temperature-dependent properties. In particular, the numerical results in terms of thermal stress on the armour were obtained in MATLAB environment considering temperature-dependent thermomechanical properties. These numerical outcomes were compared with the analytical results calculated with constant properties.

The superposition stress method was employed to calculate the thermal stress contributions. In particular, the contribution due to the temperature gradient experienced by the armour and the one due to the difference in CTEs of the armour and heat sink materials were considered. Results show that the numerical thermal stresses profile matches the numerical profile with negligible errors. Then, the numerical method was fully validated and adopted for the transient calculation to evaluate the effect of adopting constant thermomechanical properties or temperature-dependent thermomechanical properties on the stress results. Comparison between calculations of gradient stress field and mismatch stress field, computed in case of constant (case “2”) and temperature-dependent thermomechanical properties (case “1”), showed negligible difference (lower than 1%).

Then, it is possible to conclude that, in the range of temperature in which the divertor works, the influence of the variation of the mechanical properties with temperature is negligible on the assessment of the secondary stress field in the armour.

Moreover, simulations seem to show that the simplified method herewith presented is able to cope with the study of the thermal stress field in the divertor plasma facing components could be a fast and enough reliable approach to be used in this context which deserves further development to be definitively validated by focused campaign of analyses to be carried on with thermomechanical codes.

Conclusions

The research activity carried out during the XXXVI cycle of Ph.D. course in Energy – curriculum Low-carbon Energetics and Innovative Nuclear Systems –held at the Department of Engineering (DI) of the University of Palermo has been framed within the design studies on the DEMO nuclear fusion reactor.

The central core of the work was the study of some important aspects of the thermal-hydraulic and thermomechanical performances of DEMO divertor double-circuit cooling option. The aim was to identify the strengths and limitations of the models, giving important indications of the component behaviour under high heat loads.

Coupled solid-fluid thermofluid-dynamic analyses of the entire divertor assembly were carried out by adopting a proper nuclear heating map. The objective of the work was the assessment of the circuit cooling capabilities and its thermal behaviour, to highlight the possible occurrence of hot spots and potential water vaporization issues. Moreover, in order to extend the life of the component, alternative materials to Eurofer97 were investigated for the TBs of the PFC cooling circuit, i.e. CuCrZr and SS 316 Ti. Then, the structural temperature distributions in all three cases were studied and compared.

As far as the thermal-hydraulic study is concerned, the research campaign was carried out following a theoretical-computational approach based on the FVM and adopting the commercial CFD code ANSYS CFX and the simulations run on the CRESCO ENEAGRID HPC systems.

The hydraulic behaviour in terms of pressure drops and velocity distributions can be considered acceptable, respecting most of the constraints. Some exceptions were encountered in the RPs plasma-facing and back channels where the velocity distribution is highly uneven, thus posing the requirement of a design review of the cooling circuit.

As for the thermal fields, some potential critical points were identified that will require design modifications or specific treatments to ensure the component’s safety and reliability in the intended operating environment. It was noticed that temperatures in PFC structures reach extremely high values on the TBs and on their supports, especially for the case with TBs in SS 316 Ti and Eurofer97. Analogous problems are highlighted in the CB cooling

circuit structure. Temperatures higher than 550°C are reached in some regions of the SL, RPs and their supports and in some inboard corners of the CB, requiring several changes in the design of the cassette.

Regarding the thermomechanical study, it was focused on the performances of the DEMO divertor CB, subjected to high mechanical and thermal stresses. Through the execution of two parallel studies, this research attempt examines the CB's response to the novel operating conditions.

The initial study focused on the mechanical behaviour of the CB structure under the elevated coolant pressure of the divertor operating regime. Specifically, the structural integrity of the CB was assessed under the anticipated load combination for a typical pressure test scenario. This study placed particular emphasis on evaluating the equivalent stress and displacement fields. Moreover, it was verified whether the model meets the RCC-MRx structural design criteria. The research campaign was conducted following a theoretical-computational approach based on the FEM and adopting a suitable release of the commercial code ANSYS Mechanical.

Results showed that the structural design criteria are not entirely met across the CB structure, including both its inboard and outboard regions, albeit with some exceptions like the NSs, where the criteria are mostly verified. This may be attributed to the small thickness of CB stiffening plates subjected to high pressure. To address the identified shortcomings and strengthen the structural integrity of the CB, future design improvements are recommended. Particular attention is directed towards internal ribs and connection areas, increasing their thickness where necessary. It is mandatory to acknowledge that this preliminary study replicates an overloading test scenario wherein the component does not attain nominal temperatures. Consequently, a forthcoming research effort is necessary to obtain a comprehensive thermo-mechanical response of the divertor CB, considering both primary and secondary loads.

In parallel with the mechanical assessment of the DEMO divertor CB, a complementary investigation was undertaken to probe the structural behaviour of plasma-facing surfaces. These critical components are subjected to intense thermal and particle fluxes and are envisaged to be coated with a thin layer of Tungsten for the DEMO divertor. Within this framework, a theoretical-numerical assessment of the thermal stresses on a typical Tungsten armour was conducted to ascertain the feasibility of employing a simplified analytical approach in replicating the comprehensive thermal stress response of a plasma-facing component. The research campaign was carried out following a theoretical-numerical approach, developed in the MATLAB environment.

After validating the numerical approach against analytical solutions for a steady-state scenario, a transient problem, encompassing both scenarios with constant and temperature-dependent properties, was explored. Notably, the numerical results pertaining to thermal stress on the armour, obtained with a numerical tool and considering temperature-dependent properties, were compared against analytical results computed under the assumption of constant thermomechanical properties. The analysis showed that the analytical thermal stress profile closely aligns with the numerical profile, with errors approaching negligible levels, although the assumption of adopting constant properties.

The present study showed some insights related to the thermomechanical and thermal-hydraulic dynamics governing the behaviour of the DEMO divertor and plasma-facing components. These findings are important for potential future investigations aimed at reinforcing the structural integrity and the cooling capabilities and then, optimizing the divertor design.

References

[1] International Energy Agency, ‘World Energy Outlook 2023’, 2023.

[2] United Nations, ‘Trasforming our world: The 2030 Agenda for Sustainable Development’, 2015.

[3] T. Donné and W. Morris, *European Research Roadmap to the Realisation of Fusion Energy*. EUROfusion: Munich, Germany, 2018.

[4] F. Romanelli and others, *A Roadmap to the Realisation of Fusion Energy*. 2012.

[5] J. R. Lamarsh, *Introduction to Nuclear Reactor Theory*. New York.

[6] A. A. Harms, K. F. Schoepf, and D. R. Kingdon, *Principles of Fusion Energy: An Introduction to Fusion Energy for Students of Science and Engineering*. in Principles of Fusion Energy: An Introduction to Fusion Energy for Students of Science and Engineering. World Scientific, 2000.

[7] G. Federici, L. Boccaccini, F. Cismondi, M. Gasparotto, Y. Poitevin, and I. Ricapito, ‘An overview of the EU breeding blanket design strategy as an integral part of the DEMO design effort’, *Fusion Engineering and Design*, vol. 141, pp. 30–42, 2019, doi: https://doi.org/10.1016/j.fusengdes.2019.01.141.

[8] G. Federici and A. J. H. Donné, ‘Introduction’, *Fusion Engineering and Design*, vol. 178, p. 113102, 2022, doi: https://doi.org/10.1016/j.fusengdes.2022.113102.

[9] C. Bachmann, *PDD - Plant Description Document*. EUROfusion: Munich, Germany, 2020.

[10] J.H. You and others, ‘Divertor of the European DEMO: Engineering and technologies for power exhaust’, *Fusion Engineering and Design*, vol. 175, p. 113010, 2022, doi: https://doi.org/10.1016/j.fusengdes.2022.113010.

[11] T. Dolan, *Fusion Research: Principles, Experiments and Technology*. New York:Pergamon Press, 1982.

[12] H. Reimerdes *et al.*, ‘Assessment of alternative divertor configurations as an exhaust solution for DEMO’, *Nuclear Fusion*, vol. 60, no. 6, p. 66030, May 2020, doi: 10.1088/1741-4326/ab8a6a.

[13] G. Mazzone, J. H. You, and E. Visca, ‘DEMO of the European DEMO: Overview of DEMO Divertor Architecture Design Options (2014-2022))’, *IAEA Headquarters - 4th Technical Meeting on Divertor Concepts*, 2022.

[14] G. Mazzone and et al., ‘Eurofusion-DEMO Divertor - Cassette Design and Integration’, *Fusion Engineering and Design*, vol. 157, p. 111656, 2020, doi: 10.1016/j.fusengdes.2020.111656.

[15] G. Mazzone, ‘Divertor cassette Design Description Document 2017’, 2017.

[16] D. Marzullo, *DIV-1-T007-D004 - CAD Design - 2020*. EUROfusion: Munich, Germany, 2021.

[17] D. Marzullo, V. Imbriani, and F. Giovanna, *DIV-DEMO.S.1-T001-D001_DEMO Divertor CAD model 2021*. EUROfusion: Munich, Germany, 2021.

[18] D. Marzullo, *DIV-DEMO.S.1-T010-D001DEMO Divertor CAD model 2022_ENEA*. EUROfusion: Munich, Germany, 2022.

[19] D. Marzullo, *DEMO_DIVERTOR_2019*. EUROfusion: Munich, Germany, 2019.

[20] P.A. Di Maio, *DIV-DEMO.S.1-T002-D001_Divertor Thermo-hydraulic assessment 2021*. EUROfusion: Munich, Germany, 2022.

[21] P.A. Di Maio and others, ‘Thermal-hydraulic study of the DEMO divertor cassette body cooling circuit equipped with a liner and two reflector plates’, *Fusion Engineering and Design*, vol. 167, p. 112227, 2021, doi: https://doi.org/10.1016/j.fusengdes.2021.112227.

[22] D. Stork, *1. WPDIV PCD Final Review Panel Report*. EUROfusion: Munich, Germany, 2020.

[23] P. Frosi, ‘Loads Specification (LS) for Divertor Assembly 2020 (incl. neutronic analysis and structural integrity report)’, 2020.

[24] D. Marzullo, ‘DEMO Divertor Design Description Document (DDD) 2022’, 2022.

[25] E. Gaganidze and others, *DEMO-DEF-1-CD1 - Materials Properties Handbook - CuCrZr*. EUROfusion: Munich, Germany, 2020.

[26] A. Quartararo *et al.*, ‘Thermofluid-dynamic assessment of the EU-DEMO divertor single-circuit cooling option’, *Fusion Engineering and Design*, vol. 188, p. 113408, 2023, doi: https://doi.org/10.1016/j.fusengdes.2022.113408.

[27] V. Imbriani, ‘WP-DIV Demo Divertor 2022 -CAD Model - two cooling options with cassette cooled with water at high pressure and temperature’, 2022.

[28] A. Quartararo, P. A. Di Maio, and E. Vallone, ‘ADRANOS: A numerical tool developed to analyse coolant operating conditions of the EU-DEMO divertor’, *Fusion Engineering and Design*, vol. 197, p. 114055, 2023, doi: https://doi.org/10.1016/j.fusengdes.2023.114055.

[29] P. A. Di Maio, ‘DIV-DEMO.S.1-T011-D001_DEMO Divertor Thermo-hydraulic assessment 2022_ENEA, Eurofusion Report 2Q47U2 v1.0’, 2023.

[30] A. Quartararo *et al.*, ‘Thermofluid-dynamic assessment of the EU-DEMO divertor single-circuit cooling option’, *Fusion Engineering and Design*, vol. 188, p. 113408, Mar. 2023, doi: 10.1016/J.FUSENGDES.2022.113408.

[31] G. Mazzone, ‘Personal Communication’, 2023.

[32] A. Quartararo *et al.*, 'Hypothetical porous medium concept as a virtual swirl tape: A novel modelling technique towards efficient CFD simulation of swirl tape cooling pipe', *Fusion Engineering and Design*, vol. 200, p. 114240, 2024, doi: https://doi.org/10.1016/j.fusengdes.2024.114240.

[33]'https://www.afs.enea.it/project/eneagrid/Resources_en/CRESCO_documents/index.html'.

[34] D. Marzullo, 'DIV-JUS-2-CD1: Divertor System Detailed Design Description, Eurofusion Report 2NSLJP v1.4', 2020.

[35] International Association for the Properties of Water and Steam, *Revised Release on the IAPWS Industrial Formulation 1997 for the Thermodynamic Properties of Water and Steam*. 2007.

[36] E. Gaganidze, 'DEMO-DEF-1-CD1 - Materials Properties Handbook - EUROFER97, Eurofusion Report 2NZHBS v1.3', 2023.

[37] E. Gaganidze, 'DEMO-DEF-1-CD1 - Materials Properties Handbook - CuCrZr, Eurofusion Report 2NV3Q6 v1.0', 2020.

[38] ITER Organization, 'ITER SDC-IC Appendix A Materials Design Limit Data', 2013.

[39] ITER Organization, *ITER Material Properties Handbook, ITER Document No. G74 MA 16*.

[40] The American Society of Mechanical Engineers, 'Boiler and pressure vessel code, Section II - Part D', *The American Society of Mechanical Engineers*, 2015.

[41] C. Bachmann, 'PDD - Plant Description Document, Eurofusion Report 2KVWQZ v1.9', 2020.

[42] R. Villari, 'DIV-DEMO.S.1-T012-D001_Neutronics and shielding assessment report 2022_ENEA, Eurofusion Report 2Q45X4 v1.0', 2023.

[43] R. Villari, 'DIV-DEMO.S.1-T022-D001_Neutronics and shielding assessment report 2023_ENEA, Eurofusion Report 2R7NAT v1.0', 2024.

[44] A. R. Raffray *et al.*, 'Critical heat flux analysis and R&D for the design of the ITER divertor', *Fusion Engineering and Design*, vol. 45, no. 4, pp. 377–407, 1999, doi: https://doi.org/10.1016/S0920-3796(99)00053-8.

[45] P. Linstrom and W. Mallard, 'The NIST Chemistry WebBook: A Chemical Data Resource on the Internet', no. 46, Mar. 2001.

[46] L. S. Tong, 'A phenomenological study of critical heat flux ASME paper 75-HT-68'. June, 1975.

[47] D. C. Groeneveld *et al.*, 'The 2006 CHF look-up table', *Nuclear Engineering and Design*, vol. 237, no. 15, pp. 1909–1922, 2007, doi: https://doi.org/10.1016/j.nucengdes.2007.02.014.

[48] J.-H. You and H. Bolt, 'Analytical method for thermal stress analysis of plasma facing materials', *Journal of Nuclear Materials*, vol. 299, pp. 9–19, 2001, [Online]. Available: https://api.semanticscholar.org/CorpusID:95584162

[49] RCC-MRx, *Design and Construction Rules for Mechanical Components in high-temperature structures, experimental reactors and fusion reactors*. AFCEN, 2012.

[50] H. S. Carslaw and J. C. Jaeger, *Conduction of Heat in Solids*. Oxford: United Kingdom: Clarendon Press, 1959.

[51] R. J. Atkin and N. Fox, *An Introduction to the Theory of Elasticity*. Mineola, New York: US: Courier Corporation, 2013.

[52] S. P. Timoshenko and J. N. Goodier, *Theory of Elasticity*. University of Michigan: US: McGraw-Hill Education, 1969.

[53] G. R. Liu and S. S. Quek, *The Finite Element Method (Finite Element Method)*. Oxford: United Kingdom: Butterworth-Heinemann, 2014.

[54] E. Gaganidze, 'DEMO Material Properties Handbook', Garching bei München, Germany, 2023.

[55] D. Qu, W. W. Basuki, J. Gibmeier, R. Vaßen, and J. Aktaa, 'Development of Functionally Graded Tungsten/EUROFER Coating System for First Wall Application', *Fusion Science and Technology*, vol. 68, pp. 578–581, 2015, [Online]. Available: https://api.semanticscholar.org/CorpusID:118043308

[56] G. E. C. H. Hsueh, 'Residual Stresses in Meta/Ceramic Bonded Strips', *Journal of the American Ceramic Society* , vol. 68, pp. 241–248, 1985.

[57] E. Gaganidze and others, *DEMO-DEF-1-CD1 - Materials Properties Handbook - Tungsten*. EUROfusion: Munich, Germany, 2020.

[58] L. Shampine and M. Reichelt, 'The matlab ODE suite', *SIAM Journal on Scientific Computing*, vol. 18, Apr. 1997, doi: 10.1137/S1064827594276424.